

Ab initio calculations  
of the optical properties  
of phase-change materials

von  
Manfred Niesert

Diplomarbeit in Physik

vorgelegt der

Fakultät für Mathematik, Informatik und Naturwissenschaften  
der Rheinisch-Westfälischen Technischen Hochschule Aachen

im September 2003

angefertigt im  
Institut für Festkörperforschung (IFF)  
Forschungszentrum Jülich



# Contents

<b>1</b>	<b>Introduction</b>	<b>1</b>
<b>2</b>	<b>Density Functional Theory</b>	<b>5</b>
2.1	The Many-Particle Problem . . . . .	5
2.2	The Hartree-Fock Ansatz . . . . .	6
2.3	Density Functional Theory . . . . .	7
2.4	Exchange and Correlation . . . . .	11
2.5	Spin-Density Functional Theory . . . . .	11
2.6	Determination of the Total Energy . . . . .	12
2.7	Improvements to Density Functional Theory . . . . .	13
<b>3</b>	<b>Dielectric Properties of Solids</b>	<b>15</b>
3.1	Notes on Symmetry . . . . .	15
3.2	Physical Tensors . . . . .	16
3.3	Macroscopic Optics . . . . .	19
3.4	Relation between real and imaginary part . . . . .	21
3.5	Macroscopic Dielectric Function . . . . .	22
3.6	Microscopic Dielectric Function . . . . .	26
<b>4</b>	<b>Basis sets</b>	<b>29</b>
4.1	The Plane-Wave Basis . . . . .	30
4.2	The APW method . . . . .	32
4.3	The LAPW method . . . . .	36
4.4	The Local Orbital extension . . . . .	38
4.5	A note on the kinetic energy in the LAPW basis . . . . .	39
<b>5</b>	<b>Implementation</b>	<b>41</b>
5.1	Momentum matrix elements in the LAPW basis . . . . .	41
5.1.1	Interstitial contribution . . . . .	42
5.1.2	Muffin-tin contributions . . . . .	43
5.1.3	Properties of the matrix elements . . . . .	44
5.1.4	Illustration . . . . .	45
5.2	$k$ -space integration . . . . .	46
5.3	The Real part of the Dielectric Function . . . . .	52

5.4	Backfolding . . . . .	53
5.4.1	Algebraic considerations . . . . .	54
5.4.2	Representation in a basis . . . . .	56
5.4.3	Illustration . . . . .	60
5.4.4	Consequences for computation . . . . .	62
5.5	Resulting problems in the integration . . . . .	63
5.5.1	The Influence of Degeneracy . . . . .	64
5.5.2	The Influence of Band crossing . . . . .	66
5.6	A Note on Computational Demands . . . . .	68
5.7	Test calculation . . . . .	70
5.7.1	Aluminum . . . . .	70
5.7.2	Copper . . . . .	74
<b>6</b>	<b>Application to Phase-Change Materials</b>	<b>77</b>
6.1	Phase-Change Materials . . . . .	77
6.2	GeTe compounds . . . . .	79
6.3	AgTe compounds . . . . .	88
<b>7</b>	<b>Conclusion</b>	<b>93</b>
<b>A</b>	<b>Momentum matrix elements</b>	<b>95</b>
<b>B</b>	<b>Tetrahedron method</b>	<b>101</b>
B.1	Integration weights . . . . .	101
B.2	Number and density of states . . . . .	103
<b>C</b>	<b>Units</b>	<b>105</b>
<b>D</b>	<b>Parameters of calculations</b>	<b>107</b>
	<b>Bibliography</b>	<b>118</b>
	<b>Danksagung</b>	<b>119</b>

# Chapter 1

## Introduction

Data storage plays a major role in information technology. The rapid advances in this area are driven by the need to read and write the information with ever faster speed and ever increasing storage density. These demands are creating new frontiers in solid state physics which fuel the development of new materials, the investigation of new physical phenomena and the development of new methods.

Among competing modern mass storage concepts, rewritable optical storage devices based on *phase-change media* provide one future option to store large amount of data at high data transfer-rates. The understanding, and consequently the development of new, and the improvement of existing rewritable phase change media, which should allow sub-micron bit sizes to be written, read and erased within a few nanoseconds determine the future and the spread of this storage concept. At present such devices are build as exchangeable discs, the rewritable Digital Versatile Disc (DVD). The storage process itself can compete to those of magnetic hard discs in terms of storage/access time.

In devices based on the phase-change effect, information bits correspond to small spots being either in the crystalline or in an amorphous state. These two states of matter exhibit two different reflectivities for incident light, which is optically detected and used to encode the bits 0 and 1. A change between these two states of matter is induced by local heating; either above the melting temperature in the case of writing by transforming the crystalline structure into the amorphous one; or above a lower crystallization temperature, supplying enough energy to recrystallize starting from the amorphous state.

The experimental activities in this field motivated us to investigate the optical properties of phase-change materials based on modern microscopic and materials-dependent theories of solid states physics. The theoretical groundwork for understanding the interaction of incident light with matter on a quantum-mechanical level has already been developed in the late fifties and early sixties of the last century by Ehrenreich and Cohen [EC59] and Adler [Adl62]. The intuitive description involves transitions induced by photons between occupied and unoccupied *single-*

*electron* states. However, the computational tools and capacities to corroborate this framework with calculations for real complex materials has developed more recently.

The density functional theory (DFT), developed by Hohenberg and Kohn [HK64] and Kohn and Sham [KS65], provide a powerful and accurate description of the ground-state electronic properties of the many-electron problem in real materials. The theoretical work discussed in this thesis is based on the local density approximation (LDA) and the generalized gradient approximation (GGA) of the exchange correlation energy. This approach developed to the standard model in solid physics for the description of real materials and has been applied to a large spectrum of complex materials including surfaces and low-dimensional systems. This approach describes the sensitivity of the electronic excitations to their ground-state properties. The time-dependent extension of the density functional theory represents a more refined treatment of the linear and nonlinear response of many-electron systems due to time-dependent external perturbations [ZS80, SZ80, Mah80] than the random-phase approximation described by Ehrenreich and Cohen [EC59]. A key feature of this extension is that it provides a consistent treatment of electron-electron interactions in the absence and the presence of time-varying fields, but it is beyond the scope of this thesis.

At the center of this thesis is the implementation of the microscopic description of the dielectric response function on the basis of the density functional theory in the LDA and GGA. The dielectric function describes the response of matter in an electric field. The implementation is restricted to the long-wavelength limit relevant for light in the optical regime and to linear response theory suitable for low light intensities. Non-linear response, the local field effects, and intraband transitions are neglected. This dielectric response function has been implemented within the context of the full-potential linearized augmented plane-wave (FLAPW) method. This electronic structure method is an all-electron method. It is known to give precise results for materials with transition-metal atoms in open structures and low symmetries as it is experienced in recently explored phase-change materials such as for example the ternary alloys  $\text{AgInTe}_2$  or  $\text{AgSbTe}_2$ . The implementation documented in this thesis includes the momentum-matrix elements, which is a very elaborate task due to the complexity of the LAPW basis-set. It includes also the development of the tetrahedron-method for the Brillouin-zone integration of two-point functions which include simultaneously occupied and unoccupied states. This is necessary for the calculation of the imaginary part of the dielectric response function. The Kramers-Kronig integration has been implemented to obtain the real part of the dielectric function from the imaginary one. Since the FLAPW method FLEUR, used in this thesis, is not capable to treat all Bravais lattices, some structures are calculated in Bravais lattices, which are superstructures to the original lattice. This introduces a backfolding in the electronic structure, which is analyzed with great care in this thesis, not to introduce spurious optical transitions. The implementation is carried out in an algorithm that allows an easy extension to parallel computing over the individual tetrahedra and to program for magneto-optics. The method devel-

oped also works for electronic structure methods with a pure plane-wave basis sets as it is common in pseudo-potential methods. All implementations and numerical approximations have been tested thoroughly for Aluminum and Copper, for which experimental similar theoretical results are available. Similar implementations in all-electron methods have been carried out by Delin [Del98] in a full-potential linear muffin-tin orbital method (FP-LMTO), by Abt [Abt97] in the FLAPW-code WIEN, by Krasovskii in the FLAPW [KS99], by Alouani in an LMTO and projector augmented plane wave (PAW) method [AAW<sup>+</sup>97] and Oppeneer in a augmented spherical wave (ASW) method [SBB<sup>+</sup>00].

In this thesis the dielectric function is determined for phase-change materials calculated within density functional theory. It is structured as follows:

The main aspects of the density functional theory are reviewed in Chapter 2. We define the quantities needed to evaluate the ground-state properties and discuss important details of the computational procedures. Chapter 3 gives the formulation of the dielectric response of matter. For this, general consequences of symmetry, tensor properties, optical constants and spectral functions are recapitulated, followed by a derivation of the dielectric function in the long-wavelength limit. The microscopical and the macroscopical approach are addressed. Chapter 4 introduces basis sets of different plane-wave based electronic structure methods. The LAPW method that forms the basis of the calculations in this thesis is presented in more detail. The implementation of the dielectric function – the momentum-matrix elements, the tetrahedron method and the implementation of the Kramers-Kronig implementation – is layed out in the following chapter 5. A focus is put to the backfolding effect, that occurs for calculations of non-minimal unit cells, and consequences for the computation are explained. Test calculations are performed to compare to reference results. More details on the matrix elements of the momentum operator and on the tetrahedron method are presented in appendices A and B.

A brief description of the class of phase-change materials are given in chapter 6. The implemented method is applied to the GeTe compound in rocksalt and trigonal A7 structure. Although the density of states for both structures are very similar, a significant difference is found for the reflectivity at the ultra-violet energy range, which is also found in the experiment. In appendix C one finds details of used units and in appendix D all computational details are collected. The thesis closes with a conclusion.



# Chapter 2

## Density Functional Theory

### 2.1 The Many-Particle Problem

The complete properties of solids can in principle be calculated *ab initio* – i.e. free of any parameters, only using the setup of the system and its interactions – on a quantum mechanical level. The whole information of a system is contained in the system's wave-function, which has to be obtained as solution of the Schrödinger equation

$$\mathcal{H}|\Psi\rangle = E|\Psi\rangle, \quad (2.1)$$

with  $\mathcal{H}$  the Hamiltonian of a system of interacting nuclei and electrons (assuming  $4\pi\epsilon_0 = 1$ )

$$\mathcal{H} = -\sum_{i=1}^N \frac{\hbar^2}{2m} \nabla_i^2 + \frac{1}{2} \sum_{i \neq j} \frac{e^2}{|\mathbf{r}_i - \mathbf{r}_j|} - \sum_{i,J} \frac{e^2 Z_J}{|\mathbf{r}_i - \boldsymbol{\tau}_J|} + \frac{1}{2} \sum_{I \neq J} \frac{e^2 Z_I Z_J}{|\boldsymbol{\tau}_I - \boldsymbol{\tau}_J|}. \quad (2.2)$$

$\mathbf{r}$  denote the electronical coordinates and  $\boldsymbol{\tau}$  those of the nuclei,  $Z_I$  denotes the charge of the nuclei. Spin-dependence and external fields are omitted. In the relativistic case, the Dirac equation has to be solved. The energy of a state  $\Psi$  is given by

$$E = \langle \Psi | \mathcal{H} | \Psi \rangle. \quad (2.3)$$

The effort to solve this many-body problem scales exponentially with the number of particles described and is unaccomplishable for everything except *very* small systems, and certainly for a macroscopic system with a number of particles of an order of magnitude of  $10^{23}$ .

A first and very general approximation is the Born-Oppenheimer method (also called adiabatic approximation). Since the mass of the electrons is at least three orders of magnitude smaller than those of the nuclei, the electrons are expected to follow the motions of the nuclei instantaneously, while the nuclei will react slowly

to a change in electronic configuration. Therefore, the ion's position can be set fixed, reducing the number of degrees of freedom. (From a strict point of view this approximation needs more precise justification, see [Mad78].) This approximation is used in the majority of electronic calculations.

When calculating the ground state of a system, the energy has to take its minimum. Depending on your ansatz, the solution can usually be obtained by minimizing the total energy.

## 2.2 The Hartree-Fock Ansatz

A variety of different approaches have been developed to tackle this many-particle problem. One frequently used method (in many areas of physics) is to transfer the many-body problem to a *one-particle-like* problem, for instance by imposing some certain form on the wavefunction.

The most basic choice is the *Hartree Ansatz*, which replaces the wavefunction  $\Psi(\mathbf{r}_1, \dots, \mathbf{r}_N)$  with a product of  $N$  one-particle wavefunctions  $\psi(\mathbf{r})$ :

$$\Psi(\mathbf{r}_1, \dots, \mathbf{r}_N) = \psi_1(\mathbf{r}_1) \cdot \psi_2(\mathbf{r}_2) \cdot \dots \cdot \psi_N(\mathbf{r}_N), \quad (2.4)$$

depending only on the spatial coordinate of one particle. If one introduces this ansatz into the Schrödinger equation, one obtains  $N$  Schrödinger-like single-particle equations with a integral called Coulomb term or *Hartree* term, containing the electron-electron interaction. This simple ansatz treats the particles independent in the sense that every particle moves in a static potential created by the other electrons, which is the only interaction considered.

It is possible to take care about the expelling properties of fermions resulting from the Fermi principle – called *exchange* interaction – by using a Slater determinant of wavefunctions instead of a simple product:

$$\Psi(\mathbf{r}_1, \dots, \mathbf{r}_N) = \frac{1}{\sqrt{N!}} \begin{vmatrix} \psi_1(\mathbf{r}_1) & \dots & \psi_N(\mathbf{r}_1) \\ \vdots & \ddots & \vdots \\ \psi_1(\mathbf{r}_N) & \dots & \psi_N(\mathbf{r}_N) \end{vmatrix}. \quad (2.5)$$

This *Hartree-Fock* Ansatz results in a significantly more complex numerical treatment as well as in much better results. Including a wavefunction of this form into the Schrödinger equation gives  $N$  single particle equations now containing an additional term – the *exchange* or *Fock* term – containing contributions from all the other single-particle wavefunctions.

The description is still incomplete due to the fact that the single particles are not independent as assumed in this approximation. These *correlation* effects can not be expressed analytically in the general case.

## 2.3 Density Functional Theory

A new idea how to describe the ground state of a many-particle system has been acquired by Hohenberg and Kohn in the 1960s. It turns the focus from the abstract many-particle state as descriptive quantity of the system to the ostensive charge density in real space. Not only that not the whole information content of the wavefunction is needed, it is not desirable to obtain the complete solution  $\Psi$  for a large system since storage of it is as hardly possible as calculation of it.

One different approach, the Thomas-Fermi theory, was known since the late twenties [Fer27, Tho27]. It assumes the interacting electrons to be independent, moving in an external potential. (In this context the term *external* means everything except of this one particle itself, so it includes also the effects of the nuclei in the system, not only those of fields external to the system.) Then the formulae for the uniform electron gas are applied. The obtained results give only a few quantitative trends, chemicals bonds for instance can not be predicted. However, the system is described by the density only.

**The Lemma of Hohenberg and Kohn:** The charge density relates to the many-particle wavefunction like

$$n(\mathbf{r}) = \left\langle \Psi \left| \sum_{i=1}^N \delta(\mathbf{r} - \mathbf{r}_i) \right| \Psi \right\rangle. \quad (2.6)$$

Hohenberg and Kohn [HK64] derived that for a given *external* potential the expectation value of any observable in the ground state is uniquely defined by and functionals of the charge density. Furthermore, the functional of the total energy

$$E = E[n(\mathbf{r})] \quad (2.7)$$

is minimized by the true ground state density  $n_0(\mathbf{r})$ . This implies that the ground state density can be obtained from the minimization of this functional,

$$\delta E[n] = 0. \quad (2.8)$$

The amount of charge

$$N = \int d^3r n(\mathbf{r}) \quad (2.9)$$

takes the role of a subsidiary parameter. Furthermore the density determines the total potential and therewith the Hamiltonian, that means the complete system and all its derivable properties (including many-body wavefunctions, two-particle Green's functions). A more mathematical insight is that there are functions  $n(\mathbf{r})$  not yielding a valid potential  $v(\mathbf{r})$ , so-called non V-representable functions. These are non-physical densities.

The Hohenberg-Kohn lemma does not imply any knowledge about the physical interactions and is universal thereby. On the other hand, nothing has been stated about the form of the functional  $E[n]$  up to now.

**Kohn-Sham equations:** Kohn and Sham [KS65] formulated a form for the energy functional that proved to be very successful. They proposed to split it up into three contributions

$$E[n] = T_s[n] + U[n] + E_{xc}[n]. \quad (2.10)$$

$T_s$  is the kinetic energy of *non-interacting* particles,  $U$  is the Coulomb energy, and  $E_{xc}$  contains the remaining contributions to the energy due to exchange and correlation. The Coulomb energy of the electrons is constructed out of the electron-electron energy together with the external energy, resulting additively from the Coulomb field of the nuclei and from fields external to the system:

$$U[n] = E_{ext}[n] + E_H[n] \quad (2.11)$$

$$E_{ext}[n] = \int d^3r V_{ext}(\mathbf{r})n(\mathbf{r}) \quad (2.12)$$

$$E_H[n] = 4\pi \frac{e^2}{2} \int d^3r d^3r' \frac{n(\mathbf{r})n(\mathbf{r}')}{|\mathbf{r} - \mathbf{r}'|} \quad (2.13)$$

An advantage of this representation is that for the kinetic energy, which is a significant proportion to the total energy, an analytic expression can be given (see Section 2.6). The density is related to the single particle wavefunctions via

$$n(\mathbf{r}) = 2 \sum_{i=1}^N |\psi_i(\mathbf{r})|^2, \quad (2.14)$$

with the factor 2 accounting the spin degeneracy<sup>1</sup>. For this choice the kinetic energy reads

$$T_s[n] = -2 \sum_{i=1}^N \int d^3r \psi_i^*(\mathbf{r}) \frac{\hbar^2}{2m} \nabla^2 \psi_i(\mathbf{r}). \quad (2.15)$$

Equivalent to minimizing the energy with respect to the density, one can do so as well with respect to the single wavefunctions or to their complex conjugates. The subsidiary condition of particle conservation (2.9) is replaced by the normalization of the wavefunctions

$$\int d^3r |\psi_i(\mathbf{r})|^2 = 1. \quad (2.16)$$

Taking this requirement into account by Lagrange parameters  $\epsilon_i$ , the variation of the energy yields the *Kohn-Sham equations*

$$\mathcal{H}_1 \psi_i(\mathbf{r}) = \left\{ -\frac{\hbar^2}{2m} \nabla^2 + V_{eff}(\mathbf{r}) \right\} \psi_i(\mathbf{r}) = \epsilon_i \psi_i(\mathbf{r}), \quad (2.17)$$

---

<sup>1</sup>In this case, you calculate with half the number of electrons.

which are Schrödinger-like equations of a one-particle Hamiltonian  $\mathcal{H}_1$  containing an effective potential

$$V_{eff}(\mathbf{r}) = V_{ext}(\mathbf{r}) + V_H(\mathbf{r}) + V_{xc}(\mathbf{r}) \quad (2.18)$$

consisting of the external, the Hartree and the exchange-correlation potential

$$V_{ext}(\mathbf{r}) = \frac{\delta}{\delta n(\mathbf{r})} E_{ext}(\mathbf{r}) \quad (2.19)$$

$$V_H(\mathbf{r}) = 4\pi e^2 \int d^3r' \frac{n(\mathbf{r}')}{|\mathbf{r} - \mathbf{r}'|} \quad (2.20)$$

$$V_{xc}(\mathbf{r}) = \frac{\delta}{\delta n(\mathbf{r})} E_{xc}(\mathbf{r}). \quad (2.21)$$

These potentials are simple functions, while the corresponding energies are considered as functionals of the density.

This choice (2.10) of kinetic energy and subsequent derivations converts the problem to a problem of fictitious single particles moving in an effective potential all other particles contribute to.

The parameters  $\epsilon_i$  are introduced as Lagrangian parameters only. As a consequence of Janak's theorem, only the highest occupied value has a physical meaning, i.e. it is equal to the chemical potential, the ionization energy of the system. Beyond this, there is no justification to take these parameters as the one-particle energies. However, it is known from experience that this assumption works surprisingly good, and is thus commonly assumed in band structure calculations.

**Eigenvalue problem:** Usually the Kohn-Sham equations (2.17) are not solved directly, but the solutions are represented in a basis. Then the operator  $\mathcal{H}_1$  has to be constructed and diagonalized. Since the basis functions are not necessarily orthogonal, one has to solve the generalized eigenvalue problem

$$(\mathcal{H}_1 - \epsilon_i \mathcal{S})\mathbf{c} = 0 \quad (2.22)$$

(also called secular equation) with  $\mathcal{S}$  the overlap matrix and  $\mathbf{c}$  the expansion coefficients.

**Self-consistency:** Since the electron density goes into the Hartree potential  $V_H$  and the exchange-correlation potential  $V_{xc}$ , and the effective potential determines the solutions  $\psi_i$  through (2.17), which again make the charge density (2.14), this formalism comprises a self-consistency, as shown in Fig. (2.1).

To enter the loop one has to provide an appropriate starting density. With this the potentials are generated and the one-particle solutions are calculated. In matrix

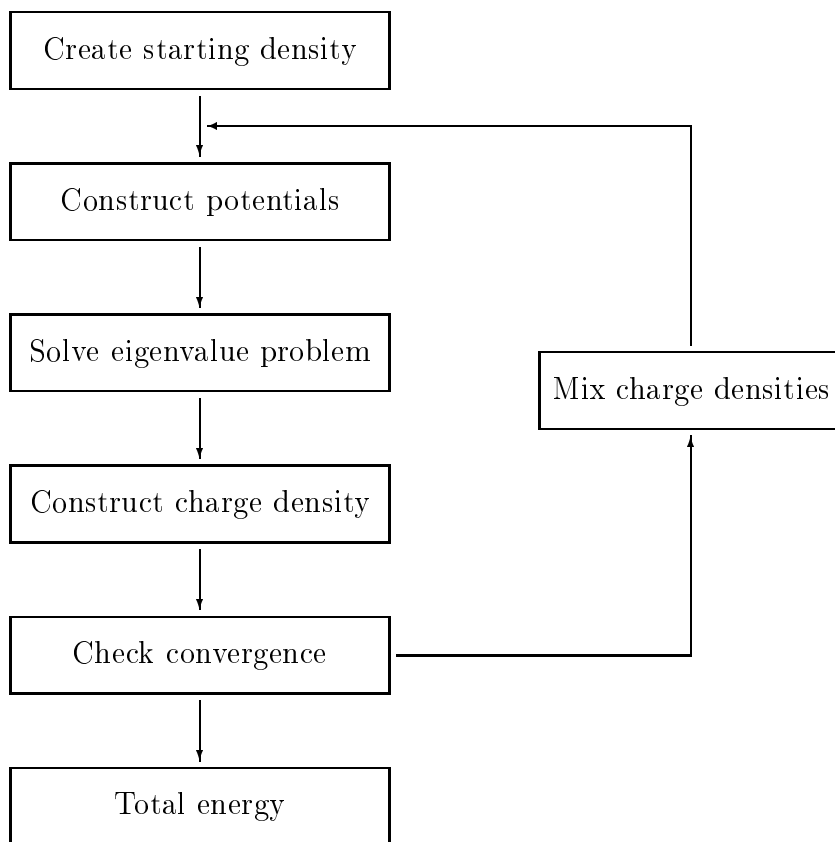


Figure 2.1: The self-consistency cycle of a density-functional calculation.

picture this is the setup of the  $\mathcal{H}$  and  $\mathcal{S}$  matrices and the solution of the generalized eigenvalue problem (2.22). With the results the temporary density  $n_{new}(\mathbf{r})$  is calculated.

One now checks if the difference between the previous density  $n^{(i)}(\mathbf{r})$  and the new one is sufficiently small. If not, the temporary density is incorporated into the previous one. Since taking the calculated density as next input density  $n^{(i+1)}(\mathbf{r})$  for the cycle would introduce too big steps which destroy convergence, some mixing has to be performed. The simplest way is a linear mixing

$$n^{(i+1)}(\mathbf{r}) = (1 - \alpha)n^{(i)}(\mathbf{r}) + \alpha n_{new}(\mathbf{r}) \quad (2.23)$$

with mixing parameter  $\alpha$ . More sophisticated methods like those of Broyden and Anderson have been developed, which incorporate the knowledge of earlier iterations and yield a faster convergence. After finishing the loop, one can process the obtained density, e.g. calculate the total energy.

## 2.4 Exchange and Correlation

Since no approximations have been made so far, density functional theory is exact in principle. However, calculations are only possible with the knowledge of the exchange-correlation energy functional  $E_{xc}[n]$  defined by (2.10). The exact functional is unknown and not soluble analytically. Solving it would be equivalent to solving the many-body problem. Therefore, approximations have to be made.

Basically, the Kohn-Sham equations are a Hartree-like ansatz. All exchange and correlation effects (i.e. all many-body effects) are included in the functional  $E_{xc}[n]$ . It contains the fermionic effects, modifications to the effective potential and corrections to the kinetic energy, all due to the electron-electron interaction. This means that the exchange-correlation potential describes the effects of the Pauli principle and the Coulomb potential beyond a pure electrostatic interaction of the electrons.

The most widely used approach is the *Local Density Approximation* (LDA). The idea is to assume  $E_{xc}$  to be that of a homogenous electron gas with density  $n(\mathbf{r})$ :

$$E_{xc}[n(\mathbf{r})] = \int d^3r n(\mathbf{r})\epsilon_{xc}(n(\mathbf{r})). \quad (2.24)$$

The important simplification is that  $\epsilon_{xc}$  is not a functional of the density, but a function of the value of the density at some spatial coordinate. With this, also the exchange-correlation potential  $V_{xc}$  in (2.19) takes the form of a function. One possible approximation is to view exchange and correlation to be independent:

$$\epsilon_{xc}(n(\mathbf{r})) = \epsilon_x(n(\mathbf{r})) + \epsilon_c(n(\mathbf{r})) \quad (2.25)$$

More complex parametrisations incorporate the results of Hartree-Fock or many-body calculations. One would expect the LDA to fail systems with rapidly varying densities. But it shows to give good results in an unexpected variety of systems.

A class of more sophisticated approximations is the *Generalized Gradient Approximation* (GGA). It makes the same localization ansatz as in (2.24), but connects  $\epsilon_{xc}$  not only with the value of the density but also with the absolute value of its gradient:

$$E_{xc}[n(\mathbf{r})] = \int d^3r n(\mathbf{r})\epsilon_{xc}(n(\mathbf{r}), |\nabla n(\mathbf{r})|). \quad (2.26)$$

## 2.5 Spin-Density Functional Theory

The spin property of electrons, so far only accounted by a degeneracy factor of two, can be easily incorporated into the theory. It has been shown that the basic Hohenberg-Kohn theorem stands for spin-polarized densities as well. You redefine

(in the non-relativistic case) the wavefunctions as spinors

$$\psi_i(\mathbf{r}) = \begin{pmatrix} \psi_{i\uparrow}(\mathbf{r}) \\ \psi_{i\downarrow}(\mathbf{r}) \end{pmatrix}. \quad (2.27)$$

With this slightly different notation, apart from the charge density there arises a second central quantity out of these wavefunctions, the magnetization density  $\mathbf{m}(\mathbf{r})$ :

$$n(\mathbf{r}) = \sum_{i=1}^N \psi_i^*(\mathbf{r})\psi_i(\mathbf{r}) \quad (2.28)$$

$$\mathbf{m}(\mathbf{r}) = \sum_{i=1}^N \psi_i^*(\mathbf{r})\boldsymbol{\sigma}\psi_i(\mathbf{r}). \quad (2.29)$$

$\boldsymbol{\sigma}$  is the vector  $(\sigma_x, \sigma_y, \sigma_z)$  of Pauli matrices. The energy is now a functional of these two densities:

$$E = E[n(\mathbf{r}), \mathbf{m}(\mathbf{r})] \quad (2.30)$$

The two spins couple through an effective magnetic field appearing in the modified Kohn-Sham equations. To incorporate the interaction of an external magnetic field  $\mathbf{B}_{ext}$  with this spin-polarized system, we include the energy contribution  $\mathbf{m}(\mathbf{r}) \cdot \mathbf{B}_{ext}(\mathbf{r})$  into the Kohn-Sham equations and yield

$$\mathcal{H}_1\psi_i(\mathbf{r}) = \left\{ -\frac{\hbar^2}{2m}\nabla^2 + V_{eff}(\mathbf{r}) + \boldsymbol{\sigma}\mathbf{B}_{eff}(\mathbf{r}) \right\} \psi_i(\mathbf{r}) = \epsilon_i\psi_i(\mathbf{r}), \quad (2.31)$$

$$\mathbf{B}_{eff}(\mathbf{r}) = \mathbf{B}_{xc}(\mathbf{r}) + \mathbf{B}_{ext}(\mathbf{r}), \quad (2.32)$$

$$\mathbf{B}_{xc}(\mathbf{r}) = \frac{\delta E[n(\mathbf{r}), \mathbf{m}(\mathbf{r})]}{\delta \mathbf{m}(\mathbf{r})}. \quad (2.33)$$

The approximations in Section 2.4 can be easily extended for the case of spin-polarized systems.

## 2.6 Determination of the Total Energy

When the total energy needs to be calculated, the ion-ion interaction  $E_{ii}$  of the nuclei

$$E_{ii} = e^2 \sum_{I \neq J} \frac{Z_I Z_J}{|\boldsymbol{\tau}_I - \boldsymbol{\tau}_J|} \quad (2.34)$$

has to be included into the functional (2.10),

$$E_{tot}[n] = T_s[n] + E_H[n] + E_{xc}[n] + E_{ext} + E_{ii}. \quad (2.35)$$

Because of numerical reasons, it is not desirable to calculate the kinetic energy in the form (2.15), applying the double spatial derivative. Instead, one utilizes the Kohn-Sham equations (2.17). Rearranging, multiplying the Bra from the left and summing over all occupied states gives

$$-\frac{\hbar}{2m}\nabla^2\psi_i(\mathbf{r}) = (\epsilon_i - V_{eff}(\mathbf{r}))\psi_i(\mathbf{r}) \quad (2.36)$$

$$\Rightarrow T_s[n] = \sum_{i=1}^N \epsilon_i - \int d^3r n(\mathbf{r})V_{eff}(\mathbf{r}). \quad (2.37)$$

$E_H$  and  $E_{ext}$  are have the form (2.13) and (2.12), the exchange-correlation energy is defined by (2.10) and implemented in an approximation like (2.24) or (2.26).

## 2.7 Improvements to Density Functional Theory

Many extensions has been made to the density functional theory and its different approximations. It is a subject of active and continuous development. As we have seen, the treatment of spin and the inclusion of external electric and magnetic fields are a natural extension of the theory. New exchange-correlation functionals such as the generalized gradient approximation (GGA) are being developed.

The GW-approximation is being developed to describe single particle excitation properties based on the many-body perturbation theory in order to recover one of the major drawbacks of the density functional theory in the LDA or GGA, which is the considerable underestimation of the band-gaps in semiconductors. LDA+U theory focuses on the description where the onsite Coulomb interaction is underestimated in the LDA, such as in oxide materials. It is used to improve correlation driven bandgaps. Advanced theories like time-dependent density functional theory (TDDFT) treat electronic excitations due to time-dependent external excitations. It includes single-particle as well as collective excitations and it is based on a fully quantum mechanical formulation of the nonlocal electronic response.

The density functional theory has proven to be a very powerful tool to treat a many-body problem of real material efficiently and precisely in the framework of a one-particle picture. It has been applied also in a variety of other disciplines, like super-conductivity or astrophysics.



# Chapter 3

## Dielectric Properties of Solids

Before going into the details of the dielectric function, general concepts of symmetry and second rank tensors are recapitulated. Important relations of macroscopic optics are given in 3.3, introducing the complex refractive index and the complex dielectric function. The connection between the real and imaginary part is explained in Section 3.4. The connection of optics to a quantum mechanical representation is subsequently given in Section 3.5, and the differences to a microscopic treatment of the electromagnetic wave are addressed in 3.6.

### 3.1 Notes on Symmetry

Symmetry operations transfer a system into itself, leaving it indistinguishable to the initial state. In this context we are interested in symmetry operations in real space. Symmetry operators commute with the Hamiltonian,

$$[(\boldsymbol{\alpha}, \mathcal{T}), \mathcal{H}] = 0. \quad (3.1)$$

$(\boldsymbol{\alpha}, \mathcal{T})$  denotes an operation consisting of a rotation  $\boldsymbol{\alpha}$  and a subsequent translation  $\mathcal{T}$ . Taking symmetries into account can massively simplify the calculations, or makes it only possible.

**Classifications:** Perfect crystals – systems possessing translational symmetry – are classified into lattice types. Considering translations only, this gives the minimal set of essentially different lattice types, the *Bravais lattices*. In three dimensions there are 14 Bravais lattices: the seven lattices cubic, trigonal, rhombic, hexagonal, monoclinic, triclinic and tetragonal, defined by the length of and angles between the basis vectors, and variations of these lattices by occupying unit cell faces or the unit cell center with atoms. The according translational operators of a lattice form the *Translation group*.

The rotations of a system (i.e. the according operators) that map the crystal into itself build the *Rotation group*. There are also *non-symmorphic* symmetries which bring the crystal into itself only with an additional translation (which is not part of the translational group). The according symmetry operations are screw axes and glide planes. These rotations extend the rotation group to the *Point group*. For symmorphic lattices both groups are identical. There are thirty-two different point groups.

The *Space group* contains of the totality of transformations that bring the crystal into itself, containing the translational and the point group as subgroups. There are 230 possible space groups; 157 of them are non-symmorphic, 73 are simple.

**Translational symmetry:** The translational operator

$$\mathcal{T}_{\mathbf{R}} : \mathbf{r} \rightarrow \mathbf{r} + \mathbf{R} \quad (3.2)$$

of a lattice vector  $\mathbf{R}$  commutes with the Hamiltonian so that both operators share a set of eigenvectors. The consequence is the so-called *Bloch theorem*, that states that the eigenfunctions can take the form

$$\psi_n(\mathbf{k}, \mathbf{r}) = e^{i\mathbf{k}\mathbf{r}} \varphi_n(\mathbf{k}, \mathbf{r}), \quad \text{with} \quad \varphi_n(\mathbf{k}, \mathbf{r}) = \varphi_n(\mathbf{k}, \mathbf{r} + \mathbf{R}) \quad (3.3)$$

defining  $\mathbf{k}$  (often called the *crystal momentum*) as a new good quantum number.  $\varphi_n(\mathbf{k}, \mathbf{r})$  is a lattice periodic function. This vector  $\mathbf{k}$  is taken from the reciprocal space. The energy spectrum is periodic in reciprocal space,

$$E(\mathbf{k}) = E(\mathbf{k} + \mathbf{G}) \quad (3.4)$$

with  $\mathbf{G}$  being a reciprocal lattice vector. Thus one can reduce considerations to the first Brillouin zone.

**Rotational symmetry:** To a rotation in real space, the according symmetry operation in the reciprocal space is the inverse rotation. Analogously to the translations, this reduces the effective reciprocal space to consider, leaving as unique part the irreducible wedge of the first Brillouin zone (IBZ).

## 3.2 Physical Tensors

Let us connect two physical vector quantities linearly via

$$\mathbf{B} = \underline{T}\mathbf{a}. \quad (3.5)$$

If  $\mathbf{B}$  is simply proportional to  $\mathbf{a}$  (i.e. pointing in the same direction)  $\underline{T}$  is a scalar factor, but in the general case,  $\underline{T}$  is a tensor of second rank. By its definition, a tensor transforms under a basis change  $\mathcal{A}$  to

$$\underline{T}' = \mathcal{A}\underline{T}\mathcal{A}^T, \quad \text{or} \quad \underline{T}'_{ij} = \mathcal{A}_{ik}\mathcal{A}_{jl}\underline{T}_{kl}. \quad (3.6)$$

Any second-rank tensor can be split up into a symmetric and an antisymmetric part,

$$\underline{T}_{ij}^s = \underline{T}_{ij} + \underline{T}_{ji}, \quad \underline{T}_{ij}^a = \underline{T}_{ij} - \underline{T}_{ji}, \quad \underline{T}_{ij} = \frac{1}{2}(\underline{T}_{ij}^s + \underline{T}_{ij}^a) \quad (3.7)$$

but most physical second-rank tensors are purely symmetrical (i.e.  $T_{ij} = T_{ji}$ ), for example the dielectric tensor being subject of this thesis. (One of the few exceptions is the thermoelectric tensor.) Nye [Nye57] remarks that this symmetry property of tensors is not an obvious one, and that the proof necessarily involves thermodynamical considerations.

The behavior of a symmetric second-rank tensor  $T_{ij}$  under coordinate transformation of the coordinates  $x_i$  follows the equation

$$T_{ij}x_ix_j = 1, \quad (3.8)$$

which defines a sphere that is either an ellipsoid, a hyperboloid of one or a hyperboloid of two sheets. This equation is called the *representation quadric* for the tensor  $T_{ij}$ . An important property of a quadric is that it possesses *principal axes*. These are three directions at right angles such that the general quadric (3.8) takes the form

$$T_{11}x_1^2 + T_{22}x_2^2 + T_{33}x_3^2 = 1, \quad (3.9)$$

when referred to these axes.

A symmetrical tensor referring to arbitrary axes has six independent components. When referring to its principal axes it depends on the symmetry of the crystal in consideration how many independent coefficients remain. The *Neumann principle* states that the symmetry elements of any physical property of a crystal must include the symmetry elements of the point group of the crystal. Thus tensors (or the crystals, accordingly) are grouped in the following three so-called *optical classifications*:

**Isotropic (Anaxial) crystals:** These are crystals in which three arbitrary crystallographically equivalent orthogonal axes can be chosen. These three axes are the principal axes of the tensor. All diagonal elements are equal (see table below), and the crystal acts like an amorphous medium, meaning equal in all directions.

**Uniaxial tensors:** These crystals do not possess three orthogonal equivalent axes, but two or more of these axes in one plane. This is the case for lattices of the tricline, trigonal and hexagonal kind. The plane with the equivalent axes is perpendicular to the three-fold, four-fold or six-fold symmetry axis, respectively. One of the optical axes coincides with this symmetry axes, the others form a pair of orthogonal axes in the plane.

Classification	Crystal System <sup>1</sup>	Indep. Coeff.	Tensor shape
Anaxial	Cubic	1	$\begin{pmatrix} T & 0 & 0 \\ 0 & T & 0 \\ 0 & 0 & T \end{pmatrix}$
Uniaxial	Tetragonal	2	$\begin{pmatrix} T_1 & 0 & 0 \\ 0 & T_1 & 0 \\ 0 & 0 & T_3 \end{pmatrix}$
	Hexagonal		
	Trigonal		
Biaxial	Orthorhombic	3	$\begin{pmatrix} T_1 & 0 & 0 \\ 0 & T_2 & 0 \\ 0 & 0 & T_3 \end{pmatrix}$
	Monoclinic	4	$\begin{pmatrix} T_{11} & 0 & T_{31} \\ 0 & T_2 & 0 \\ T_{31} & 0 & T_{33} \end{pmatrix}$
	Triclinic	6	$\begin{pmatrix} T_{11} & T_{12} & T_{31} \\ T_{12} & T_{22} & T_{23} \\ T_{31} & T_{23} & T_{33} \end{pmatrix}$

Table 3.2: Shapes of second-rank tensors for different crystal structures, taken from a table of ([Nye57]).

**Biaxial tensors:** Crystals with lower symmetry. For orthorhombic crystals, the tensor possesses diagonal form with each different elements. The optical axes coincide with the crystal axes. In monocline and tricline systems, the optical axes are not aligned. (In this case, it would be possible to rotate the axes of the tensor such that only the three principal coefficients are necessary, but one would have no information regarding the orientation of the representation's sphere relative to the crystallographic axes, please confer [Lov89].)

In most cases of calculations the used basis vectors coincide with the optical axes of the crystal in study.

### 3.3 Macroscopic Optics

**Maxwell equations:** This set of equation describes electromagnetic waves. In the presence of matter they read

$$\nabla \times \mathbf{E}(\mathbf{r}, t) = -\frac{\partial}{\partial t} \mathbf{B}(\mathbf{r}, t) \quad (3.10)$$

$$\nabla \cdot \mathbf{D}(\mathbf{r}, t) = \rho(\mathbf{r}, t) \quad (3.11)$$

$$\nabla \times \mathbf{H}(\mathbf{r}, t) = \mathbf{j}(\mathbf{r}, t) + \frac{\partial}{\partial t} \mathbf{D}(\mathbf{r}, t) \quad (3.12)$$

$$\nabla \cdot \mathbf{B}(\mathbf{r}, t) = 0, \quad (3.13)$$

with  $\mathbf{E}$ ,  $\mathbf{D}$  the electric field and the electric displacement,  $\mathbf{B}$  the magnetic induction and  $\mathbf{H}$  the magnetic field.  $\rho$  and  $\mathbf{j}$  describe the external charges and currents. The induced charge and current vanish by the averaging done for this macroscopic approach. This description is complete only if the coupling between the  $\mathbf{D}$  and  $\mathbf{E}$  and between  $\mathbf{B}$  and  $\mathbf{H}$  is given.

**Material coefficients:** To describe the response linearly, one introduces two coupling functions (also called *constants* frequently), the dielectric function  $\varepsilon$  (also known as permittivity) and the magnetic permeability  $\mu$ , by

$$\mathbf{D} = \varepsilon \varepsilon_0 \mathbf{E}, \quad \mathbf{B} = \mu \mu_0 \mathbf{H}. \quad (3.14)$$

Alternatively the electric polarization  $\mathbf{P}$  and the magnetization  $\mathbf{M}$  are defined by

$$\mathbf{D} = \varepsilon_0 \mathbf{E} + \mathbf{P}, \quad \mathbf{P} = \alpha_p \mathbf{E} = \chi \varepsilon_0 \mathbf{E}, \quad (3.15)$$

$$\mathbf{H} = \frac{1}{\mu_0} \mathbf{B} - \mathbf{M}, \quad \mathbf{M} = \chi_m \mathbf{H}, \quad (3.16)$$

defining the electric and magnetic susceptibilities  $\chi$  and  $\chi_m$  and the polarizability  $\alpha_p$  as

$$\varepsilon = 1 + \chi, \quad \alpha_p = \varepsilon_0 \chi, \quad \mu = 1 + \chi_m \quad (3.17)$$

When coupling the current  $\mathbf{j}$  proportional to the electric field according to Ohm's law, the electrical conductivity  $\sigma$  is introduced:

$$\mathbf{j} = \sigma \mathbf{E}. \quad (3.18)$$

The conductivity relates to the dielectric function by

$$\sigma(\omega) = -i\omega \varepsilon_0 \chi(\omega). \quad (3.19)$$

**Absorption of waves:** In vacuum, the electric field of a free electromagnetic wave follows the wave equation

$$\Delta \mathbf{E}(\mathbf{r}, t) = \mu_0 \varepsilon_0 \frac{\partial^2}{\partial t^2} \mathbf{E}(\mathbf{r}, t), \quad (3.20)$$

which has solutions

$$\mathbf{E}(\mathbf{r}, t) = \mathbf{E}_0 e^{i(\mathbf{k}\mathbf{r} - \omega t)}. \quad (3.21)$$

When penetrating matter, the amplitude decays exponentially,

$$E = E_0 e^{-\frac{1}{2}\alpha z}, \quad (3.22)$$

with the absorption coefficient  $\alpha$  defined as

$$\frac{dI}{dz} = -\alpha I \quad (3.23)$$

for penetration in  $z$ -direction, and  $I \sim |E|^2$  the intensity. The complex refractive index

$$\bar{n}(\omega) = n(\omega) + i\kappa(\omega) \quad (3.24)$$

include the real refractive index  $n$  and the extinction coefficient  $\kappa$ . The dielectric function is coupled via the relation

$$\varepsilon(\omega) = \bar{n}^2(\omega) \quad (3.25)$$

with the dielectric constant  $\varepsilon(\omega) = \varepsilon_1(\omega) + i\varepsilon_2(\omega)$ . The real and imaginary part are related to  $n$  and  $\kappa$  as

$$n^2 - \kappa^2 = \varepsilon_1 \quad (3.26)$$

$$2n\kappa = \varepsilon_2, \quad (3.27)$$

or vice versa

$$n = \sqrt{\frac{1}{2} \left( \sqrt{\varepsilon_1^2 + \varepsilon_2^2} + \varepsilon_1 \right)} \quad (3.28)$$

$$\kappa = \sqrt{\frac{1}{2} \left( \sqrt{\varepsilon_1^2 + \varepsilon_2^2} - \varepsilon_1 \right)}. \quad (3.29)$$

Taking into account the boundary conditions of the electric and magnetic field at an interface of one dielectric to air, the reflectivity of a bulk surface reads

$$R = \left( \frac{1 - \bar{n}}{1 + \bar{n}} \right)^2 = \frac{(n - 1)^2 + \kappa^2}{(n + 1)^2 + \kappa^2}. \quad (3.30)$$

In the case of thin films, different formulae have to be used to determine the reflectivity, taking into account multiple reflections inside the film and interference of these.

**Tensor properties:** In the general case, the couplings (3.14),(3.18) are not simple scalars, but tensor-like and they are not constants but depend on the frequency  $\omega$  and momentum  $\mathbf{k}$ . Since the coupling is homogeneous in time, and for the macroscopic approach also in space, the arguments of the susceptibilities read

$$\mathbf{P}(\mathbf{r}, t) = \varepsilon_0 \int d^3 r' \int dt' \underline{\chi}(\mathbf{r} - \mathbf{r}', t - t') \mathbf{E}(\mathbf{r}', t') \quad (3.31)$$

$$\mathbf{M}(\mathbf{r}, t) = \int d^3 r' \int dt' \underline{\chi}_m(\mathbf{r} - \mathbf{r}', t - t') \mathbf{H}(\mathbf{r}', t') \quad (3.32)$$

Causality has to be conserved by appropriate integration boundaries, or by defining the susceptibilities zero for this values. In Fourier space this convolution gives

$$\mathbf{P}(\mathbf{k}, \omega) = \underline{\chi}(\mathbf{k}, \omega) \mathbf{E}(\mathbf{k}, \omega) \quad (3.33)$$

$$\mathbf{M}(\mathbf{k}, \omega) = \underline{\chi}_m(\mathbf{k}, \omega) \mathbf{H}(\mathbf{k}, \omega). \quad (3.34)$$

### 3.4 Relation between real and imaginary part

The real and imaginary parts of the refractive index and of the dielectric function are not independent, but closely related to each other. Due to the Dirac relation

$$\frac{1}{\omega + i\epsilon} = \mathcal{P} \frac{1}{\omega} + i\pi\delta(\epsilon) \quad (3.35)$$

a spectral distribution function with an energylike parameter  $\omega$

$$G(\omega) = \lim_{\epsilon \rightarrow 0} \frac{1}{N} \int d^3 k \frac{F(\mathbf{k})}{E - E(\mathbf{k}) - i\epsilon} \quad (3.36)$$

has its real part

$$\Re G(\omega) = \frac{1}{N} \mathcal{P} \int d^3 k \frac{F(\mathbf{k})}{\omega - \omega(\mathbf{k})} \quad (3.37)$$

and its imaginary part

$$\Im G(\omega) = \frac{\pi}{N} \int d^3 k F(\mathbf{k}) \delta(\omega - \omega(\mathbf{k})), \quad (3.38)$$

which are Hilbert transforms of each other.  $\mathcal{P}$  denotes the principle value of an integral, that is the integral with singularities excluded. For instance if within the interval  $[a, b]$  the function  $f$  contains one singularity at  $x_0$ , the principal value reads

$$\mathcal{P} \int_a^b dx f(x) = \lim_{g \rightarrow +0} \int_a^{x_0-g} dx f(x) + \int_{x_0+g}^b dx f(x). \quad (3.39)$$

The principal value might converge even if each of the two integrals on the right side diverge.

**Kramers-Kronig Relation:** These relations connect the real and imaginary part of any spectral function that relates two fields in a linear and causal way. The relations read

$$\epsilon_1(\omega) = 1 + \frac{1}{\pi} \mathcal{P} \int_{-\infty}^{+\infty} d\eta \frac{\epsilon_2(\eta)}{\eta - \omega} \quad (3.40)$$

$$\epsilon_2(\omega) = -\frac{1}{\pi} \mathcal{P} \int_{-\infty}^{+\infty} d\eta \frac{\epsilon_1(\eta) - 1}{\eta - \omega}. \quad (3.41)$$

$\mathcal{P}$  denotes the principal value of the integral. Since  $\omega > 0$  it is desirable to transform (3.40) to integrals over the domain  $(0, \infty)$ . Utilizing the relation

$$\varepsilon(-\omega) = \varepsilon_1(-\omega) + \frac{i\sigma(-\omega)}{-\omega} = \varepsilon^*(\omega), \quad (3.42)$$

and by multiplying both the numerator and denominator of (3.40) with  $(\eta + \omega)$ , one yields

$$\epsilon_1(\omega) = 1 + \frac{2}{\pi} \mathcal{P} \int_0^{\infty} d\eta \frac{\eta \epsilon_2(\eta)}{\eta^2 - \omega^2} \quad (3.43)$$

$$\epsilon_2(\omega) = -\frac{2}{\pi} \mathcal{P} \int_0^{\infty} d\eta \frac{\epsilon_1(\eta) - 1}{\eta^2 - \omega^2}. \quad (3.44)$$

The consequence of the Kramers-Kronig relations is that once the imaginary part is known for the whole spectrum, the real part is known as well, and vice versa. It is also worth to notice that these relations are of universal validity since they do not imply any knowledge of the interactions inside the solid. However, it poses a difficult task in experiments to scan the whole frequency range.

One can also construct Kramers-Kronig relations for other quantities, like the magnitude and the phase of the complex reflection coefficient.

### 3.5 Macroscopic Dielectric Function

Up to now there is no connection between the dielectric function and the quantum mechanical state of the system. The first such formulation has been given in the *self-consistent field* (SCF) method. Starting point is the single-particle Liouville-von Neumann equation

$$i \frac{\partial \rho}{\partial t} = [\mathcal{H}, \rho] \quad (3.45)$$

with  $\mathcal{H}$  the Hamiltonian and  $\rho$  the density operator.  $\mathcal{H}$  is separated into an time-independent part  $\mathcal{H}_0$  and a time-dependent perturbation  $V$ ,

$$\mathcal{H} = \mathcal{H}_0 + V(\mathbf{r}, t). \quad (3.46)$$

The unperturbed system has solutions

$$\mathcal{H}_0|\mathbf{k}\rangle = E(\mathbf{k})|\mathbf{k}\rangle, \quad (3.47)$$

and the density operator of this system acts like

$$\rho_0|\mathbf{k}\rangle = f_0(E(\mathbf{k}))|\mathbf{k}\rangle, \quad (3.48)$$

$f_0$  being the Fermi distribution function for zero temperature. By assuming the density operator of the perturbed system to be of the form  $\rho = \rho_0 + \rho_1$ , one arrives at the linearized form of the Liouville equation (3.45)

$$i\frac{\partial\rho_1}{\partial t} = [\mathcal{H}_0, \rho_1] + [V, \rho_0] \quad (3.49)$$

if the term of higher order  $[V, \rho_1]$  is neglected. Assuming a time dependence  $V \sim e^{-i\omega t} e^{\delta t}$  of an electromagnetic oscillation, one obtains

$$\langle\mathbf{k}|\rho_1|\mathbf{k} + \mathbf{q}\rangle = \frac{f_0(E(\mathbf{k} + \mathbf{q})) - f_0(E(\mathbf{k}))}{E(\mathbf{k} + \mathbf{q}) - E(\mathbf{k}) - \hbar\omega + i\hbar\delta} \langle\mathbf{k}|V|\mathbf{k} + \mathbf{q}\rangle. \quad (3.50)$$

This *self-consistent field* method relates the induced density  $\rho_1$  to the perturbing potential. The form of the perturbing potential makes this a semi-classical model, treating the electrons quantum mechanically and the photon as a classical electromagnetic wave (though it gives away its energy quantized). Lindhard [Lin54] has given an expression for the dielectric function within this self-consistent field method

$$\varepsilon(\mathbf{q}, \omega) = 1 - \frac{4\pi e^2}{q^2\Omega^*} \lim_{\delta \rightarrow 0} \int d^3k \frac{f_0(E(\mathbf{k} + \mathbf{q})) - f_0(E(\mathbf{k}))}{E(\mathbf{k} + \mathbf{q}) - E(\mathbf{k}) - \hbar\omega + i\hbar\delta}. \quad (3.51)$$

The integration runs over the whole system,  $\Omega^*$  is the system's volume. Ehrenreich and Cohen [EC59] showed that this is equivalent to a many-particle approach based on the random-phase approximation (RPA) for a Fermi gas at zero temperature given by Nozière and Pines [NP58b, NP58a]. Ehrenreich applied this to solids of cubic structure and obtains

$$\varepsilon(\mathbf{q}, \omega) = 1 - \frac{4\pi e^2}{q^2\Omega} \lim_{\delta \rightarrow 0} \sum_{i,f} \int d^3k \frac{|\langle f, \mathbf{k} + \mathbf{q} | i\mathbf{k} \rangle|^2}{E_f(\mathbf{k} + \mathbf{q}) - E_i(\mathbf{k}) - \hbar\omega + i\hbar\delta} \times [f_0(E_i(\mathbf{k} + \mathbf{q})) - f_0(E_f(\mathbf{k}))], \quad (3.52)$$

the two summation indices running over all bands. The integration runs over the unit cell with volume  $\Omega$ . The  $\mathbf{q}$  indicate involved phonons, taking up a difference

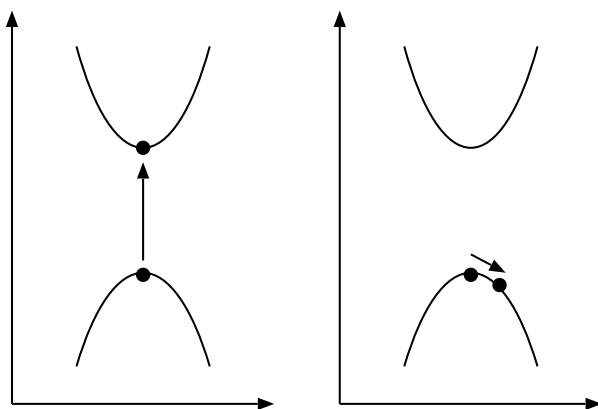


Figure 3.1: Sketch of interband and intraband transitions. In the shown model band structures (i.e. plots of energy  $E$  vs. crystal momentum  $\mathbf{k}$ ) the spots indicate one-particle states. On the left an interband transition from band  $i$  to band  $f$  is drafted, on the right an intraband transition within one band  $i$ .

in crystal momentum. Compared to (3.51) the square of the matrix element in the numerator has appeared. Perturbation theory in the limit  $|\mathbf{q}| \rightarrow 0$  yields

$$|\langle f, \mathbf{k} + \mathbf{q} | i\mathbf{k} \rangle|^2 = \delta_{fi} + (1 - \delta_{fi}) \left( \frac{q}{m\omega_{fi}} \right)^2 |\langle f\mathbf{k} | \frac{\nabla}{i} | i\mathbf{k} \rangle|^2, \quad (3.53)$$

with  $\hbar\omega_{fi} = E_f(\mathbf{k}) - E_i(\mathbf{k})$ . The  $|i\mathbf{k}\rangle$  are Bloch states. In order to consider the long-wavelength limit  $q \rightarrow 0$ , the dielectric function is split up into the interband and the intraband part sketched in Fig. 3.1,

$$\varepsilon(\omega) = \varepsilon^{inter}(\omega) + \varepsilon^{intra}(\omega). \quad (3.54)$$

For reasons of convenience, both parts are split into their real and imaginary parts  $\varepsilon = \varepsilon_1 + i\varepsilon_2$ . The intraband contribution gives [ZL83]

$$\varepsilon_1^{intra}(\omega) = 1 - \frac{\tilde{\omega}_p^2}{\omega^2} \quad (3.55)$$

$$\varepsilon_2^{intra}(\omega) = -i\pi\tilde{\omega}_p^2 \frac{\partial}{\partial\omega} \delta(\omega). \quad (3.56)$$

An intraband transition involves a photon and is therefore a process of higher order. The imaginary part vanishes everywhere except of  $\omega = 0$  and has a singularity at this point. The plasma frequency  $\omega_p$  of a homogeneous electron gas of density  $n$  is defined by

$$\omega_p^2 = \frac{4\pi e^2 n}{m}. \quad (3.57)$$

The effective plasma frequency  $\tilde{\omega}_p$  together with the optical effective mass  $m_{opt}$  is defined by

$$\tilde{\omega}_p^2 \equiv \frac{m}{m_{opt}} \omega_p^2 = \frac{4\pi e^2}{\hbar^2} \sum_i \frac{1}{V_G} \int d^3k f_0(E_i(\mathbf{k})) \nabla_{\mathbf{k}}^2 E_i(\mathbf{k}). \quad (3.58)$$

The interband part takes the form

$$\begin{aligned} \varepsilon_1^{inter}(\omega) &= \frac{e^2}{\pi^2 m^2} \sum_{i,f} \mathcal{P} \int d^3k \frac{\hbar^2}{E_f(\mathbf{k}) - E_i(\mathbf{k})} |\langle f\mathbf{k} | \frac{\nabla}{i} | i\mathbf{k} \rangle|^2 \times \\ &\quad \frac{f_0(E_i(\mathbf{k})) [1 - f_0(E_f(\mathbf{k}))]}{(E_f(\mathbf{k}) - E_i(\mathbf{k}))^2 - (\hbar\omega)^2} \end{aligned} \quad (3.59)$$

$$\begin{aligned} \varepsilon_2^{inter}(\omega) &= \frac{e^2}{2\pi m^2 \omega^2} \sum_{i,f} \int d^3k |\langle f\mathbf{k} | \frac{\nabla}{i} | i\mathbf{k} \rangle|^2 \times \\ &\quad \delta(E_f(\mathbf{k}) - E_i(\mathbf{k}) - \hbar\omega) \cdot f_0(E_i(\mathbf{k})) [1 - f_0(E_f(\mathbf{k}))]. \end{aligned} \quad (3.60)$$

The two summation indices indicate transitions  $i \rightarrow f$  from an occupied to an unoccupied state. For non-cubic structures, the tensor takes the same form, except that the square of the matrix element turns to a tensor product. Converting the volume integral to a surface integral, the imaginary part of the interband contribution to the dielectric tensor reads

$$\begin{aligned} \varepsilon_2^{\alpha\beta}(\omega) &= \frac{e^2}{2\pi m^2 \omega^2} \sum_{i,f} \int dk^2 \frac{\langle i\mathbf{k} | \frac{\nabla_\alpha}{i} | f\mathbf{k} \rangle \langle f\mathbf{k} | \frac{\nabla_\beta}{i} | i\mathbf{k} \rangle}{|\nabla_{\mathbf{k}}(E_f(\mathbf{k}) - E_i(\mathbf{k}))|} \times \\ &\quad f_0(E_i(\mathbf{k})) [1 - f_0(E_f(\mathbf{k}))]. \end{aligned} \quad (3.61)$$

This function has been implemented in this thesis. The integral runs over the constant-energy surface  $\hbar\omega = E_f(\mathbf{k}) - E_i(\mathbf{k})$ . A term often referred to in this context is the joint density-of-states (JDOS)

$$J(E) = \sum_{i,f} \int \frac{dk^2}{|\nabla_{\mathbf{k}}(E_f(\mathbf{k}) - E_i(\mathbf{k}))|} \quad (3.62)$$

over the plane of constant energy  $E = E_f(\mathbf{k}) - E_i(\mathbf{k})$ . For propagation  $\mathbf{q}$  along unit vector  $\mathbf{u}_q$  the dielectric function is

$$\varepsilon_2(\omega) = \sum_{\alpha\beta} u_{q,\alpha} u_{q,\beta} \cdot \varepsilon_2^{\alpha\beta}. \quad (3.63)$$

The longitudinal and transversal projectors are defined by

$$\mathbf{L} = \mathbf{u}_q \circ \mathbf{u}_q, \quad \mathbf{T} = \mathbb{1} - \mathbf{u}_q \circ \mathbf{u}_q, \quad \mathbf{L} + \mathbf{T} = \mathbb{1}. \quad (3.64)$$

The dielectric tensor can thus be partitioned into

$$\underline{\varepsilon} = (\mathbf{L} + \mathbf{T})\underline{\varepsilon}(\mathbf{L} + \mathbf{T}) \quad (3.65)$$

$$= \mathbf{L}\underline{\varepsilon}\mathbf{L} + \mathbf{L}\underline{\varepsilon}\mathbf{T} + \mathbf{T}\underline{\varepsilon}\mathbf{L} + \mathbf{T}\underline{\varepsilon}\mathbf{T} \quad (3.66)$$

$$= \underline{\varepsilon}_{ll} + \underline{\varepsilon}_{lt} + \underline{\varepsilon}_{tl} + \underline{\varepsilon}_{tt}. \quad (3.67)$$

In a homogenous medium like the free-electron gas, longitudinal (transverse) electromagnetic fields would only cause a longitudinal (transverse) response. In inhomogeneous media such as periodic crystals a purely longitudinal or transverse field induces both kinds of responses. Above, only the longitudinal response has been calculated. It has been shown by Ambegaokar and Kohn [AK60] for cubic crystals and by Del Sole and Fiorino [SF84] for crystals of lower symmetry that in the limit of vanishing  $\mathbf{q}$  the effect of a transverse perturbation (electro-magnetic fields) can be described by a longitudinal response.

### 3.6 Microscopic Dielectric Function

The derivation above started from a macroscopic point of view, i.e. the macroscopic Maxwell equations. However, a precise description on the microscopic scale is only given by the microscopic Maxwell equations

$$\nabla \cdot \mathbf{e} = \frac{\rho_{mic}}{\varepsilon_0} \quad (3.68)$$

$$\nabla \times \mathbf{b} = \mu_0 \mathbf{j}_{mic} + \mu_0 \varepsilon_0 \frac{\partial \mathbf{e}}{\partial t} \quad (3.69)$$

$$\nabla \cdot \mathbf{b} = 0 \quad (3.70)$$

$$\nabla \times \mathbf{e} = -\frac{\partial \mathbf{b}}{\partial t} \quad (3.71)$$

with  $\mathbf{e} = \mathbf{e}(\mathbf{r}, t)$  the microscopic electric field and  $\mathbf{b} = \mathbf{b}(\mathbf{r}, t)$  the microscopic magnetic induction. The macroscopic quantities result from the microscopic ones by averaging over one unit cell

$$\rho = \langle \rho_{mic} \rangle, \quad \mathbf{j} = \langle \mathbf{j}_{mic} \rangle, \quad \mathbf{E} = \langle \mathbf{e} \rangle, \quad \mathbf{B} = \langle \mathbf{b} \rangle. \quad (3.72)$$

The inverse of the macroscopic and microscopic dielectric function (or tensor, respectively) are both related to the electric displacement  $\mathbf{D}$  by

$$\mathbf{E}(\mathbf{r}, t) = \varepsilon_0^{-1} \int d^3 r' \int dt' \underline{\varepsilon}_{mac}^{-1}(\mathbf{r} - \mathbf{r}', t - t') \mathbf{D}(\mathbf{r}', t') \quad (3.73)$$

$$\mathbf{e}(\mathbf{r}, t) = \varepsilon_0^{-1} \int d^3 r' \int dt' \underline{\varepsilon}_{mic}^{-1}(\mathbf{r}, \mathbf{r}', t - t') \mathbf{D}(\mathbf{r}', t'). \quad (3.74)$$

As in (3.31) causality must be conserved. Both dielectric functions are homogeneous in time, but only from the macroscopic point of view the medium is homogeneous; thus the relation for the microscopic dielectric function is more complex. The Fourier transforms

$$\mathbf{E}(\mathbf{k}, \omega) = \varepsilon_0^{-1} \underline{\varepsilon}_{mac}^{-1}(\mathbf{k}, \omega) \mathbf{D}(\mathbf{k}, \omega) \quad (3.75)$$

$$\mathbf{e}(\mathbf{k} + \mathbf{G}, \omega) = \varepsilon_0^{-1} \sum_{\mathbf{G}'} \underline{\varepsilon}_{mic}^{-1}(\mathbf{k} + \mathbf{G}, \mathbf{k} + \mathbf{G}', \omega) \mathbf{D}(\mathbf{k} + \mathbf{G}', \omega) \quad (3.76)$$

reflect this. In (3.76) reciprocal space arguments have been parted into a reciprocal lattice vector  $\mathbf{G}$  (or  $\mathbf{G}'$ , respectively) and a vector  $\mathbf{k}$  within the Brillouin zone.

Due to the coupling of the *inverse* of the dielectric function to the electric displacement in (3.74), this is the quantity that can initially be derived. Out of this the dielectric function itself is determined.  $\underline{\varepsilon}_{mic}^{-1}$  is not only the inverse with respect to the tensor character, but it relates to the dielectric function by

$$\underline{\varepsilon}_{mic}^{-1}(\mathbf{r}, \mathbf{r}', t - t') \underline{\varepsilon}_{mic}(\mathbf{r}', \mathbf{r}'', t' - t'') = \delta(\mathbf{r} - \mathbf{r}') \delta(\mathbf{r}' - \mathbf{r}'') \delta(t - t') \delta(t' - t'') \mathbb{1}. \quad (3.77)$$

Adler [Adl62] and Wiser [Wis63] derived the explicit connection of the microscopic and macroscopic quantities. For this it is useful to understand the vectors  $\mathbf{G}, \mathbf{G}'$  from the Fourier transform as matrix indices. This way the microscopic dielectric tensor

$$\underline{\varepsilon}_{mic}(\mathbf{k} + \mathbf{G}, \mathbf{k} + \mathbf{G}', \omega) \rightarrow [\underline{\varepsilon}_{mic}(\mathbf{k}, \omega)]_{\mathbf{G}\mathbf{G}'} \quad (3.78)$$

appears as a matrix with elements which are tensor functions of  $\mathbf{k}$  and  $\omega$ . Eq. (3.76) turns to a vector equation with a matrix-vector multiplication on the right. The inverse of the macroscopic tensor is equal to the inverse of the microscopic tensor for  $\mathbf{G} = \mathbf{G}' = 0$ ,

$$\underline{\varepsilon}_{mac}^{-1}(\mathbf{k}, \omega) = \underline{\varepsilon}_{mic}^{-1}(\mathbf{k}, \mathbf{k}, \omega). \quad (3.79)$$

This can be written like

$$\underline{\varepsilon}_{mac}(\mathbf{k}, \omega) = [\underline{\varepsilon}_{mic}^{-1}(\mathbf{k}, \mathbf{k}, \omega)]^{-1} \quad (3.80)$$

as well, but one has to remember the matrix character of  $\underline{\varepsilon}_{mic}^{-1}$ . Only the neglect of all off-diagonal matrix elements  $\mathbf{G} \neq \mathbf{G}'$  (the so-called *local field* effects) gives the easy relation

$$\underline{\varepsilon}_{mac}(\mathbf{k}, \omega) = \underline{\varepsilon}_{mic}(\mathbf{k}, \omega). \quad (3.81)$$

In practical applications the matrix  $\underline{\varepsilon}_{mic}$  has to be constructed for a set of  $\mathbf{G}$  vectors and the  $(0, 0)$ -element has to be determined.

For the actual derivation [ZL83] all quantities are consequently Fourier transformed. For the longitudinal response, an expression for the microscopic dielectric function and its inverse depending on the induced microscopic charge density can be calculated. For the approximation of independent particles, in the long-wavelength limit the same result as in the macroscopic case (3.60) is found when local fields are neglected.



# Chapter 4

## Basis sets

As already mentioned in Section 2.3, the eigenfunctions are usually expanded in a basis,

$$\langle \mathbf{r} | i \mathbf{k} \rangle = \psi_i(\mathbf{k}, \mathbf{r}) = \frac{1}{\sqrt{\Omega}} \sum_{\mathbf{G}} C_{\mathbf{k}+\mathbf{G}}^i \phi_{\mathbf{k}+\mathbf{G}}(\mathbf{r}), \quad (4.1)$$

where  $\Omega$  is the unit cell volume. The Hamilton and overlap matrices  $\mathcal{H}$  and  $\mathcal{S}$  are constructed for a set of  $k$ -points, and the generalized eigenvalue problem

$$[\mathcal{H}(\mathbf{k}) - \epsilon_i \mathcal{S}(\mathbf{k})] \mathbf{c}_i(\mathbf{k}) = 0 \quad (4.2)$$

is solved, with  $\mathbf{c}_i(\mathbf{k}) = (C_{\mathbf{k}+\mathbf{G}}^i)$  the vector of the  $C$ -coefficients (of eigenvalue  $i$  and vector  $\mathbf{k}$ ) for all  $\mathbf{G}$ 's. Many questions of detail, as well as general properties of the calculation like accuracy and computational effort depend on the choice of the basis set. The better the basis functions match the shape of the actual wavefunctions, the better the convergence is. Some basis sets may have drawbacks that can not always be lifted by a bigger cut-off.

At this point two possibilities to exploit symmetry should be noted. First one does not need to calculate the whole Brillouin zone (BZ), but can reduce the computation to the irreducible part (IBZ) in which points can not mapped onto each other by symmetry operations. Furthermore the presence of inversion symmetry has a special influence on the wavefunction coefficients. Let  $\mathcal{I}$  be the inversion operator

$$\mathcal{I} \mathbf{r} \rightarrow -\mathbf{r}. \quad (4.3)$$

The Hamilton operator is hermitian,  $\mathcal{H}(\mathbf{k}, \mathbf{r}) = \mathcal{H}^*(\mathbf{k}, \mathbf{r})$ . If the system possesses

inversion symmetry (i.e.  $\mathcal{H}(\mathbf{r}) = \mathcal{H}(-\mathbf{r})$ ), the Hamiltonian matrix elements read

$$\begin{aligned}
\mathcal{H}_{\mathbf{G}\mathbf{G}'}(\mathbf{k}) &= \int d^3r \varphi_{\mathbf{G}}^*(\mathbf{r}) \mathcal{H}(\mathbf{k}, \mathbf{r}) \varphi_{\mathbf{G}'}(\mathbf{r}) \\
&= \int d^3r \varphi_{\mathbf{G}}^*(-\mathbf{r}) \mathcal{H}(\mathbf{k}, -\mathbf{r}) \varphi_{\mathbf{G}'}(-\mathbf{r}) \\
&= \int d^3r \varphi_{\mathbf{G}}(\mathbf{r}) \mathcal{H}^*(\mathbf{k}, \mathbf{r}) \varphi_{\mathbf{G}'}^*(\mathbf{r}) \\
&= (\mathcal{H}_{\mathbf{G}\mathbf{G}'}(\mathbf{k}))^*,
\end{aligned} \tag{4.4}$$

if the basis functions obey

$$\mathcal{I}\varphi_{\mathbf{G}}(\mathbf{r}) = \varphi_{\mathbf{G}}^*(\mathbf{r}). \tag{4.5}$$

The same is obviously true for the overlap matrix. This means that in this case the generalized eigenvalue problem deals with real instead of complex matrices, which means a significant ease of calculation. Of course also the expansion coefficients  $C$  are real in this case.

## 4.1 The Plane-Wave Basis

A very simple basis set is build out of plane waves (PWs), the eigenfunctions for a constant potential, that are free electrons

$$\phi_{\mathbf{k}+\mathbf{G}}(\mathbf{r}) = e^{i(\mathbf{k}+\mathbf{G})\mathbf{r}},$$

The use of this basis complies to a simple Fourier transform. Typically this is a good choice for nearly free electrons and delocalized electrons. The simple analytic form usually leads to well-performing calculations that are straight-forward to implement. The Hamilton and overlap matrices can easily be calculated as

$$\begin{aligned}
\mathcal{H}_{\mathbf{G},\mathbf{G}'}(\mathbf{k}) &= \frac{\hbar^2}{2m} |\mathbf{k} + \mathbf{G}|^2 \delta_{\mathbf{G}\mathbf{G}'} + V_{(\mathbf{G}-\mathbf{G}')}, \\
V_{(\mathbf{G}-\mathbf{G}')} &= \int d^3r e^{-i(\mathbf{G}-\mathbf{G}')\mathbf{r}} V_{eff}(\mathbf{r}) \\
\mathcal{S}_{\mathbf{G},\mathbf{G}'} &= \delta_{\mathbf{G}\mathbf{G}'}
\end{aligned} \tag{4.6}$$

The matrix elements of the momentum operator for instance in this basis (in terms of the *eigenfunctions*) give

$$\langle f\mathbf{k} | \frac{\nabla}{i} | i\mathbf{k} \rangle_{PW} = \frac{1}{\Omega} \sum_{\mathbf{G}} (\mathbf{k} + \mathbf{G}) C_{\mathbf{k}+\mathbf{G}}^{f*} C_{\mathbf{k}+\mathbf{G}}^i. \tag{4.7}$$

The choice of  $\mathbf{G}$ -vectors is illustrated in Fig. 4.1. After choosing a cut-off value  $G_{max}$ , all  $(\mathbf{k} + \mathbf{G})$ -vectors are used that obey  $|\mathbf{k} + \mathbf{G}| \leq G_{max}$ . This choice is necessary because of numerical reasons. The number of basis functions obviously depends on the  $k$ -point in consideration.

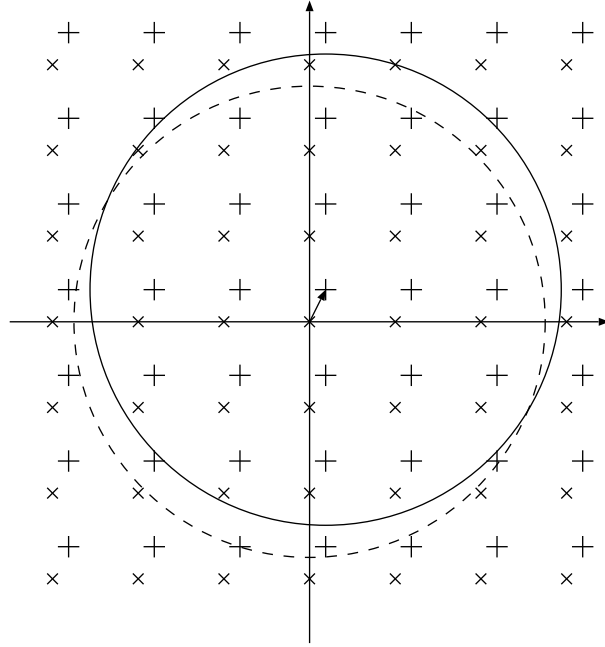


Figure 4.1: Used  $G$ -vectors in expansion. Small x-like crosses indicate the basis vectors of reciprocal space. The plus-like crosses indicate the  $(\mathbf{k} + \mathbf{G})$ -vectors corresponding to the  $\mathbf{k}$ -vector drawn in the origin. The large circle encloses all vectors of  $|\mathbf{G}| < G_{max}$ , the smaller one those of  $|\mathbf{k} + \mathbf{G}| < G_{max}$ .

**Potentials:** The price for this simplicity is the inability of this basis set to describe the strong interactions including the nuclear potential  $\sim \frac{1}{r}$ . As a solution, the idea of *pseudopotentials* has been developed. The potentials are identical to the all-electron potential outside a given core-radius, but of different, smoother shape inside. They are constructed just that the resulting pseudo-wavefunction mimics the all-electron wavefunction outside this radius as close as possible.

For many elements, this method is applicable, i.e such pseudopotentials can be constructed. Usually systems including localized valence electrons, like transition metals, are more problematic.

**Symmetry:** The potential and the charge density are represented in planewaves  $\exp(i\mathbf{G}\mathbf{r})$  which are  $k$ -independent, in contrast to the expansion of the wavefunctions. The needed cut-off should be at least twice as large as for the eigenvectors. The symmetry of the lattice can be used to simplify the representation. The sum of the planewaves of all  $G$ -vectors obtained by the space group operations of the lattice applied on one  $G$ -vectors is called a *star*,

$$\phi_S = \frac{1}{N_{Op}} \sum_{\mathcal{R}} e^{i\mathcal{R}\mathbf{G}(\mathbf{r}-\mathbf{t})}. \quad (4.8)$$

$N_{Op}$  is the number of the space group operations  $\mathcal{R}, t$ . Potentials and charge densities can be expanded in these stars.

Planewaves naturally obey the relation

$$\mathcal{I}e^{i(\mathbf{k}+\mathbf{G})\mathbf{r}} = (e^{i(\mathbf{k}+\mathbf{G})\mathbf{r}})^* , \quad (4.9)$$

which means that (4.4) is valid for this basis, i.e.  $\mathcal{H}$  is real in case of inversion symmetry.

## 4.2 The APW method

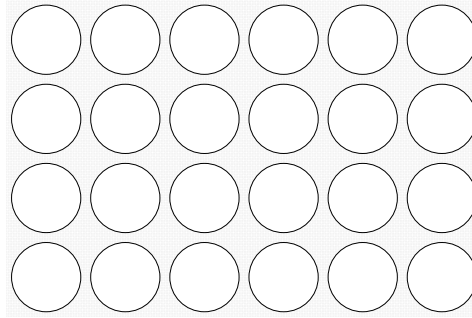


Figure 4.2: Spatial partitioning in augmented basis sets. The circles are the muffin tins, leaving the interstitial region, plotted grayed.

A basis set of better shape has been proposed by Slater already in 1937 [Sla37]. In this *Augmented PlaneWave* (APW) basis, space is divided into spheres that are centered around each atom, so-called muffin-tins (MTs), and into the remaining interstitial region (IS)<sup>1</sup>. While plane waves are used as basis functions in the interstitial, they are augmented in the spheres by spherical harmonics time radial basis functions that are solutions to of the radial Schrödinger equation to an  $l$ -dependent energy

$$\left\{ -\frac{\hbar^2}{2m} \frac{\partial^2}{\partial r^2} + \frac{\hbar^2}{2m} \frac{l(l+1)}{r^2} + V(r) - E_l \right\} r u_l(r) = 0. \quad (4.10)$$

If the according relativistic equation is solved, the solutions are spinors, containing a *large* and a *small* component. Expanding the function in a series of these functions

<sup>1</sup>For non-bulk systems, different choices can be made. For slabs, an additional vacuum region is introduced as a two half-spaces, expanding the function in decaying exponentials [Kur00].

up to an  $l$ -cutoff  $l_{max}$ , this gives the basis functions (the augmented plane waves)

$$\phi_{\mathbf{k}+\mathbf{G}}(\mathbf{r}) = \begin{cases} e^{i(\mathbf{k}+\mathbf{G})\mathbf{r}} & \mathbf{r} \in \text{IS} \\ \sum_{l=0}^{l_{max}} \sum_{m=-l}^l a_{lm}^\alpha(\mathbf{k}+\mathbf{G}) u_l(r, E_l^\alpha) Y_{lm}(\hat{\mathbf{r}}) & \mathbf{r} \in \text{MT}_\alpha. \end{cases} \quad (4.11)$$

The calculation of matrix elements becomes more complicated due to the radial functions being non-orthogonal when restricted to the muffin-tins, and due to the complex shape of the interstitial region.

It is useful to normalize the radial functions like

$$\langle u_l | u_l \rangle = \int_0^{R_\alpha} dr |u_l|^2 = 1 \quad (4.12)$$

To ensure that these basis functions are continuous, one has to match the muffin-tin functions to the planewaves on the boundaries. To arrange this, one expands the spherical harmonics into planewaves using the Rayleigh relation

$$e^{i\mathbf{K}\mathbf{r}} = 4\pi \sum_{lm} i^l j_l(rK) Y_{lm}^*(\hat{\mathbf{K}}) Y_{lm}(\hat{\mathbf{r}}). \quad (4.13)$$

$K = |\mathbf{K}|$  is the length of the vector  $\mathbf{K} = \mathbf{k} + \mathbf{G}$ , and  $j_l$  is the Bessel function of the first kind. Atoms that can be transformed into each other with a symmetry operation form one *atom kind*. For each atom kind, one of its atoms is declared as its representative (see Fig. 4.3). An atom  $\alpha$  at position  $\mathbf{S}_\alpha$  owns a coordinate frame  $(\mathcal{U}_\alpha, \mathbf{S}_\alpha)$  (in the style of symmetry operations 3.1,  $\mathcal{U}_\alpha$  being the rotation matrix). In this frame, a plane-wave takes the form

$$e^{i\mathbf{K}\mathbf{r}} \rightarrow e^{i(\mathcal{U}_\alpha \mathbf{K})(\mathbf{r} + \mathcal{U}_\alpha \mathbf{S}_\alpha)} \quad (4.14)$$

Matching the planewaves on the sphere boundaries with the muffin-tin functions for every augmented wave gives the  $a$ -coefficients as

$$a_{lm}^\alpha(\mathbf{K}) = e^{i\mathbf{K}\mathbf{S}_\alpha} \frac{4\pi i^l}{u_l(R_\alpha, E_l^\alpha)} j_l(K R_\alpha) Y_{lm}^*(\mathcal{U}_\alpha \hat{\mathbf{K}}). \quad (4.15)$$

This leaves the  $C$ -coefficients (and the energies  $E_l^\alpha$ ) as the variational parameters of the method, the  $a$ 's being determined by them. In fact this matching works only on a few points exactly, but the so-chosen  $A$ -coefficients yield the smallest mismatch.

With these basis functions the wavefunction take the form

$$\psi_i(\mathbf{k}, \mathbf{r}) = \begin{cases} \frac{1}{\sqrt{\Omega}} \sum_{\mathbf{G}} C_{\mathbf{k}+\mathbf{G}}^i e^{i(\mathbf{k}+\mathbf{G})\mathbf{r}} & \mathbf{r} \in \text{IS} \\ \sum_{\mathbf{G}} \sum_{lm} C_{\mathbf{k}+\mathbf{G}}^i a_{lm}^\alpha(\mathbf{k}+\mathbf{G}) u_l(r, E_l^\alpha) Y_{lm}(\hat{\mathbf{r}}) & \mathbf{r} \in \text{MT}_\alpha \end{cases} \quad (4.16)$$

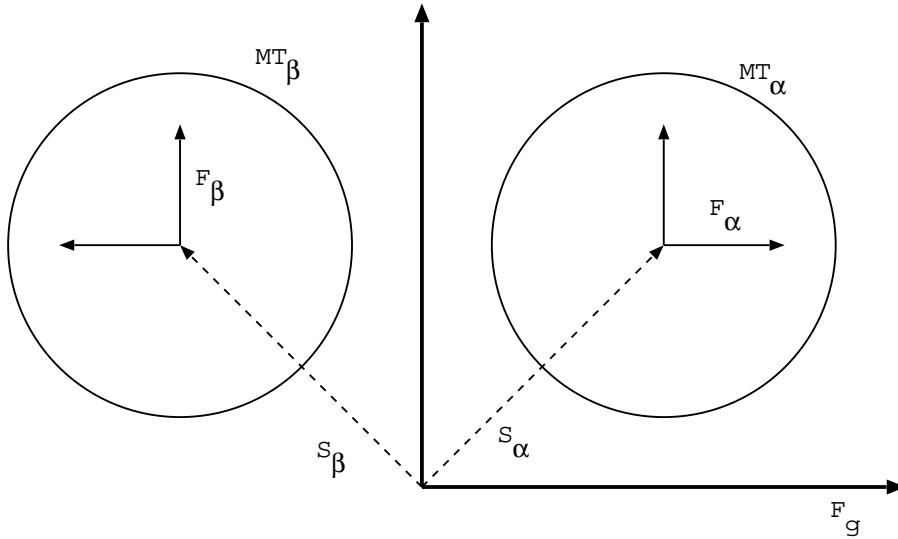


Figure 4.3: Equivalent atoms and its coordinate frames.  $MT_\alpha$ ,  $MT_\beta$  are the spheres centered at  $S_\alpha$ ,  $S_\beta$ . The local frame  $F_\alpha$  of the representative of this atom kind coincides with the global frame  $F_g$ , while the second sphere's frame evolves from the first by a rotation.

Since the  $a$ -coefficients are – together with the expansion coefficients  $C$  – the only terms inside the spheres depending on  $\mathbf{G}$ , one can write the whole wavefunction shorter as

$$\psi_i(\mathbf{k}, \mathbf{r}) = \begin{cases} \frac{1}{\sqrt{\Omega}} C_{\mathbf{k}+\mathbf{G}}^i e^{i(\mathbf{k}+\mathbf{G})\mathbf{r}} & \mathbf{r} \in \text{IS} \\ \sum_{lm} A_{lm}^{i,\alpha}(\mathbf{k}) u_l(r, E_l^\alpha) Y_{lm}(\hat{\mathbf{r}}) & \mathbf{r} \in \text{MT}_\alpha \end{cases} \quad (4.17)$$

with the shorthand

$$A_{lm}^{i,\alpha}(\mathbf{k}) = \sum_{\mathbf{G}} C_{\mathbf{k}+\mathbf{G}}^i a_{lm}^\alpha(\mathbf{k} + \mathbf{G}). \quad (4.18)$$

**Potentials:** Since these basis functions are the solutions of a constant potential in the interstitial and a spherical potential in the muffin tins, this *muffin-tin approximation* for the shape of the potentials has initially been used. In the *warped muffin-tin approximation*, the interstitial potential is extended to general shape, that means extended in planewaves.

Since the actual influence all electrons are taken into account, this method counts to the *all-electron* methods, other than pseudopotential methods. However, it is reasonable to treat the inner shells of the atoms independently since these *core states* do not take part in the chemical bond. Only the outer shells are determined

by solving the crystal eigenvalue problem. Nevertheless, the potentials is made up of all electrons.

**Symmetry:** The representation of charge densities and potentials by stars is over-taken from the planewaves for the interstitial region. In the spheres, due to symmetry operations one can collect spherical harmonics to *lattice harmonics* and expand in this basis [Sin94].

Applying the inversion operator on the APW basis functions considering the construction of the  $A$  coefficients, it turns out that – like the planewaves – also the augmented planewaves obey

$$\mathcal{I}e^{i(\mathbf{k}+\mathbf{G})\mathbf{r}} = (e^{i(\mathbf{k}+\mathbf{G})\mathbf{r}})^*, \quad (4.19)$$

which makes the Hamiltonian  $\mathcal{H}$  real in case of inversion symmetry [Kur00].

The  $A$  coefficients of equivalent atoms are connected, though this can not be seen easily due to the  $(lm)$ -expansion in different local frames. However, for the case of two equivalent atoms  $\alpha, \beta$  mapped onto each other by inversion, the coefficients obey

$$A_{lm}^{i,\alpha} = (A_{lm}^{i,\beta})^* \quad (4.20)$$

for all  $(lm)$  and all states  $i$ .

**Problems of the method:** According to (4.15) the  $A$ 's are determined completely by the planewave coefficients. So these  $C$  coefficients together with the energy parameters  $E_l$  are the variational parameters of this method. If the energy parameters were taken as fixed rather than as a variational parameter, the method would simply consist of the use of the APW basis set with solving the secular equation (4.1). The solutions would give the band energies.

Unfortunately, this is not a workable scheme. The basis functions lack variational freedom, this means they do not yield correct results if the energy parameters  $E_l$  mismatch the actual band energies. This means that these energies for one  $k$ -point can not be obtained from a single diagonalization, but it has to be solved iteratively. This makes this method much more computationally demanding.

Furthermore it is difficult to use a general potential beyond the warped muffin-tin approximation [Sin94]. Another obstacle is the so-called asymptote problem. There might be energy parameters for which  $u_l$  vanishes or becomes very small on the sphere boundary. As a consequence the planewaves and the radial functions become decoupled.

### 4.3 The LAPW method

Much work has been devoted to lift the described problems, e.g. the *modified augmented plane wave* (MAPW) approach by Bross [Bro64, Bro68, BBM<sup>+</sup>70]. In 1975, Andersen introduced the *Linearized Augmented Plane Wave* (LAPW) method. The central idea is to describe the basis functions inside the muffin-tins not only by solutions of the radial Schrödinger equation  $u_l(r, E_l)$ , but as well by its energy derivatives  $\dot{u}_l(r, E_l) \equiv \frac{\partial}{\partial E} u_l(r, E_l)$ . If  $E_l$  differs slightly from the true band energy  $\epsilon$ , according to an expansion with respect to the energy,

$$u_l(r, \epsilon) = u_l(r, E_l) + (\epsilon - E_l)\dot{u}_l(r, E_l) + \mathcal{O}((\epsilon - E_l)^2), \quad (4.21)$$

the true radial function can be approximated sufficiently. The error in the band energies will be of the order  $\mathcal{O}((\epsilon - E_l)^4)$ . The energy derivatives can be acquired from (4.10), taking the energy derivative:

$$\left\{ -\frac{\hbar^2}{2m} \frac{\partial^2}{\partial r^2} + \frac{\hbar^2}{2m} \frac{l(l+1)}{r^2} + V(r) - E_l \right\} r \dot{u}_l(r) = r u_l(r). \quad (4.22)$$

The basis functions are now

$$\phi_{\mathbf{k}+\mathbf{G}}(\mathbf{r}) = \begin{cases} \frac{1}{\sqrt{\Omega}} e^{i(\mathbf{k}+\mathbf{G})\mathbf{r}} & \mathbf{r} \in \text{IS} \\ \sum_{l=0}^{l_{max}} \sum_{m=-l}^l [a_{lm}^\alpha(\mathbf{k}+\mathbf{G}) u_l(r, E_l^\alpha) + b_{lm}^\alpha(\mathbf{k}+\mathbf{G}) \dot{u}_l(r, E_l^\alpha)] Y_{lm}(\hat{\mathbf{r}}) & \mathbf{r} \in \text{MT}_\alpha. \end{cases} \quad (4.23)$$

Analogous to the APW method, the muffin-tin coefficients are determined as

$$a_{lm}^\alpha(\mathbf{K}) = e^{i\mathbf{K}\mathbf{S}_\alpha} \frac{4\pi i^l}{W} Y_{lm}^*(\mathcal{U}_\alpha \hat{\mathbf{K}}) [\dot{u}_l(R_\alpha) K j_l'(K R_\alpha) - \dot{u}_l'(R_\alpha) j_l(K R_\alpha)] \quad (4.24)$$

$$b_{lm}^\alpha(\mathbf{K}) = e^{i\mathbf{K}\mathbf{S}_\alpha} \frac{4\pi i^l}{W} Y_{lm}^*(\mathcal{U}_\alpha \hat{\mathbf{K}}) [u_l(R_\alpha) K j_l'(K R_\alpha) - u_l'(R_\alpha) j_l(K R_\alpha)] \quad (4.25)$$

with the Wronskian

$$W = [\dot{u}_l(R_\alpha) u_l'(R_\alpha) - u_l(R_\alpha) \dot{u}_l'(R_\alpha)]. \quad (4.26)$$

Collecting terms equivalent to the APW basis set, with the definitions

$$\begin{aligned} A_{lm}^{i,\alpha}(\mathbf{k}) &= \sum_{\mathbf{G}} C_{\mathbf{k}+\mathbf{G}}^i \cdot a_{lm}^\alpha(\mathbf{k}+\mathbf{G}), \\ B_{lm}^{i,\alpha}(\mathbf{k}) &= \sum_{\mathbf{G}} C_{\mathbf{k}+\mathbf{G}}^i \cdot b_{lm}^\alpha(\mathbf{k}+\mathbf{G}) \end{aligned} \quad (4.27)$$

the wavefunctions take the form

$$\psi_i(\mathbf{k}, \mathbf{r}) = \begin{cases} \frac{1}{\sqrt{\Omega}} \sum_{\mathbf{G}} C_{\mathbf{k}+\mathbf{G}}^i e^{i(\mathbf{k}+\mathbf{G})\mathbf{r}} & \mathbf{r} \in \text{IS} \\ \sum_{lm} [A_{lm}^{i,\alpha}(\mathbf{k})u_l(r, E_l^\alpha) + B_{lm}^{i,\alpha}(\mathbf{k})\dot{u}_l(r, E_l^\alpha)] Y_{lm}(\hat{\mathbf{r}}) & \mathbf{r} \in \text{MT}_\alpha \end{cases} \quad (4.28)$$

The detailed construction of the  $\mathcal{H}$  and  $\mathcal{S}$  matrices is described in [Kur00]. The formulation above reflects a non-relativistic ansatz. The relativistic approach usually determines the relativistic radial wavefunctions  $u_l(r)$  inside the muffin-tins, which are spinors. In the interstitial, the Hamiltonian is treated non-relativistic. For the matching on the muffin-tin boundaries, only the large component is taken into account, since the small component practically vanishes on the sphere boundaries.

With this additional flexibility, the LAPWs form a good basis for most setups. In contrast to the APW method only one diagonalization is needed to obtain the band energies. And since it is very unlikely that both radial function and its derivative vanish the asymptote problem does not occur.

**Potentials:** In the APW method, a description of the potential beyond the muffin-tin approximation leads to serious problems. For the LAPW method on the other hand, this procedure can be implemented. This full-potential LAPW method (FLAPW or FPLAPW) [Ham79, WKWF81] expands the potential into stars in the interstitial, and into spherical harmonics in the spheres.

**Basis conversion:** A method to link the simplicity of the planewave basis with the accuracy of the more sophisticated LAPW basis set has been proposed by Krasovskii [KSS99]. In this *Augmented Fourier components method* (AFC), the vicinity of the core containing rapid alterations of the wavefunctions is considered to be of low influence on the chemical behavior. The results of calculation in LAPW basis are therefore *gauged* by an appropriate function, generating a smoother wavefunction in this region and leaving a slowly varying valence charge, which can be represented adequately in a planewave basis. From this results, quantities can be calculated in the simple planewave formalism.

**Symmetry:** The LAPW basis obviously includes the same symmetry as the APW basis set. According to (4.20), the coefficients for two atoms connected by inversion symmetry obey

$$A_{lm}^{i,\alpha} = \left( A_{lm}^{i,\beta} \right)^*, \quad B_{lm}^{i,\alpha} = \left( B_{lm}^{i,\beta} \right)^* \quad (4.29)$$

## 4.4 The Local Orbital extension

There might be situations where the variational freedom of the LAPW basis set is not sufficient. One example are semi-core states, which are states of low energy that do not decay completely within the muffin-tins, but have an overlap into the interstitial. Singh [Sin91] introduced the *Local Orbital* extension to the LAPW set to deal with such problems.

The idea is to expand the basis set by additional functions that are zero in the interstitial, to extend flexibility inside the muffin-tins. By constructing these additional basis functions such that the derivative vanishes on the sphere boundaries as well, the  $A$ - and  $B$ - coefficients constructed in (4.24) remain unchanged. The new basis function should have the characteristic of a certain angular momentum  $l_{lo}$  and energy  $E_{lo}$ . This is ensured by a combination of three radial wavefunctions. Hence the additional wavefunction (i.e. one *local orbital*) takes the form

$$\begin{aligned} \phi_{\mathbf{k}+\mathbf{G}_{lo}}(\mathbf{r}) = & \sum_{m=-l_{lo}}^{l_{lo}} [a_{lo,m}^{\alpha}(\mathbf{k} + \mathbf{G}_{lo})u_l^{\alpha}(r, E_l^{\alpha}) + b_{lo,m}^{\alpha}(\mathbf{k} + \mathbf{G}_{lo})\dot{u}_l^{\alpha}(r, E_l^{\alpha}) + \\ & c_{lo,m}^{\alpha}(\mathbf{k} + \mathbf{G}_{lo})u_{l_{lo}}^{\alpha}(r, E_{lo})]Y_{l_{lo},m}(\hat{\mathbf{r}}). \end{aligned} \quad (4.30)$$

inside muffin-tin  $\alpha$ , compare (4.23). The index  $lo = 1, \dots, n_{lo}$  runs over the number of local orbitals introduced, the  $a_{lo}, b_{lo}, c_{lo}$  are the corresponding coefficients for each sphere. The  $l = l_{lo}$  indicates the angular momentum quantum number associated with this local orbital. Each local orbital contains only an  $m$ -sum. This construction contains the essential characteristics in the third part  $(l_{lo}, E_{lo})$ , enriched with the LAPW-like first two parts ensuring the conditions of the boundary (i.e. the function itself and its derivative equal zero).

These two conditions together with the normalization condition do determine the three coefficients of each local orbital. But furthermore they are coupled to fictitious planewave, indicated above by the vectors  $\mathbf{G}_{lo}$ . Though no boundary conditions have to be satisfied, this ensure the local orbital to have Bloch form.<sup>2</sup>. The  $a, b, c$  coefficients above result from this matching.

Collecting the local orbital coefficients similar to (4.27), the wavefunctions inside sphere  $\alpha$  take the form

$$\begin{aligned} \psi_i(\mathbf{k}, \mathbf{r}) = & \sum_{lm} [A_{lm}^{i,\alpha}(\mathbf{k})u_l(r, E_l^{\alpha}) + B_{lm}^{i,\alpha}(\mathbf{k})\dot{u}_l(r, E_l^{\alpha})] Y_{lm}(\hat{\mathbf{r}}) + \\ & \sum_{lo,m} [A_{lo,m}^{i,\alpha}(\mathbf{k})u_l(r, E_l^{\alpha}) + B_{lo,m}^{i,\alpha}(\mathbf{k})\dot{u}_l(r, E_l^{\alpha}) + \\ & C_{lo,m}^{i,\alpha}(\mathbf{k})u_{l_{lo}}(r, E_{lo})]Y_{l_{lo},m}(\hat{\mathbf{r}}). \end{aligned} \quad (4.31)$$

---

<sup>2</sup>For details on this, as well as on the construction of the matrix elements, see [Kur00]

The first line is the unchanged LAPW, while lines two and three are the contributions of the local orbitals, which are summed together in the  $A, B, C$  with index  $(l, m)$ . These coefficients are sets of coefficients different from the standard LAPW  $A, B$  coefficients, as well as from the plane-wave coefficients  $C$ .

## 4.5 A note on the kinetic energy in the LAPW basis

Within the standard APW method one can in principle calculate the exact eigenfunctions by increasing the number of basis functions. For the LAPW basis this is not obvious since one does not perform an iteration to solve the eigenvalue problem. Though the LAPW has been very successful in calculations of the electronic structure and thus is widely used, it turns out that while yielding good energy eigenvalues, the quality of the wavefunctions is deficient.

But this property is of significant importance for the calculation of matrix elements in general and for the momentum matrix elements and optical properties in special. An investigation of this fact has been done by Krasovskii et al. [KNA93].

Different approaches have been developed to improve this fact. Bross et al. for instance enhanced the MAPW method, and developed the *spline augmented planewave* (SAPW) method. This method yields good values for the momentum matrix elements [Feh88]. Within the LAPW framework, this discrepancy of MMEs has in fact been one of the reasons of the development of the local orbitals, and the similar approach of *Extended Linear Augmented Planewaves* (ELAPW) by Krasovskii [Kra97, KS01].



# Chapter 5

## Implementation

The implementation of the dielectric function for this thesis has been done with the FLEUR code [FLE] in bulk mode. FLEUR is a full-potential linear augmented plane-wave (FLAPW) code. In the following sections some details of this implementation shall be discussed.

Since the linearized augmented plane-waves are the basis of choice, the formulae of the momentum matrix elements in this basis are presented in Section 5.1. Details on performing the  $k$ -space integration to obtain the real part of the dielectric function are shown in 5.2. The real part is obtained in 5.3. Due to a restriction of FLEUR, the effect of backfolding has to be discussed in Section 5.4. The problematic influence of this backfolding on the numerical integration is described in Section 5.5. Some remarks in 5.6 are followed by a two test calculations.

When referring in the following to the dielectric function, often it's imaginary part is meant. This should be clear from the context.

### 5.1 Momentum matrix elements in the LAPW basis

The momentum matrix elements (MMEs)<sup>1</sup>

$$\frac{\hbar}{i} \langle f \mathbf{k} | \nabla | i \mathbf{k} \rangle = \frac{\hbar}{i} \int_{uc} d^3r \psi_f^*(\mathbf{k}, \mathbf{r}) \nabla \psi_i(\mathbf{k}, \mathbf{r}) \equiv M_{fi}(\mathbf{k}) \quad (5.1)$$

are to be calculated in the LAPW basis. Due to the partitioning of the unit cell into muffin-tins and the interstitial region by the choice of the augmented basis, the matrix elements have to be calculated in these regions separately:

$$\langle \nabla \rangle = \langle \nabla \rangle_{IS} + \sum_{\alpha} \langle \nabla \rangle_{MT_{\alpha}}. \quad (5.2)$$

---

<sup>1</sup>To avoid confusion with the imaginary unit  $i$ , the initial electronic transition level is labeled  $i$ .

The formulae are presented in atomic units (see appendix C), so the factor  $\hbar = 1$  disappears.

### 5.1.1 Interstitial contribution

In the interstitial, the wavefunctions are<sup>2</sup>

$$|\nu\mathbf{k}\rangle_{IS} = \frac{1}{\Omega} \sum_{\mathbf{G}} C_{\mathbf{k}+\mathbf{G}}^{\nu} e^{i(\mathbf{k}+\mathbf{G})\mathbf{r}}, \quad \mathbf{r} \in IS, \quad (5.3)$$

and the nabla operator acts like

$$\nabla|\nu\mathbf{k}\rangle = \frac{1}{\Omega} \sum_{\mathbf{G}} i(\mathbf{k} + \mathbf{G}) C_{\mathbf{k}+\mathbf{G}}^{\nu} e^{i(\mathbf{k}+\mathbf{G})\mathbf{r}}, \quad \mathbf{r} \in IS, \quad (5.4)$$

so that the interstitial part of the matrix element reads

$$\langle f\mathbf{k} | \frac{\nabla}{i} | \nu\mathbf{k} \rangle_{IS} = \frac{1}{\Omega} \sum_{\mathbf{G}\mathbf{G}'} (\mathbf{k} + \mathbf{G}) C_{\mathbf{k}+\mathbf{G}'}^{f*} C_{\mathbf{k}+\mathbf{G}}^{\nu} \int_{IS} d^3r e^{i(\mathbf{G}-\mathbf{G}')\mathbf{r}}. \quad (5.5)$$

The non-trivial interstitial volume the integral acts on is handled by subtracting the muffin-tins from the whole unit cell  $\Omega$ :

$$\int_{IS} d^3r e^{i(\mathbf{G}-\mathbf{G}')\mathbf{r}} = \int_{\Omega} d^3r e^{i(\mathbf{G}-\mathbf{G}')\mathbf{r}} - \sum_{\alpha} \int_{MT_{\alpha}} d^3r e^{i(\mathbf{G}-\mathbf{G}')\mathbf{r}}. \quad (5.6)$$

While the first integral gives the simple value  $\Omega\delta_{\mathbf{G}\mathbf{G}'}$ , the integral over a muffin-tin centered at  $\mathbf{S}_{\alpha}$  gives the split solution

$$\int_{MT_{\alpha}} d^3r e^{i(\mathbf{G}-\mathbf{G}')\mathbf{r}} = \begin{cases} V & \mathbf{G} = \mathbf{G}' \\ 3V_{\alpha} \frac{\sin x - x \cos x}{x^3} \cdot e^{i(\mathbf{G}-\mathbf{G}')\mathbf{S}_{\alpha}} & \mathbf{G} \neq \mathbf{G}' \end{cases} \quad (5.7)$$

with  $x = |\mathbf{G} - \mathbf{G}'|R_{\alpha}$  and  $R_{\alpha}, V_{\alpha}$  the radius and the volume, respectively, of sphere  $\alpha$ . Altogether this gives (cf. Section 5.6)

$$\langle f\mathbf{k} | \frac{\nabla}{i} | \nu\mathbf{k} \rangle_{IS} = \frac{1}{\Omega} \sum_{\mathbf{G}} (\mathbf{k} + \mathbf{G}) \left[ C_{\mathbf{k}+\mathbf{G}}^{\nu} \left( \Omega - \sum_{\alpha} V_{\alpha} \right) - \sum_{\mathbf{G}' \neq \mathbf{G}} C_{\mathbf{k}+\mathbf{G}'}^{f*} \sum_{\alpha} 3V_{\alpha} \frac{\sin x - x \cos x}{x^3} \cdot e^{i(\mathbf{G}-\mathbf{G}')\mathbf{S}_{\alpha}} \right] \quad (5.8)$$

$$= \sum_{\mathbf{G}\mathbf{G}'} (\mathbf{k} + \mathbf{G}) C_{\mathbf{k}+\mathbf{G}}^{\nu} C_{\mathbf{k}+\mathbf{G}'}^{f*} \cdot s(\mathbf{G} - \mathbf{G}'). \quad (5.9)$$

---

<sup>2</sup>For convenience, the general Ket symbol is used in place of its spatial representation.

In the last line, the expressions of the preceding integral were merged into the function  $s$ , that is

$$s(\mathbf{G} - \mathbf{G}') = \begin{cases} \frac{1}{\Omega}(\Omega - \sum_{\alpha} V_{\alpha}) & \mathbf{G} = \mathbf{G}' \\ -\frac{3}{\Omega} \sum_{\alpha} V_{\alpha} \frac{\sin x - x \cos x}{x^3} e^{i(\mathbf{G} - \mathbf{G}') \cdot \mathbf{S}_{\alpha}} & \mathbf{G} \neq \mathbf{G}' \end{cases} \quad (5.10)$$

with the above  $x = |\mathbf{G} - \mathbf{G}'| R_{\alpha}$ . This is the Fourier representation of the step-function

$$S(\mathbf{r}) = \begin{cases} 1, & \mathbf{r} \in IS \\ 0, & \mathbf{r} \in MT, \end{cases} \quad (5.11)$$

which is constructed already for the setup of the Hamilton and overlap matrices  $\mathcal{H}$  and  $\mathcal{S}$  in the self-consistency part.

### 5.1.2 Muffin-tin contributions

The further procedure depends on what form of wavefunctions you start from. If you use the LAPW functions written explicitly in the basis functions (4.23), without the summation (4.27) in the calculation of your MMEs (5.1), you obtain the summations over  $\mathbf{G}, l, m$  each twice. In the further derivation, not only one pair of the  $(l, m)$ -summation vanishes, but also, by clever conversion, the second  $m$ -summation [Krab]. This leaves summations  $\mathbf{G}, \mathbf{G}', l$ . If you do this, you can simply check the hermiticity of your matrix for every  $\mathbf{G}$ -vector.

In the derivation used in this thesis, LAPWs of the accumulated form (4.28) are used. To derive the matrix elements in the spheres, the momentum operator is expressed in spherical coordinates, and its impact on the spherical harmonics is calculated. Since this part is a bit lengthy, it is moved to appendix A.

In allusion to the ladder operators  $L_+$  and  $L_-$  of the angular momentum operator, one expresses the momentum matrix elements not in terms of  $(\partial x, \partial y, \partial z)^T$ , but in the rotated form

$$\begin{pmatrix} \partial x + i\partial y \\ \partial x - i\partial y \\ \partial z \end{pmatrix} = \mathcal{M} \begin{pmatrix} \partial x \\ \partial y \\ \partial z \end{pmatrix} \equiv \begin{pmatrix} \partial_1 \\ \partial_2 \\ \partial_3 \end{pmatrix}, \quad (5.12)$$

with the base change matrix and its inverse

$$\mathcal{M} = \begin{pmatrix} 1 & i & 0 \\ 1 & -i & 0 \\ 0 & 0 & 1 \end{pmatrix}, \quad \mathcal{M}^{-1} = \begin{pmatrix} \frac{1}{2} & \frac{1}{2} & 0 \\ -\frac{1}{2}i & \frac{1}{2}i & 0 \\ 0 & 0 & 1 \end{pmatrix}. \quad (5.13)$$

The result contains only one  $(l, m)$ -summation and can be expressed as

$$\begin{aligned}
\langle f\mathbf{k}|\partial_n|\iota\mathbf{k}\rangle_{MT_\alpha} &= \sum_{l=0}^{l_{max}-1} \sum_{m=-l}^l & (5.14) \\
& [ ( \int u_{l+1}u'_l r^2 dr - l \int u_{l+1}u_l r dr ) A_{l+1,m'}^{f*} A_{l,m}^i \\
& + ( \int u_{l+1}\dot{u}'_l r^2 dr - l \int u_{l+1}\dot{u}_l r dr ) A_{l+1,m'}^{f*} B_{l,m}^i \\
& + ( \int \dot{u}_{l+1}u'_l r^2 dr - l \int \dot{u}_{l+1}u_l r dr ) B_{l+1,m'}^{f*} A_{l,m}^i \\
& + ( \int \dot{u}_{l+1}\dot{u}'_l r^2 dr - l \int \dot{u}_{l+1}\dot{u}_l r dr ) B_{l+1,m'}^{f*} B_{l,m}^i ] F_{l,m}^{(2n-1)} \\
& + [ ( \int u_l u'_{l+1} r^2 dr + (l+2) \int u_{l+1}u_l r dr ) A_{l,m}^{f*} A_{l+1,m''}^i \\
& + ( \int u_l \dot{u}'_{l+1} r^2 dr + (l+2) \int u_{l+1}\dot{u}_l r dr ) A_{l,m}^{f*} B_{l+1,m''}^i \\
& + ( \int \dot{u}_l u'_{l+1} r^2 dr + (l+2) \int \dot{u}_{l+1}u_l r dr ) B_{l,m}^{f*} A_{l+1,m''}^i \\
& + ( \int \dot{u}_l \dot{u}'_{l+1} r^2 dr + (l+2) \int \dot{u}_{l+1}\dot{u}_l r dr ) B_{l,m}^{f*} B_{l+1,m''}^i ] F_{l+1,m''}^{(2n)}
\end{aligned}$$

for  $n = 1, 2, 3$  indicating the components, and  $m', m''$  given by

$$m' = \begin{pmatrix} m+1 \\ m-1 \\ m \end{pmatrix}, \quad m'' = \begin{pmatrix} m-1 \\ m+1 \\ m \end{pmatrix} \quad \text{for } n = \begin{pmatrix} 1 \\ 2 \\ 3 \end{pmatrix}. \quad (5.15)$$

The factors  $F_{lm}^{(n)}$  are defined in appendix A. In the combinations of coefficients owning angular quantum numbers  $l$  and  $l+1$  in the products, one recognizes the dipole selection rules, i.e. the conservation of angular momentum.

The notation already indicates that only the large component of the wavefunction inside the muffin-tins is taken into account. For the valence states considered this is a good approximation.

### 5.1.3 Properties of the matrix elements

**Hermiticity:** Since the momentum operator is an observable and therewith hermitian, so must be its matrix elements. This can be shown easily by applying partial integration to the defining formula of the matrix elements (5.1). It is also obvious for the MMEs written in the plane-wave basis (4.7).

However it can be hardly seen from the formulae written in LAPW basis, since the interstitial plane-waves are expanded on the muffin-tin boundaries in terms of spherical harmonics utilizing the Rayleigh relation (4.13). If one applies partial integration to the LAPW formulae, one can see that e.g. for the  $(x+iy)$ -component of the muffin-tin contribution to the MME, parts of the factors containing  $F_{l,m}^{(1)}$  compensate with the complex conjugate of the factors containing  $F_{l+1,m-1}^{(2)}$ , leaving the boundary values of the integration un-compensated.

The rest has to be taken by the difference in conjugating the interstitial contribution, which is sensitive to conjugation due to the factor  $(\mathbf{k} + \mathbf{G})$  in the first sum in (5.9).

**Reality:** The diagonal matrix elements are real since the momentum operator is an observable. Furthermore this can also be seen from and compared with the derivatives of the energy bands

$$\langle i\mathbf{k} | \nabla | i\mathbf{k} \rangle = \frac{1}{\hbar} \frac{\partial E_i(\mathbf{k})}{\partial \mathbf{k}}. \quad (5.16)$$

The non-diagonal parts are in general complex, as can be assumed because of the complex  $A, B$  muffin-tin coefficients. For the case of inversion symmetry, however, the matrix elements become real. This is obvious in the case of a plane-wave basis set (4.7) due to the now real  $C$  coefficients, but not for LAPW basis (due to the re-expansion on the muffin-tin boundaries).

**Equivalent atoms:** If one views the muffin-tin part of the MMEs, one sees that apart from the radial functions  $u_l(r)$  and its derivatives the  $A, B$  coefficients are the only contributions specific for the atoms. The former are identical for equivalent atoms, according to Chapter 4. The latter are dependent for equivalent atoms. For the case of inversion symmetry, the coefficients of symmetry equivalent atoms are the complex conjugates of each other. So are the momentum matrix elements,

$$\langle f\mathbf{k} | \nabla | i\mathbf{k} \rangle_{MT_\alpha} = \langle f\mathbf{k} | \nabla | i\mathbf{k} \rangle_{MT_\beta} \quad (5.17)$$

for equivalent atoms  $\alpha, \beta$  due to 4.29 and 5.14.

### 5.1.4 Illustration

To give an impression of the amplitude and  $\mathbf{k}$ -dependence, a band structure-like plot of matrix elements is shown in Fig. 5.1. These are selected MMEs for a simple-cubic Aluminum setup with one atom per unit cell, that is investigated in Section 5.4. The path is  $(0, 0, 0) \rightarrow (\frac{1}{2}, 0, 0) \rightarrow (\frac{1}{2}, \frac{1}{2}, 0) \rightarrow (\frac{1}{2}, \frac{1}{2}, \frac{1}{2}) \rightarrow (0, 0, 0)$ , and due to big variations in amplitude, the plot uses a logarithmic y-axis.

The progression of the curve is monotonous in most areas. On the corners of the path, the matrix elements are not unique due to degeneracy (compare to the band structures in Section 5.4). However, some transitions have a rapid change in amplitude when approaching the corners. In this case, only the sum over the transitions has a physical meaning and gives deterministic results. Another irregularity are jumps that occur within a path, which can usually be connected to band crossings.

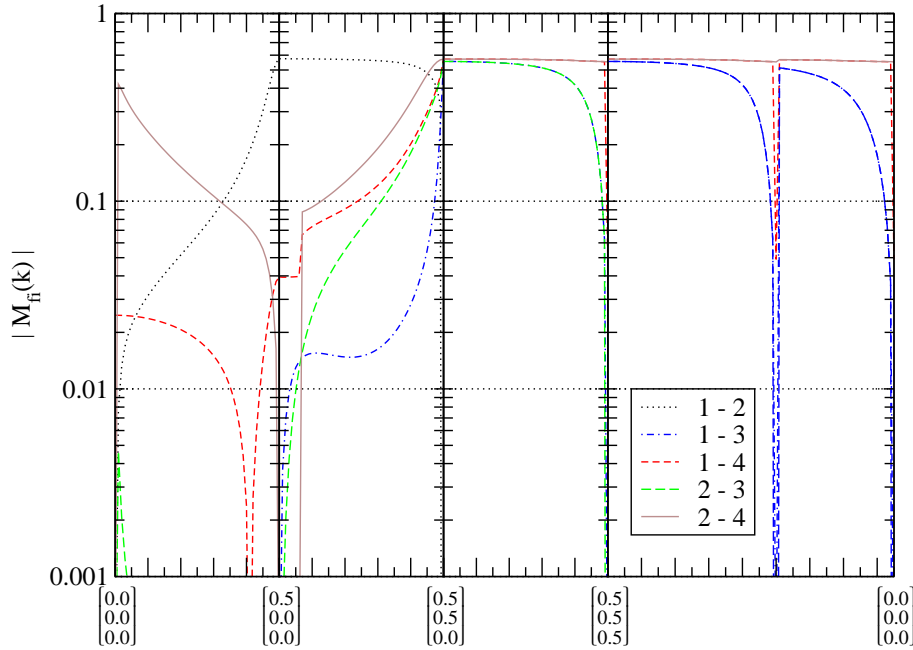


Figure 5.1: The absolute value of matrix elements for five selected transitions evolving on paths on the border of the irreducible Brillouin zone. The initial and final level  $i$  and  $f$  are given in the legend.

## 5.2 $k$ -space integration

The task to perform an integration in  $k$ -space

$$\frac{1}{V_G} \sum_i \int_{BZ} d^3k U(\mathbf{k}) f(\epsilon_i(\mathbf{k})) \quad (5.18)$$

( $V_G$  being the volume of the Brillouin zone,  $f$  the Fermi factor at temperature zero, i.e. a step function) frequently appears in band structure calculations, for instance in the determination of the Fermi energy in the self-consistency of the density functional theory described in Section 2.3. The integrand  $U(\mathbf{k})$  is calculated only for a very finite set of sample  $k$ -points.

There are different kinds of methods, e.g. the special points method [CC73, Cun74]. It provides a set of special  $k$ -points in the irreducible Brillouin zone with alleged weights to calculate the integrand on. This transfers the integration (5.18) into a summation

$$\frac{1}{V_G} \sum_i \int_{BZ} d^3k U(\mathbf{k}) f(\epsilon_i(\mathbf{k})) \rightarrow \sum_i \sum_{\mathbf{k}} U(\mathbf{k}) w_{i\mathbf{k}}. \quad (5.19)$$

For smoothly varying functions this yields reliable results. However, for incomplete occupied bands the integrand in (5.18) is not smooth due to the sharp Fermi factor. Consider for instance a band close to the Fermi energy. In the self-consistency, this band could be shifted above or below the Fermi energy, resulting in big changes in the charge density. This can degrade or even destroy the convergence. One can implement a more elaborate Fermi factor like the true Fermi function

$$f(\epsilon) = \frac{1}{e^{\frac{\epsilon - E_F}{kT}} + 1}, \quad (5.20)$$

that is making the integrand smoothly by a *temperature broadening*.

Another method of integration is to divide the volume into subvolumes of a certain shape and perform the integration in the volume analytically over the interpolated function. Among the method of Gilat and Raubenheimer [GR66, Bro93], the *Tetrahedron Method* is the most prominent integration method of this kind.

**Tetrahedra:** This method was introduced independently by Lehmann and Taut [LT72] in 1972 and by Andersen and Jepsen [JA71] in 1971. It's idea is to divide the integration volume into tetrahedra. This is always possible, though not uniquely. The tetrahedra can in principle have arbitrary shape, but ought to be as regular in shape as possible (e.g. not flattened). The integration thus changes to

$$\frac{1}{V_G} \int_{BZ} d^3k \quad \rightarrow \quad \sum_{\{Tet\}} \frac{V_T}{V_G} \int_{V_T} d^3k. \quad (5.21)$$

$V_T$  is the tetrahedron's volume. In each tetrahedron, the energy interpolated linearly is given uniquely by the four corner energies.

**Interpolation in one tetrahedron:** The corners are labeled from 0 to 3 with increasing energy, i.e.<sup>3</sup>

$$\epsilon_0 < \epsilon_1 < \epsilon_2 < \epsilon_3. \quad (5.22)$$

For the  $k$ -vectors (with the same indices ordered in terms of its corresponding energy) the energy in linear interpolation is

$$\epsilon(\mathbf{k}) = \epsilon_0 + \mathbf{b} \cdot (\mathbf{k} - \mathbf{k}_0). \quad (5.23)$$

---

<sup>3</sup>In this integration scheme one has to avoid equal energies. This does not pose a problem since one can slightly shift the energies without introducing a significant error. In the case of two (or three) identical energies (i.e.  $\Delta\epsilon_{ij} = 0$ , cf. appendix B) the contribution of one tetrahedron (or the corner weights, respectively) is equal to a tetrahedron with one of the critical energies shifted by  $\epsilon$  in the limit  $\epsilon \rightarrow 0$ .

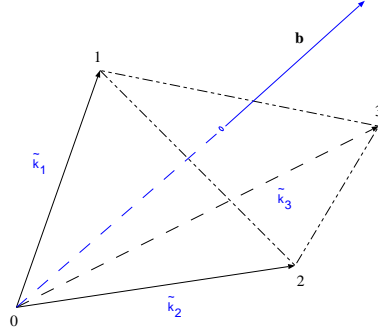


Figure 5.2: A tetrahedron with corner labels sorted by energy, and interpolation vector  $\mathbf{b}$ . The small circle marks the penetration point of the vector.

Here, the vector  $\mathbf{b}$  is defined such that the energy coincides for  $k$  equal  $\mathbf{k}_0, \mathbf{k}_1, \mathbf{k}_2, \mathbf{k}_3$  with the given corner energies. This is provided by the definition

$$\mathbf{b} = \sum_{i=1}^3 (\epsilon_i - \epsilon_0) \mathbf{r}_i, \quad (5.24)$$

including the auxiliary vectors

$$\tilde{\mathbf{k}}_i = \mathbf{k}_i - \mathbf{k}_0, \quad i \in \{1, 2, 3\} \quad (5.25)$$

$$\mathbf{r}_i = \frac{1}{V_T} \tilde{\mathbf{k}}_j \times \tilde{\mathbf{k}}_k, \quad \{i, j, k\} \text{ cyclic.} \quad (5.26)$$

This interpolation yields a continuous energy in the whole integration volume  $BZ$  made out of the set of tetrahedra. The integrand can be interpolated analogously like

$$U(\mathbf{k}) = U_0 + \mathbf{b}' \cdot (\mathbf{k} - \mathbf{k}_0) \quad (5.27)$$

with the according definition

$$\mathbf{b}' = \sum_{i=1}^3 (U_i - U_0) \mathbf{r}_i. \quad (5.28)$$

With this the whole integrand is continuous in the integration volume. A possible simplification is to take the integrand set to a constant value  $\bar{U}$  averaged over the tetrahedron. With this, the quantity is of course not continuous anymore.

Given this linear form of the integrand, the integration in each tetrahedron can be performed analytically.

**Spectral calculations:** This method works fine for spectral integrals, for instance those kinds of integrals mentioned in Section 3.4. Take integrals of the type of the density-of-states

$$\begin{aligned} D(E) &= \frac{1}{V_G} \sum_i \int_{BZ} d^3k \delta(E - E_i(\mathbf{k})) \\ &= \frac{1}{V_G} \sum_i \int_{E=E_i(\mathbf{k})} dS \frac{1}{|\nabla_{\mathbf{k}} E_i(\mathbf{k})|}. \end{aligned} \quad (5.29)$$

If this integrand is interpolated linearly like in (5.27), it gives

$$\frac{1}{|\nabla_{\mathbf{k}} E(\mathbf{k})|} = \frac{1}{|\mathbf{b}|}. \quad (5.30)$$

The constant-energy plane  $E = E_i(\mathbf{k})$  in one tetrahedron is the cross-section of a plane perpendicular to  $\mathbf{b}$ . There are three possible cases of this plane to cut the tetrahedron, yielding a cutting area  $A$  and leading to a contribution of the integral equal  $\frac{A}{|\mathbf{b}|}$ . The explicit results are [LT72]

$$D_T(\epsilon) = \begin{cases} 0 & \epsilon < \epsilon_1 \text{ or } \epsilon_4 < \epsilon \\ \frac{V_T}{V_G} \frac{3(\epsilon - \epsilon_1)^2}{\epsilon_{21}\epsilon_{31}\epsilon_{41}} & \epsilon_1 < \epsilon < \epsilon_2 \\ \frac{V_T}{V_G} \frac{1}{\epsilon_{31}\epsilon_{41}} \left[ 3\epsilon_{21} + 6(\epsilon - \epsilon_2) - 3 \frac{(\epsilon_{31} + \epsilon_{42})(\epsilon - \epsilon_2)^2}{\epsilon_{32}\epsilon_{42}} \right] & \epsilon_2 < \epsilon < \epsilon_3 \\ \frac{V_T}{V_G} \frac{3(\epsilon_4 - \epsilon)^2}{\epsilon_{41}\epsilon_{42}\epsilon_{43}} & \epsilon_3 < \epsilon < \epsilon_4 \end{cases} \quad (5.31)$$

with the energy differences  $\epsilon_{ij} = \epsilon_i - \epsilon_j$ .

**Inclusion of Fermi factors:** The proceeding described will not give good results if the integrand is not continuous but includes Fermi factors, like in (5.18) or (3.61). For corners with energy above Fermi energy the value zero will be used for interpolation irrespective of the occupation of the tetrahedron. But a Fermi factor just defines a constant-energy plane that separates the occupied and unoccupied part. Due to the linear interpolation, such an energy plane is easy to determine, as done for the density of states.

Taking one Fermi factor into account (like in integral (5.18)) means cutting out the remaining *valid* volume, i.e. the volume the Fermi factor is unequal zero in. Depending on the energy  $\epsilon$  and the Fermi energy  $\epsilon_F$  referring to, this volume consists out of zero volume ( $\epsilon_F < \epsilon_1$ ), one subtetrahedron ( $\epsilon_1 < \epsilon_F < \epsilon_2$ ), three subtetrahedra ( $\epsilon_2 < \epsilon_F < \epsilon_3$  or  $\epsilon_3 < \epsilon_F < \epsilon_4$ ), or the complete tetrahedron ( $\epsilon_4 < \epsilon_F$ ) [RF75].

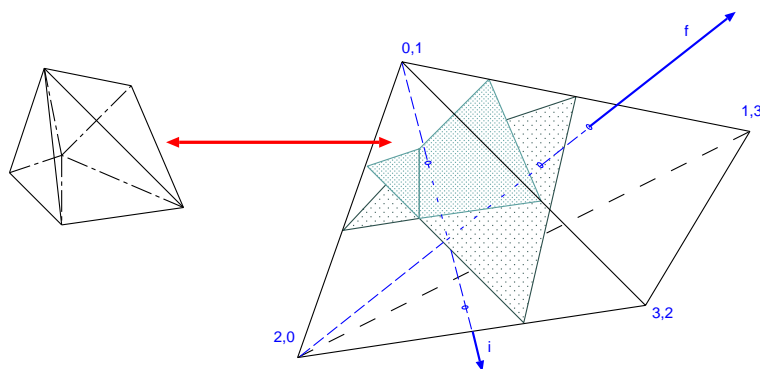


Figure 5.3: A tetrahedron that is divided due to two Fermi factors. The numbers at the corners are the sorted energy indices for the initial and final bands  $i$  and  $f$ , the two vectors are the corresponding  $\mathbf{b}$  vectors (5.24). In this diagram the energy cuts both bands within the tetrahedron and results in two crossing constant-energy planes. Cutting of vectors with these planes or the tetrahedra boundary are marked with small circles. The valid subvolume is marked with the red arrow, as well as shown on the left, with its division into three subtetrahedra.

For an integral containing two Fermi factors like (3.61), one performs on each subtetradron obtained for the first Fermi factor the (inverse) occupation procedure for the second Fermi factor, resulting in at most nine subtetrahedra for the initial tetrahedron. Note that for the second step a renumbering has to be made due to the possibly different order of the energies  $E_f$ .

For the integration (3.61), this means that for every transition  $i \rightarrow f$ , the valid volume is determined, and the remaining integrand, i.e.

$$U(\mathbf{k}) = \frac{\langle i\mathbf{k}|p_\alpha|f\mathbf{k}\rangle\langle f\mathbf{k}|p_\beta|i\mathbf{k}\rangle}{|\nabla_{\mathbf{k}}(E_f(\mathbf{k}) - E_i(\mathbf{k}))|}, \quad (5.32)$$

is evaluated for each of the valid volume's tetrahedra.

**Weighted formulation:** Blöchl has shown that the tetrahedron method can also be written to result in the form of a weighted summation (5.19). These weights are given in appendix B. With this formalism, arbitrary continuous functions can be integrated without doing the geometric derivation (i.e. calculating the cross section of the constant-energy plane with the tetrahedron) mentioned above for the density of states.

It should be noted that the obtained weights do not coincide with those of the special point method which are based on symmetry, i.e. the tetrahedron method does not take into account the high symmetry character of the irreducible zone's boundaries. This leads to a worse convergence than using the special points method,

and is the reason why the tetrahedron method is usually not used for the self-consistency, but for spectral calculations.

Attempts have been made to raise the level of interpolation to a quadratic one. When marking out such a formalism to the linear one introduced above, the latter one is referred to explicitly as *linear tetrahedron* (LT) method.

**Reduction to the Irreducible Brillouin Zone (IBZ):** Usually the eigenvectors and eigenvalues are calculated only in the irreducible part of the Brillouin zone. Let's consider the effect on integral (3.61). Let  $\mathcal{R}$  be an appropriate rotation matrix. The energies are the same at the rotated  $k$ -point

$$E_i(\mathbf{k}) = E_i(\mathcal{R}\mathbf{k}), \quad (5.33)$$

but the eigenvectors are rotated:

$$\langle \mathbf{r} | \iota, \mathcal{R}\mathbf{k} \rangle = \langle \mathcal{R}^{-1}\mathbf{r} | \iota, \mathbf{k} \rangle \quad (5.34)$$

For the calculation of the momentum matrix elements, instead of rotating the eigenvectors one can also rotate the coordinate system and therewith the nabla operator, in symbols  $\nabla_{\mathcal{R}\mathbf{r}} = \mathcal{R}\nabla_{\mathbf{r}}$ . With this the matrix element for a  $k$ -point  $\mathcal{R}\mathbf{r}$  in the first Brillouin zone, but outside the irreducible wedge, can be computed like

$$\begin{aligned} \langle f, \mathcal{R}\mathbf{k} | \nabla | \iota, \mathcal{R}\mathbf{k} \rangle &= \int d^3r \psi_f^*(\mathcal{R}\mathbf{k}, \mathbf{r}) \nabla_{\mathbf{r}} \psi_{\iota}(\mathcal{R}\mathbf{k}, \mathbf{r}) \\ &= \int d^3r \psi_f^*(\mathbf{k}, \mathcal{R}^{-1}\mathbf{r}) \nabla_{\mathbf{r}} \psi_{\iota}(\mathbf{k}, \mathcal{R}^{-1}\mathbf{r}) \\ &= \int d^3r \psi_f^*(\mathbf{k}, \mathbf{r}) \nabla_{\mathcal{R}\mathbf{r}} \psi_{\iota}(\mathbf{k}, \mathbf{r}) \\ &= \mathcal{R} \langle f\mathbf{k} | \nabla | \iota\mathbf{k} \rangle \end{aligned} \quad (5.35)$$

When calculating the integral

$$\varepsilon_2^{\alpha\beta}(\omega) \sim \sum_{\iota f} \int_{\hbar\omega=\Delta E}^{BZ} dS \frac{\langle \iota\mathbf{k} | \nabla_{\alpha} | f\mathbf{k} \rangle^{\dagger} \langle f\mathbf{k} | \nabla_{\beta} | \iota\mathbf{k} \rangle}{|\nabla_{\mathbf{k}}(E_f(\mathbf{k}) - E_{\iota}(\mathbf{k}))|} f(E_{\iota}(\mathbf{k})) [1 - f(E_f(\mathbf{k}))] \quad (5.36)$$

with only use of the irreducible part, one uses the identity of the energies at the corresponding  $k$ -points (5.33). Furthermore  $\mathcal{R}^{\dagger} = \mathcal{R}^{-1}$ , so that the numerator of the fraction in the preceding integral gives

$$\langle \iota, \mathcal{R}\mathbf{k} | \nabla_{\alpha} | f, \mathcal{R}\mathbf{k} \rangle^{\dagger} \langle f, \mathcal{R}\mathbf{k} | \nabla_{\beta} | \iota, \mathcal{R}\mathbf{k} \rangle = \langle \iota\mathbf{k} | \nabla_{\alpha} | f\mathbf{k} \rangle^{\dagger} \langle f\mathbf{k} | \nabla_{\beta} | \iota\mathbf{k} \rangle \quad (5.37)$$

and the integral itself

$$\varepsilon_2^{\alpha\beta}(\omega) \sim N_{\mathcal{R}} \sum_{\iota f} \int_{\hbar\omega=\Delta E}^{IBZ} dS \frac{\langle \iota\mathbf{k} | \nabla_{\alpha} | f\mathbf{k} \rangle^* \langle f\mathbf{k} | \nabla_{\beta} | \iota\mathbf{k} \rangle}{|\nabla_{\mathbf{k}}(E_f(\mathbf{k}) - E_{\iota}(\mathbf{k}))|} f(E_{\iota}(\mathbf{k})) [1 - f(E_f(\mathbf{k}))] \quad (5.38)$$

with  $N_{\mathcal{R}}$  the number of symmetry operations.

**A note on cubic systems:** Since we know from section three that the dielectric tensor is proportional to the unit matrix for cubic crystals, one can immediately reduce the calculation (5.38) to the scalar case, using the square of the absolute value in the numerator.

This is not to be mixed up with the momentum matrix elements itself, which of course still have independent components. For instance remember the diagonal MMEs being proportional to the band derivatives, which have a well-defined direction.

**Reality:** The imaginary part of the dielectric function  $\varepsilon_2(\omega)$  is a real function. So must be the results of (5.38). For the cubic case this is obvious since the denominator reduces to a real expression.

In the case of non-cubic systems (3.61), the integral contains products of momentum matrix elements  $M_{if}^{\alpha*} M_{fi}^{\beta}$  which are in general complex. This means that the components of the tensor obtained from (5.38) can be complex, obeying the relation  $\varepsilon_2^{\alpha\beta} = \varepsilon_2^{\beta\alpha*}$ . But according to (3.63), the resulting dielectric function along a unit vector  $\mathbf{u}$  is composed of a summation

$$\varepsilon_2 = \sum_{\alpha,\beta} \varepsilon_2^{\alpha\beta} u_{\alpha} u_{\beta}, \quad (5.39)$$

containing for every contribution of  $\varepsilon_2^{\alpha\beta}$  the transposed part  $\varepsilon_2^{\beta\alpha}$  as well. Therefore the dielectric function  $\varepsilon_2$  becomes real, and one can reduce the dielectric tensor to its real part  $\tilde{\varepsilon}_2 = \Re \varepsilon_2$  (i.e. symmetrizing it by  $(\tilde{\varepsilon}_2^{\alpha\beta} = \frac{1}{2}(\varepsilon_2^{\alpha\beta} + \varepsilon_2^{\beta\alpha}))$ ). This also restores consistency with the statement in Chapter 3 that the dielectric tensor is symmetrical.

### 5.3 The Real part of the Dielectric Function

Due to the tight relation between real (3.37) and imaginary part (3.38) of spectral functions the real and imaginary part of the interband transitions both take similar form (3.59) and (3.60). The first possibility is to perform  $k$ -space integrations for both the real and imaginary part. This has been done e.g. for the magnetic susceptibility by Gilat and Bharatiya [GB75]. They used the tetrahedron integration scheme to derive analytical expressions for the integral contributions which are quite lengthy. In this thesis, the alternative path is followed, i.e. only the imaginary part is determined, and the Kramers-Kronig integration transformation (3.43) is employed afterwards to obtain the real part.

**Numerical accuracy of the Kramers-Kronig relations:** In this implementation an external integration routine has been used (courtesy of E. Krasovskii). The

accuracy of this method should be tested for a prominent analytical example, this is the harmonic oscillator. The real and imaginary part of the dielectric function are given by

$$\varepsilon_1(\omega) = 1 + \frac{N_0 e^2}{m} \frac{(\omega_0^2 - \omega^2)}{(\omega_0^2 - \omega^2)^2 + \omega^2 \delta^2} \quad (5.40)$$

$$\varepsilon_2(\omega) = \frac{N_0 e^2}{m} \frac{\omega \delta}{(\omega_0^2 - \omega^2)^2 + \omega^2 \delta^2}. \quad (5.41)$$

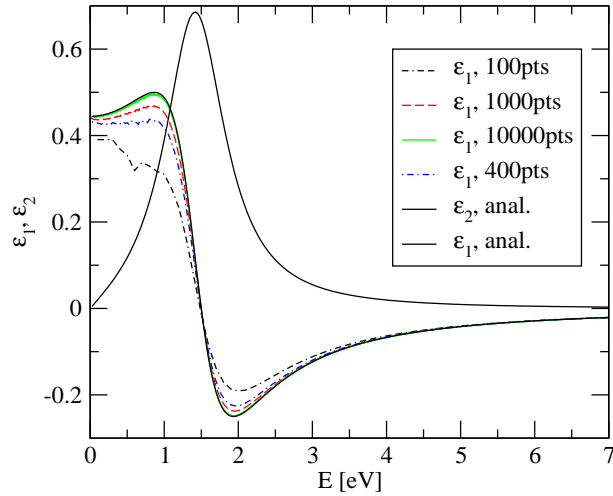


Figure 5.4: Numerical results of the Kramers-Kronig transform for the harmonic oscillator. The analytical solutions are plotted in straight black lines, numerical solutions for four different numbers of mesh points are drawn in dotted colored lines.

Several attenuations and resonance frequencies have been tested. Representative curves are plotted in Fig. 5.4. The used data are  $\delta = 1.0$ ,  $N_0 e^2 / m = 1$ ,  $\omega_{max} = 10 \frac{1}{s}$ ,  $\omega_0 = 1.5 \frac{1}{s}$ . The numerical integration yields good agreement with the analytic curve, supposing that an appropriate set of mesh points (in the order of thousand or more) has been chosen.

## 5.4 Backfolding

At this point it should be mentioned that there are degrees of freedom in the choice of the unit cell. There might be unit cells of different shapes for the same number of atoms, resulting in a different reciprocal lattice. In doing so the band structure stays unchanged in the reciprocal space, but appears different due to the differently chosen basis. There is also the possibility and (possibly the need) to choose a bigger unit cell to model the system, giving a smaller Brillouin zone with modified bands.

The effect on the band structure, called *backfolding*, shall be discussed here. Since the dielectric properties are understood to be transitions between bands, understanding of the impact of backfolding is essential if dealing with bigger unit cells.

### 5.4.1 Algebraic considerations

To understand the effect of periodicity, the Bloch theorem should be recapitulated, to simplify matters in one dimension for a non-degenerate system including time-reversal symmetry. The Schrödinger equation

$$\mathcal{H}\psi_n(r) = E\psi_n(r) \quad (5.42)$$

yields eigenvalues  $E$  and eigenvectors  $\psi$ . When the system consists of unit cells of length  $R$ , the corresponding translation operator is defined as

$$\mathcal{T}_R : r \rightarrow r + R, \quad (5.43)$$

with the properties

$$[\mathcal{T}_R, \mathcal{H}] = 0, \quad (5.44)$$

$$\mathcal{T}_R\psi_n(r) = \psi_n(r + R). \quad (5.45)$$

This translation operator shares a common set of eigenvectors with the Hamiltonian. Since the absolute square of the wavefunctions is independent under proper translations,

$$\mathcal{T}_R|\psi|^2 = \mathcal{T}_R(\psi^*\psi) = (\mathcal{T}_R^*\psi^*)(\mathcal{T}_R\psi) = |\lambda|^2|\psi|^2, \quad (5.46)$$

the eigenvalues of the translational operator take the form  $\lambda = e^{ikr}$ , which at the same time classifies the wavefunctions:  $\psi_n(r) \rightarrow \psi_n(k, r)$ . Furthermore, as a consequence of (5.44) these wavefunctions can be chosen to take *Bloch form*

$$\psi_n(k, r) = e^{ikR}\varphi_n(k, r), \quad \varphi_n(k, r) = \varphi_n(k, r + R), \quad (5.47)$$

consisting of an exponential and a lattice-periodic function. The essential step now is how Bloch waves *shifted in  $k$ -space* react on translations in real space:

$$\mathcal{T}_R\psi_n(k + G, r) = e^{i(k+G)R}\psi_n(k + G, r) = e^{ikR}\psi_n(k + G, r). \quad (5.48)$$

This means that all shifted  $k$ -vectors  $k+G$  are associated to the same eigenvalue  $\lambda = e^{ikR}$  of the translation operator. Therefore the set of eigenvalues and eigenvectors at  $k+G$  are *equivalent* to those at  $k$ . Therefore one can reduce all considerations to the first Brillouin zone  $-\frac{K}{2} \leq k \leq \frac{K}{2}$ ,  $K = \frac{2\pi}{L}$ . One might be confused by this insight since the Hamiltonian in matrix representation in a basis seems to change with a substitution of  $k$  to  $k + G$ . For the case of an infinite basis this substitution only

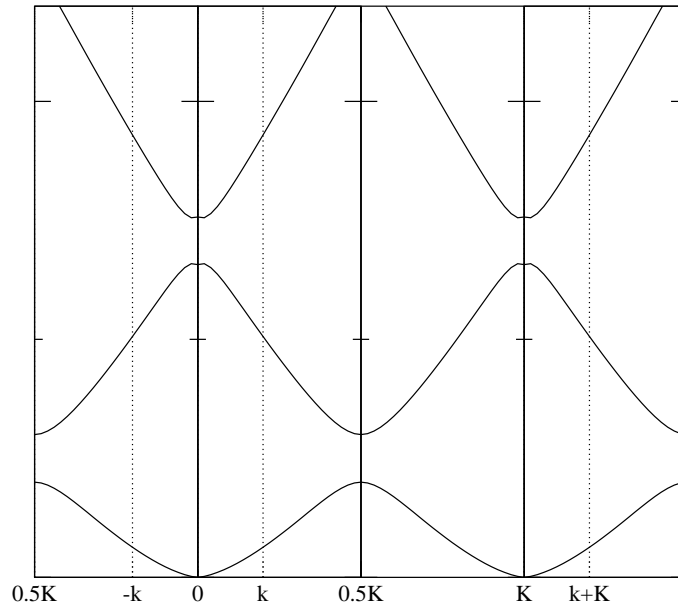


Figure 5.5: Sample band structure similar to nearly-free electrons. The First Brillouin zone's boundary is at  $\frac{1}{2}K$ . Two equivalent  $k$ -points to  $k$  are marked,  $-k$  and  $k + K$ .

concerns permutations of rows and columns. For a finite basis, one gets numerical problems for high-lying states.

The consequence for the band structure is shown for a system similar to nearly-free electrons in Fig. 5.5. The solid vertical lines at  $\frac{1}{2}K, K, \dots$  are the boundaries of the Brillouin zones. The dashed lines indicate one  $k$ -point  $k$  and equivalents of it at  $-k$  and  $k + K$ .

If one now imposes a lower periodicity like  $\tilde{R} = 2R$ , the reciprocal lattice and therewith the Brillouin zone reduces to half the size,  $|k| \leq \tilde{K}, \tilde{K} = \frac{\pi}{L}$ . A denser periodicity of  $\tilde{K} = \frac{K}{2}$  is demanded now instead of  $K$  in the first place, with  $\tilde{K}$ . This makes the point  $-k$  (which is equivalent to  $k$  due to time-reversal) equivalent to  $-k + \tilde{K} = \frac{K}{2} - k$ . Since these two points have (possibly) distinct sets of eigenvalues in the initial setup of high periodicity, these two sets sum up in this setup.

The corresponding band structure is shown in Fig. 5.6. The periodicity of branches has been doubled, the first Brillouin zone shrinks to half the size  $\tilde{K}$ , and the number of bands in it doubled. This figure gives an idea of the origin of the term *backfolding*. The bands look folded back at the center of the former bigger Brillouin zone; but the superposition with an additional band structure is a better way to visualize.

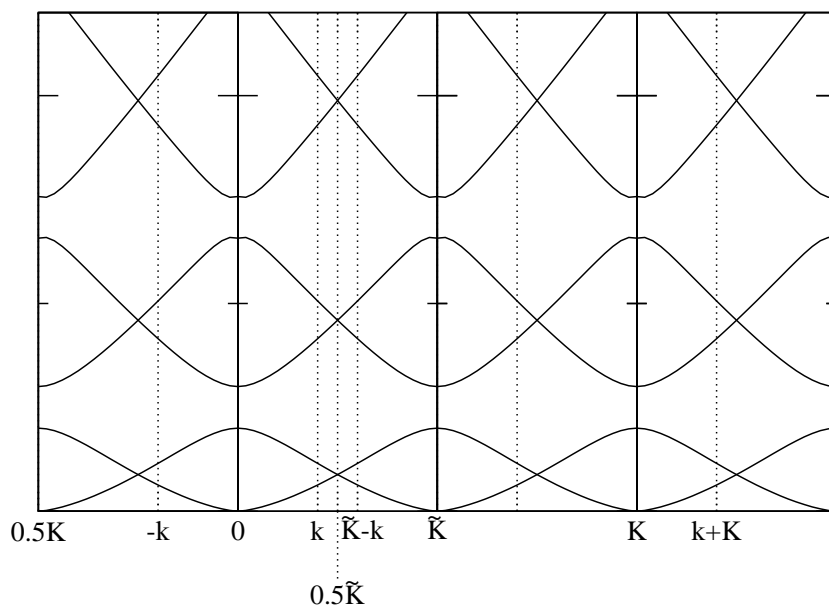


Figure 5.6: Sample band structure for a system for that a lower translational symmetry than in Fig. 5.5 has been used. The new Brillouin zone border is  $\frac{1}{2}\tilde{K}$ . Additionally,  $\tilde{K} - k$  is marked as equivalent to  $k$  now.

## 5.4.2 Representation in a basis

The impact of backfolding on the energy eigenvalues has been shown in the previous paragraph. But the dielectric function essentially depends on the momentum matrix elements and therewith on the wavefunctions. Here, the effect of backfolding should be illustrated for a plane-wave calculation.

For simplicity, I choose a simple, hypothetical system of Aluminum (Al) in a simple cubic (sc) structure<sup>4</sup>. This is calculated in two setups ( $\mathcal{A}$  denotes sets of basis vectors,  $\mathcal{D}$  are atom positions in coordinates of these basis vectors)

$$\mathcal{A}_1 = \left\{ L \begin{pmatrix} 1 \\ 0 \\ 0 \end{pmatrix}, L \begin{pmatrix} 0 \\ 1 \\ 0 \end{pmatrix}, L \begin{pmatrix} 0 \\ 0 \\ 1 \end{pmatrix} \right\}, \quad \mathcal{D}_1 = \left\{ \begin{pmatrix} 0 \\ 0 \\ 0 \end{pmatrix} \right\} \quad (5.49)$$

and

$$\mathcal{A}_2 = \left\{ L \begin{pmatrix} 1 \\ 0 \\ 0 \end{pmatrix}, L \begin{pmatrix} 0 \\ 1 \\ 0 \end{pmatrix}, L \begin{pmatrix} 0 \\ 0 \\ 2 \end{pmatrix} \right\}, \quad \mathcal{D}_2 = \left\{ \begin{pmatrix} 0 \\ 0 \\ 0 \end{pmatrix}, \begin{pmatrix} 0 \\ 0 \\ \frac{1}{2} \end{pmatrix} \right\}, \quad (5.50)$$

<sup>4</sup>So in this context, SC is not meant to be an abbreviation of *self-consistency*, as in the theoretical part before.

that is the second setup doubles the first one in z-direction. The resulting reciprocal lattices (written in form of Bravais matrices, i.e. writing the (transposed) reciprocal basis vectors in matrix form) are

$$\mathcal{B}_1 = \frac{2\pi}{L} \begin{pmatrix} 1 & 0 & 0 \\ 0 & 1 & 0 \\ 0 & 0 & 1 \end{pmatrix}, \quad \mathcal{B}_2 = \frac{2\pi}{L} \begin{pmatrix} 1 & 0 & 0 \\ 0 & 1 & 0 \\ 0 & 0 & \frac{1}{2} \end{pmatrix}, \quad (5.51)$$

the second setup having a Brillouin zone halved in z-direction. The wavefunctions should be expressed in plane-waves for both setups,

$$\psi_i^{(1)}(\mathbf{k}, \mathbf{r}) = \frac{1}{\sqrt{\Omega}} \sum_{\mathbf{G}_1 \in \mathcal{G}_1} C_{\mathbf{k}+\mathbf{G}}^{(1)i} \phi_{\mathbf{k}+\mathbf{G}_1}(\mathbf{r}), \quad (5.52)$$

$$\psi_i^{(2)}(\mathbf{k}, \mathbf{r}) = \frac{1}{\sqrt{2\Omega}} \sum_{\mathbf{G}_2 \in \mathcal{G}_2} C_{\mathbf{k}+\mathbf{G}_2}^{(2)i} \phi_{\mathbf{k}+\mathbf{G}_2}(\mathbf{r}), \quad (5.53)$$

with  $\Omega$  the volume of the small unit cell,  $\mathcal{G}_1$ ,  $\mathcal{G}_2$  the two sets of  $\mathbf{G}$ -vectors. The  $\varphi$  are the common plane-wave basis functions

$$\phi_{\mathbf{k}+\mathbf{G}}(\mathbf{r}) = e^{i(\mathbf{k}+\mathbf{G})\mathbf{r}}. \quad (5.54)$$

As a result of the smaller Brillouin zone the set of  $\mathbf{G}$  vectors in the second setup is double as dense as in the first one, see Fig. 5.7. Since we cut a sphere of  $|\mathbf{G}| \leq G_{max}$ ,

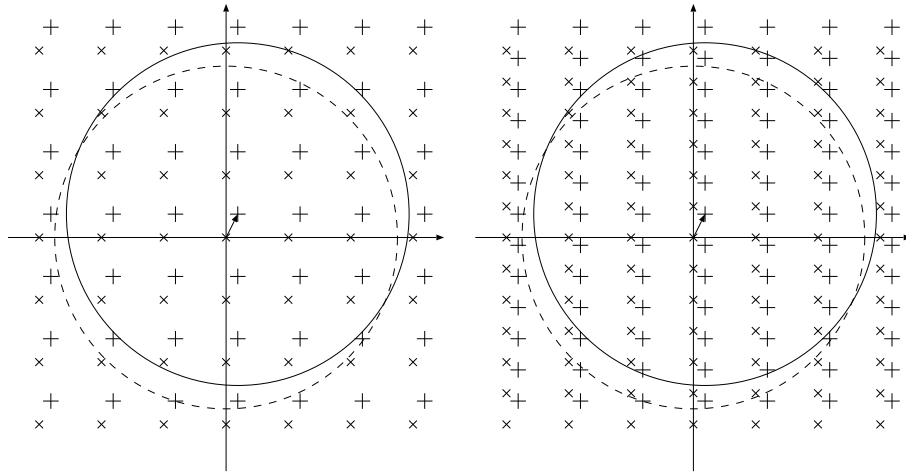


Figure 5.7: The  $k_x - k_z$ -plane of the reciprocal lattices for the two setups. Basis vectors are indicated by x-like crosses,  $(\mathbf{k} + \mathbf{G})$ -vectors for one special  $\mathbf{k}$  drawn in the origin by plus-like crosses.

the set  $\mathcal{G}_2$  contains approximately double the number of vectors. So for every vector

$\mathbf{G}$  out of  $\mathcal{G}_1$  we assign a vector

$$\underline{\mathbf{G}} = \mathbf{G} + \tilde{K}, \quad \tilde{K} = (0, 0, \frac{\pi}{L}), \quad (5.55)$$

so that all the vectors  $\{\mathbf{G}, \underline{\mathbf{G}}\}$  form the second set  $\mathcal{G}_2$ . This assignment works only approximately due to the shape of the sphere, but is valid for a sufficient expansion cut-off  $G_{max}$ : Since the influence (i.e. the magnitude of the expansion coefficient) of large  $G$ -vectors vanish in the case of a valid convergence, the discrepancy can be neglected. So we can take  $\mathcal{G}_2$  double as large as  $\mathcal{G}_1$ , and omit indices to the  $G$ -vectors since it should be clear from the context which vectors are referred to.

Let's watch the generalized eigenvalue problem (2.22). Since the plane-wave are orthogonal, the overlap has unit shape:

$$[\mathcal{H}(\mathbf{k}) - \epsilon(\mathbf{k})\mathbb{1}]\mathbf{c}(\mathbf{k}) = 0. \quad (5.56)$$

For the two setups the elements of these matrices read (see (4.6))

$$\begin{aligned} \mathcal{H}_{\mathbf{G}, \mathbf{G}'}^{(1)}(\mathbf{k}) &= \frac{\hbar^2}{2m} |\mathbf{k} + \mathbf{G}|^2 \delta_{\mathbf{G}\mathbf{G}'} + V_{(\mathbf{G}-\mathbf{G}')}^{(1)}, & V_{(\mathbf{G}-\mathbf{G}')}^{(1)} &= \frac{1}{\Omega} \int_{uc_1} d^3r e^{-i(\mathbf{G}-\mathbf{G}')\mathbf{r}} V_{eff}(\mathbf{r}) \\ \mathcal{H}_{\mathbf{G}, \mathbf{G}'}^{(2)}(\mathbf{k}) &= \frac{\hbar^2}{2m} |\mathbf{k} + \mathbf{G}|^2 \delta_{\mathbf{G}\mathbf{G}'} + V_{(\mathbf{G}-\mathbf{G}')}^{(2)}, & V_{(\mathbf{G}-\mathbf{G}')}^{(2)} &= \frac{1}{2\Omega} \int_{uc_2} d^3r e^{-i(\mathbf{G}-\mathbf{G}')\mathbf{r}} V_{eff}(\mathbf{r}), \end{aligned} \quad (5.57)$$

integrations performed over the real space units cells one ( $uc_1$ ) and two ( $uc_2$ ).

Now we want to relate the Hamilton matrices of the two systems. Since the function  $V_{eff}$  is periodic in the first unit cell  $uc_1$  (thus twice periodic in  $uc_2$ ), and an exponential  $\exp(i(\mathbf{G} - \underline{\mathbf{G}}')\mathbf{r})$  is simple periodic in  $uc_2$ , contributions of the potential of mixed  $G$ -vectors vanish:

$$V_{(\mathbf{G}-\underline{\mathbf{G}}')}^{(2)} = V_{(\underline{\mathbf{G}}-\mathbf{G}')}^{(2)} = 0. \quad (5.58)$$

If we therefore rearrange the vectors of  $\mathcal{G}_2$  when applying them on  $\mathcal{H}$  to group the vectors of  $\mathcal{G}_1$  first, we obtain for the Hamiltonian the block form

$$\mathcal{H}^{(2)} = \begin{pmatrix} \mathcal{H}^{(2a)} & 0 \\ 0 & \mathcal{H}^{(2b)} \end{pmatrix}, \quad (5.59)$$

the submatrix (a) taking the contributions of the undashed, (b) taking those of the dashed  $G$ -vectors.

Contributions  $(\underline{\mathbf{G}} - \underline{\mathbf{G}}')$  to the potential are identical to contributions  $(\mathbf{G} - \mathbf{G}')$  of the corresponding undashed  $G$ -vectors. In the formula for the potential, the

double integration range cancels with the factor  $\frac{1}{2}$  in front of the integral, and the contribution is the same as in the small setup:

$$V_{(\underline{\mathbf{G}}-\underline{\mathbf{G}}')}^{(2)} = V_{(\mathbf{G}-\mathbf{G}')}^{(2)} = V_{(\mathbf{G}-\mathbf{G}')}^{(1)}. \quad (5.60)$$

Since the kinetic part of  $\mathcal{H}^{(2a)}$  is identical to  $\mathcal{H}^{(1)}$ , so is the whole submatrix. Let's turn focus on  $\mathcal{H}^{(2b)}$ . It reads

$$\mathcal{H}_{\underline{\mathbf{G}},\underline{\mathbf{G}}'}^{(2b)}(\mathbf{k}) = \frac{\hbar^2}{2m} |\mathbf{k} + \underline{\mathbf{G}}|^2 \delta_{\underline{\mathbf{G}}\underline{\mathbf{G}}'} + V_{(\underline{\mathbf{G}}-\underline{\mathbf{G}}')}. \quad (5.61)$$

We assume time reversal symmetry, i.e.  $\mathcal{H}(\mathbf{k})$  yields the same set of eigenvectors and eigenvalues for  $-\mathbf{k}$ . We apply this on our submatrix  $\mathcal{H}^{(2b)}$ . Because of  $\underline{\mathbf{G}} = \mathbf{G} + \tilde{K}$  and (5.60), our matrix elements are equivalent to

$$\mathcal{H}_{\underline{\mathbf{G}},\underline{\mathbf{G}}'}^{(2b)}(\mathbf{k}) = \frac{\hbar^2}{2m} |(\tilde{K} - \mathbf{k}) + \mathbf{G}|^2 \delta_{\mathbf{G}\mathbf{G}'} + V_{(\mathbf{G}-\mathbf{G}')} \quad (5.62)$$

$$= \mathcal{H}_{\mathbf{G},\mathbf{G}'}^{(1)}(\tilde{K} - \mathbf{k}). \quad (5.63)$$

With defining a backfolding operator  $\mathcal{T}_k : \mathbf{k} \rightarrow \tilde{K} - \mathbf{k}$ , the Hamiltonian reads

$$\mathcal{H}^{(2)}(\mathbf{k}) = \begin{pmatrix} \mathcal{H}^{(1)}(\mathbf{k}) & 0 \\ 0 & \mathcal{H}^{(1)}(\mathcal{T}_k \mathbf{k}) \end{pmatrix}. \quad (5.64)$$

The spectrum of such a matrix is the sum of the spectra of the submatrices. The eigenvectors are filled up with zeros in its additional components. If the small setup has the eigenvalues and eigenvectors

$$\{\epsilon_j^{(1)}(\mathbf{k})\}, \quad \{|j\mathbf{k}\rangle\} = \left\{ \left( C_{(\mathbf{k}+\mathbf{G})}^{(1)j} \right) \right\}, \quad (5.65)$$

those of the large setup are

$$\begin{aligned} \{\epsilon_i^{(2)}(\mathbf{k})\} &= \{\epsilon_j^{(1)}(\mathbf{k})\} \cup \{\epsilon_j^{(1)}(\mathcal{T}_k \mathbf{k})\} \quad \text{and} \\ \{|i\mathbf{k}\rangle\} &= \left\{ \left( \begin{pmatrix} C_{(\mathbf{k}+\mathbf{G})}^{(1)j} \\ 0 \end{pmatrix} \right) \right\} \cup \left\{ \left( \begin{pmatrix} 0 \\ C_{(\mathcal{T}_k \mathbf{k}+\mathbf{G})}^{(1)j} \end{pmatrix} \right) \right\} \end{aligned} \quad (5.66)$$

(with  $j$  ( $i$ ) running over all bands of the small (large) system).

It should be noted that the derivations given above only fit approximately, due to the finite set of  $\mathbf{G}$ -vectors. This is illustrated in Fig. 5.7, where a sample cutting sphere is plotted. For such a small set of vectors, it is barely possible to make a reasonable mapping (5.55). This effect should diminish for an increasing number of basis functions.

The experience shows that the distinction (5.66) into two different kinds of eigenvectors is also valid for the same system in an LAPW basis. This has been tested for the calculation presented in the next subsection.

However, if the backfolding involves a more complex transformation of basis vectors, these results – the form of the eigenvectors (5.66) – do not stand strictly anymore.

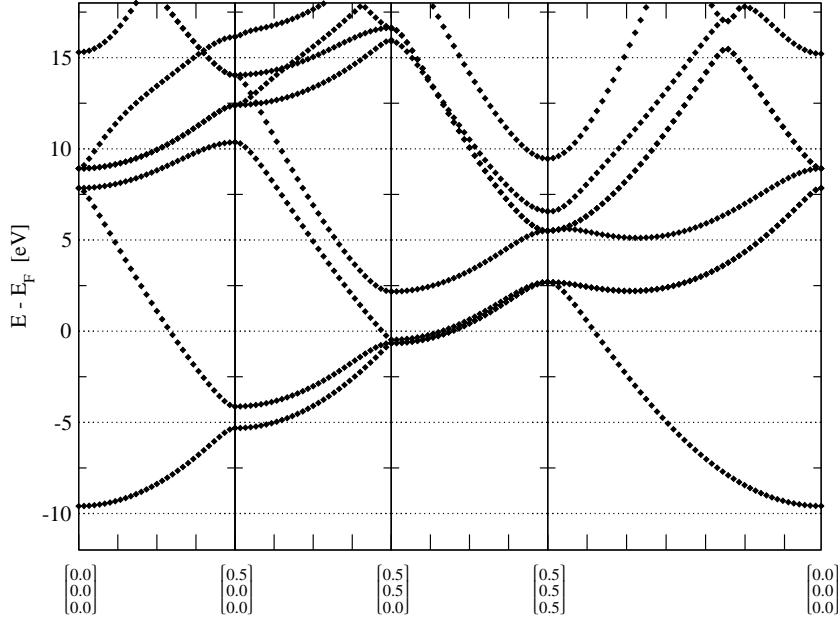


Figure 5.8: Band structure for fcc Aluminum, setup 1 (small unit cell).

### 5.4.3 Illustration

This effect should be demonstrated now by some band structures for this system. Figs. 5.8 and 5.9 show the band structures for the two systems along the path  $(0,0,0) \rightarrow (\frac{1}{2}, 0, 0) \rightarrow (\frac{1}{2}, \frac{1}{2}, 0) \rightarrow (\frac{1}{2}, \frac{1}{2}, \frac{1}{2}) \rightarrow (0,0,0)$ , each in internal coordinates. Due to the symmetry mentioned above, every plot  $\mathbf{k}_1 \rightarrow \mathbf{k}_2$  in the large system is the sum of the plots  $\mathbf{k}_1 \rightarrow \mathbf{k}_2$  and  $(\tilde{K} - \mathbf{k}_1) \rightarrow (\tilde{K} - \mathbf{k}_2)$  of the small system (with  $\tilde{K} = (0, 0, \frac{2\pi}{L})$ ).

Due to the simple kind of backfolding in this setup, one sees the backfolding nicely in a plot along z-direction. In Fig. 5.10 the path  $(\frac{1}{2}, \frac{1}{2}, 0) \rightarrow (\frac{1}{2}, \frac{1}{2}, \frac{1}{2})$  is shown, that is the third section of Fig. 5.9. The band structure of the large system is given by that of the small system overlapped with the additional path  $(\frac{1}{2}, \frac{1}{2}, \frac{1}{2}) \rightarrow (1, \frac{1}{2}, \frac{1}{2})$ .

In Fig. 5.11 the band structure  $(0,0,0) \rightarrow (\frac{1}{2}, 0, 0)$  is plotted. The bands of the large system on the right are those of the small system along the same line on the

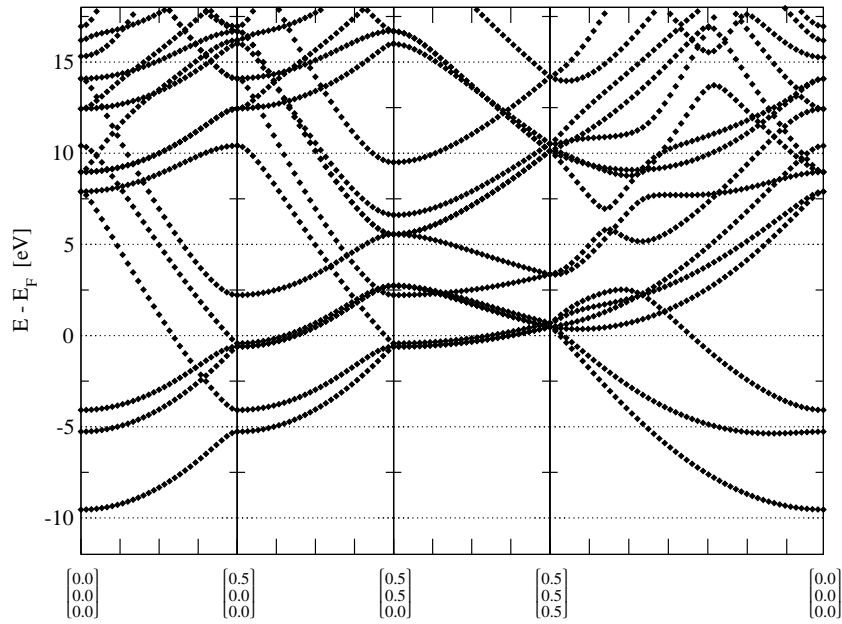


Figure 5.9: Band structure for scc Aluminum, setup 2 (large unit cell).

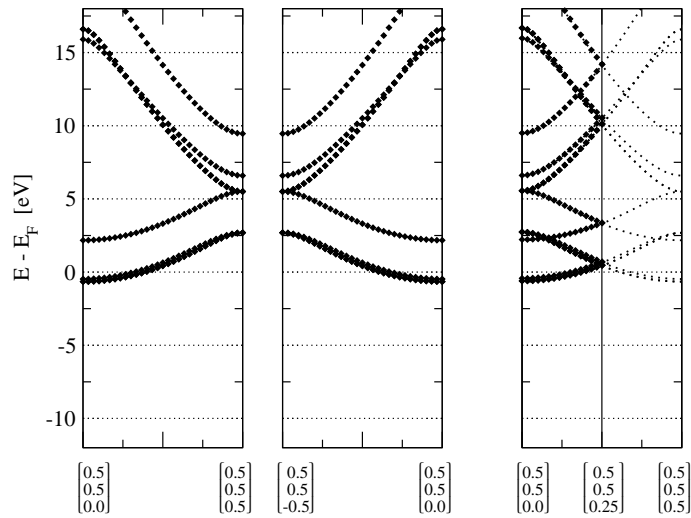


Figure 5.10: Backfolded band structure parallel to z-direction. On the left two band structures of the small system are shown that overlap to the band structure of the large system on the right.

very left, superposed by the bands  $(0, 0, \frac{1}{2}) \rightarrow (\frac{1}{2}, 0, \frac{1}{2})$ . Here it is already difficult to distinguish the two kinds of bands by a simple glimpse.

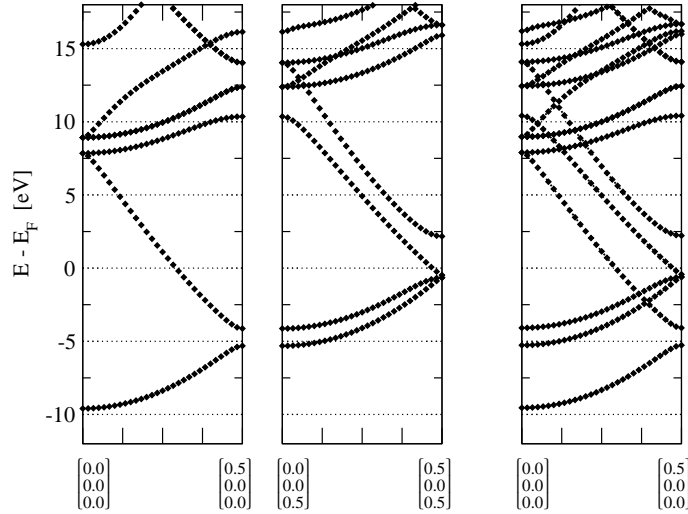


Figure 5.11: Backfolded band structure perpendicular to z-direction. The right band structure (large setup) is the sum of the two on the left (small setup).

#### 5.4.4 Consequences for computation

The calculation of a physical property (i.e. the expectation value of a hermitian operator) must be the same whatever choice of the unit cell has been made. Since the band structures change, one might get the impression that this rule is violated.

One essential ingredient of the dielectric function (3.61) are the transitions from one band to another, that is a double sum over occupied and unoccupied states. This summation will change if the band structure changes. The joint density of states (JDOS) for example, given by (3.62), relies on these transitions only, meaning only on the gradient of the energy differences. It does not depend additionally on matrix elements like the dielectric function (3.61). This leads to different results for a backfolded setup.

To show this, the dielectric function (3.61) is plotted in graph 5.12 with matrix elements neglected, i.e. the numerator equal to one. Though not the same quantity, this term suffers the same effect with respect to backfolding as the JDOS does. It can diverge for small energies due to the factor  $\frac{1}{\omega^2}$ . This difference for the two setups does not contradict physics since the JDOS is not an observable and does not have a physical meaning by itself.

The difference of the dielectric function for the two different unit cells in the small graph in Fig. 5.12 results from the  $k$ -points being double as dense for the large setup as for the small one (the same number of  $k$ -points was used), and from the remaining effects of the additional bands. Furthermore one sees by comparing the two curves for the small setup (black curve with markers on the right, and the

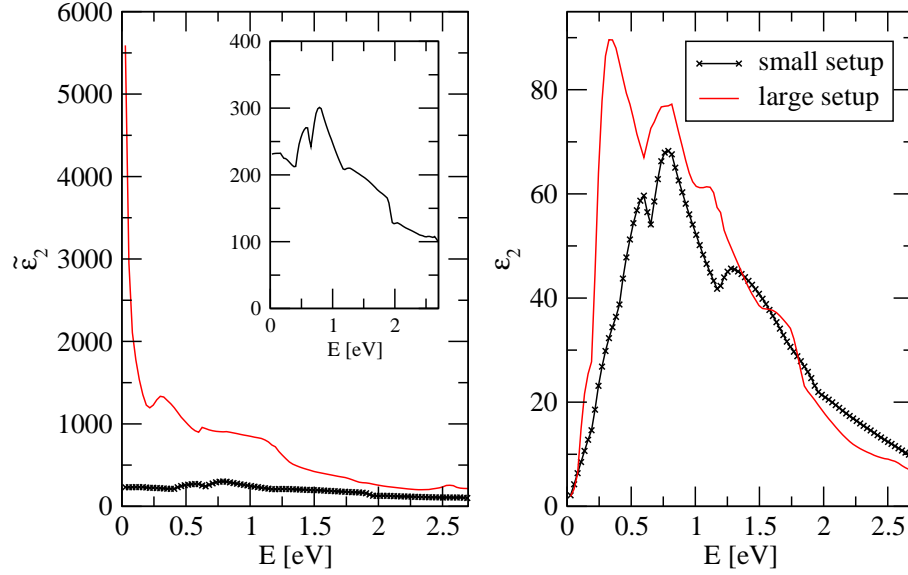


Figure 5.12: Dielectric function of scc Aluminum without inclusion of matrix elements  $\tilde{\epsilon}_2$  on the left and with inclusion of matrix elements  $\epsilon_2$  on the right. Both graphs show the results for the large setup (red curve) and the small setup (black curve with markers). The small graph on the left  $\tilde{\epsilon}_2$  of the small system is enlarged. 288  $k$ -points have been used.

small graph on the left) that the pure band structure (i.e. neglecting the momentum matrix elements) already possesses some of the characteristics, e.g. the two peaks at  $0.6\text{eV}$  and  $0.8\text{eV}$ . Other characteristics (like the decrease for small frequencies) are obtained only by including the matrix elements.

The dielectric function on the other hand yields the same results for both setups due to the momentum matrix elements included in its mathematical description. These matrix elements have the property to vanish if being applied on a regular and a backfolded eigenfunction:

$$\langle f\mathbf{k}|\nabla|i\mathbf{k}\rangle = 0 \quad \text{for a backfolded transition,} \quad (5.67)$$

that is one state of  $i$  or  $f$  being backfolded, the other one regular. For the simple setup of Section 5.4, this can be seen easily from the form of the eigenvectors (5.66) and the form of the matrix elements in plane-wave basis (4.7).

## 5.5 Resulting problems in the integration

Up to now, the interesting insights of the previous section do not pose any analytical problems. But in the numerical treatment, problems appear due to the interpolation

between  $k$ -points made in the integration scheme described above. The two different kinds of problems encountered in the implementation are described in this section.

Before describing the details, one should remember the way a computer handles bands. A human can connect  $k$ -points logically to bands by watching a band-structure, or can give it a mathematical character. Initially, computers can only enumerate the eigenvalues, and uses the according eigenvectors. It needs additional effort [YKS] to recognize band crossings.

### 5.5.1 The Influence of Degeneracy

The first problem with backfolding arises at points with degenerated energy eigenvalues. At these points the eigenvectors are determined only up to linear combinations of each other. (This means that the matrix elements are not unique for eigenvectors with degenerated eigenvalues, even not for an observable like the momentum. In the case of the dielectric function that contains *transitions* from one level to another, only the sum over these transitions – as it is contained in (3.61) – gives a unique value.) An example for degenerated eigenvalues is sketched in Fig. 5.13. For instance,  $k_3$  could be the zone boundary. It is known that the matrix elements vanish for a degenerate energy eigenvalues,

$$\langle f\mathbf{k}_g|\nabla|i\mathbf{k}_g\rangle = 0 \quad \text{for} \quad E_i(\mathbf{k}_g) = E_f(\mathbf{k}_g), \quad (5.68)$$

as in our case. (This is shown by Mavropoulos, Papanikolaou and Dederichs [MPD03].) It should be valid in the limit  $\mathbf{k} \rightarrow \mathbf{k}_g$ , too. Therefore, one should not expect problems from this.

The situation is different if you consider transitions to another band  $c$  in a system possessing backfolding. In the last named figure, let bands  $a$  and  $c$  be regular, while  $b$  is backfolded. Transitions  $b \rightarrow c$  should not give any contributions. This is consistent with the image that according to (5.66), the eigenvectors of bands  $b$  and  $c$  have the form

$$|ak\rangle \sim \begin{pmatrix} * \\ 0 \end{pmatrix}, \quad |bk\rangle \sim \begin{pmatrix} 0 \\ * \end{pmatrix}, \quad |ck\rangle \sim \begin{pmatrix} * \\ 0 \end{pmatrix}, \quad k \in (k_1, k_3). \quad (5.69)$$

At  $k_3$ , however, due to the intermixture of  $a$  and  $b$ , the eigenvectors take the form

$$|ak\rangle \sim \begin{pmatrix} * \\ * \end{pmatrix}, \quad |bk\rangle \sim \begin{pmatrix} * \\ * \end{pmatrix}, \quad (5.70)$$

resulting in a matrix element  $M_{cb}(k_3) \neq 0$ . In the analytical solution this is no problem due to the singularity of this point (or plane in three dimensions, respectively). In a linear interpolation scheme, though, this leads to finite contributions, as sketched in the small picture in Fig. 5.13.

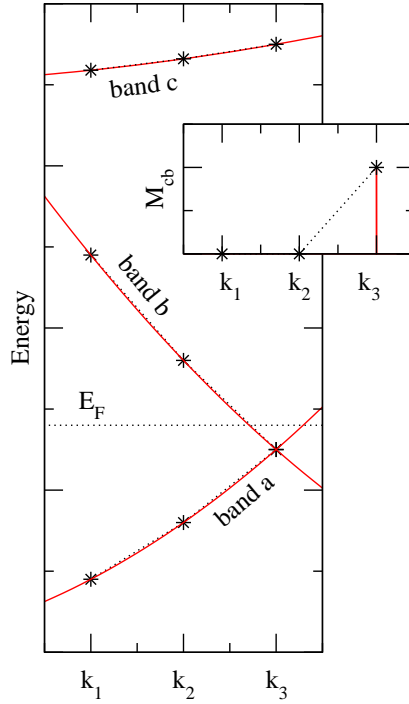


Figure 5.13: One-dimensional illustration of degeneracy. The straight red lines are the true bands, while the dotted black ones are interpolated linearly from the energy values (plotted as stars) at the mesh points  $k_1, k_2, k_3$ . The horizontal dotted line indicates the Fermi energy. In the small picture, a linear interpolation is sketched in dotted black, the true discontinuous path in solid red.

**A possible solution:** It is neither common nor possible without additional numerical effort to determine the “natural form”  $|\nu \mathbf{k}_g\rangle_n$  of the wavefunctions at a  $k$ -point  $\mathbf{k}_g$  possessing degeneracy (that would be  $|\nu \mathbf{k}_g\rangle_n = \lim_{\mathbf{k} \rightarrow \mathbf{k}_g} |\nu \mathbf{k}\rangle$ ). Furthermore it is quite improbable (if possible at all with limited numerical precision) for a sample  $k$ -point within the irreducible Brillouin zone to hit a point of degeneracy. On the other hand degeneracy on the Brillouin zone’s boundary (and at high symmetry points in it, which are in turn boundaries of the irreducible part of the Brillouin zone) is very common. Experience affirms that matrix elements like  $M_{cb}(k)$  quickly vanish when moving off the high symmetry (see next subsection).

Therefore a simple solution is just to shift all  $k$ -points marginally off the boundary inside the irreducible wedge. If backfolding is absent, this leads to only a marginal but noticeable error, due to the quick variations of the matrix elements close to high-symmetry planes. In the presence of backfolding, the effect is similar to neglecting the matrix elements (shown in Fig. 5.12): The dielectric function will get additional contributions due to wrong interpolation, especially big values for small frequencies.

### 5.5.2 The Influence of Band crossing

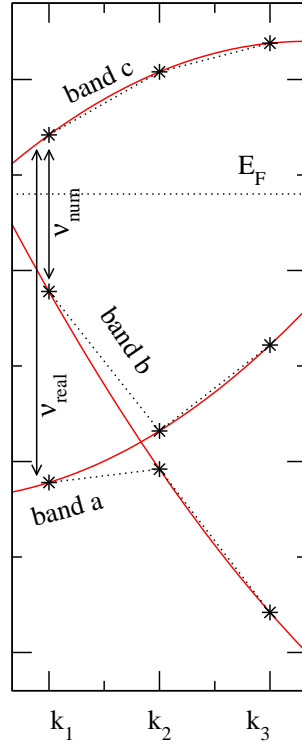


Figure 5.14: One-dimensional example for band crossing. The straight red lines are the true bands, while the dotted black lines are interpolated from the energy values (plotted as stars) at the mesh points  $k_1, k_2, k_3$ . Fermi energy is dotted in the upper third.

In the case of band crossing, the interpolation errors have a significant influence. This is illustrated for a one-dimensional example in Fig. 5.14. The true bands are approximated linearly from the energy values at three sampling  $k$ -points  $k_1, k_2, k_3$ . As in the sketch before the bands are labeled  $a, b, c$ . For a human observer this refers the true bands, while a computer gives these labels to the eigenvalues ordered from bottom to up.

Let the bands  $a$  and  $c$  be regular, while band  $b$  is backfolded, and focus on the interval  $[k_1, k_2]$ . According to (5.66) the eigenvalues at  $k_1$  take the form

$$|ak_1\rangle \sim \begin{pmatrix} * \\ 0 \end{pmatrix}, \quad |bk_1\rangle \sim \begin{pmatrix} 0 \\ * \end{pmatrix}, \quad |ck_1\rangle \sim \begin{pmatrix} * \\ 0 \end{pmatrix}, \quad (5.71)$$

and the form

$$|ak_2\rangle \sim \begin{pmatrix} 0 \\ * \end{pmatrix}, \quad |bk_2\rangle \sim \begin{pmatrix} * \\ 0 \end{pmatrix}, \quad |ck_2\rangle \sim \begin{pmatrix} * \\ 0 \end{pmatrix} \quad (5.72)$$

at point  $k_2$ . This results in matrix elements for a transition  $b \rightarrow c$  of the form

$$M_{cb}(k_1) = 0, \quad \text{but} \quad M_{cb}(k_2) \neq 0. \quad (5.73)$$

Due to the non-vanishing matrix element at  $k_2$ , the matrix element is interpolated in  $[k_1, k_2]$  continuous in the range  $[0, M_{cb}(k_2)]$ . In the given example, this results in transitions at low frequencies  $\nu_{num}$  (see Fig. 5.14), while analytically (and for an infinitely dense mesh) only transitions down to  $\nu_{real}$  are possible in this interval.

Though also occurring in the absence of backfolding, the impact on calculations are stronger with backfolding present due to the larger number of bands. Further on, the differences resulting from matrix elements equal zero being interpolated incorrectly are crucial, especially for small energies due to the factor  $\frac{1}{\omega^2}$  that goes into the dielectric function (3.61).

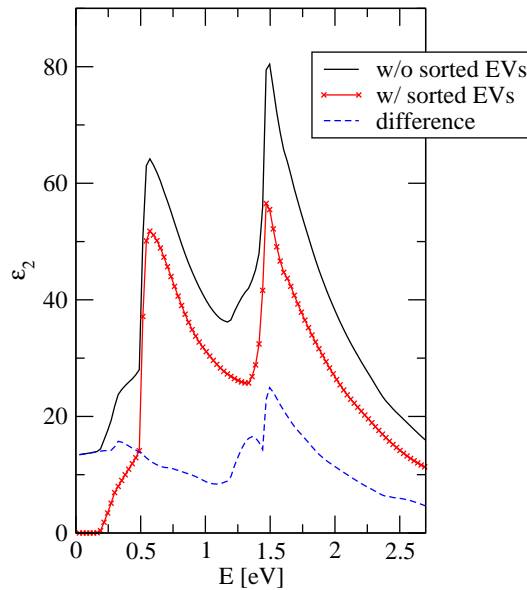


Figure 5.15: Dielectric function for fcc Aluminum, with and without sorted eigenvalues to correct crossing with backfolded bands (288  $k$ -points).

**An approach to avoid the problem:** A method to minimize the contribution of backfolding to this effect is to renumber the bands. This is possible up to a certain point for crossings of regular bands with backfolded ones, as mentioned earlier (5.66).

In Fig. 5.15, this method has been applied to aluminum for a mesh of 288  $k$ -points. Only with this method one restores the correct absorption edge of the curve. Calculations show that without reordering of bands, this effect is still present for a calculation involving 11000  $k$ -points (likewise in the irreducible BZ).

The higher the eigenvalues are, and the closer the  $k$ -points to high symmetry positions, the worse is classification into regular and backfolded ones. The first item is not too serious because transitions of higher energy contribute less to the dielectric function, due to the prefactor  $\frac{1}{\omega^2}$ . Second one can assume band crossings of regular and backfolded bands not to appear in the very close vicinity of high-symmetry planes. Starting from this one can hope to get good results with this method.

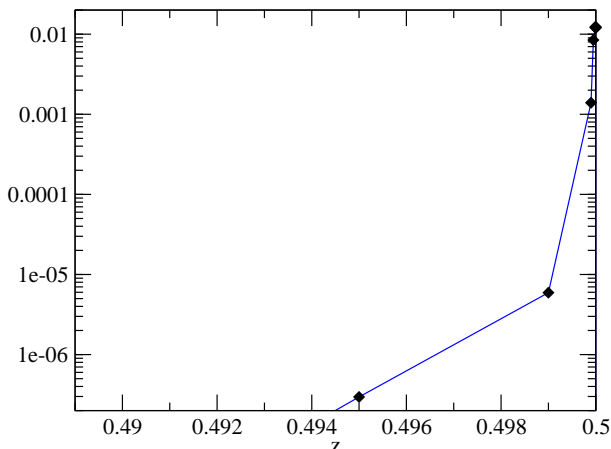


Figure 5.16: The overlap of wavefunctions 1 and 2 of an fcc Copper system.

In Fig. 5.16 the actual decay of overlap and absolute value of matrix elements is shown. The observed system is the second test system in Section 5.7, fcc Copper. The two lowest bands are examined along the  $k$ -vectors  $(z, z, z)$  for  $z \in [0.499, 0.5]$ . The plot is double logarithmic. It gives an idea of how far to shift  $k$ -points off the boundary so that the matrix elements vanish (as they should) and the bands can be classified correctly.

## 5.6 A Note on Computational Demands

For sophisticated spectral computations you need an adequate set of  $k$ -points – possibly in the order of thousands. This meets the fact that for large systems with a big number of electrons, the number of transitions roughly scales quadratically to it. Together this can result in significant demands of computer memory, so that one has to consider how to provide these matrix elements to your integration routine.

It turns out that the calculation of the matrix elements (and herein the interstitial contribution) is the major computational effort. So one can calculate the MMEs in advance, resulting in minimal computational costs and biggest memory demands. On the other hand the matrix elements can be computed on-the-fly, abandon the use of the big array memory, but needing to calculate the same matrix elements several

times. In between, you can try to cache selected elements in memory to combine the advantages of both approaches with minimal drawbacks.

At this point, the special way of connections of your  $k$ -points to tetrahedra and the order of tetrahedra can be of big help. For instance, regard a typical tetrahedra set connecting nearest neighbors in a set of  $n_k$   $k$ -points equidistant in the three spatial coordinates. This tetrahedra should be arranged in layers, e.g. in  $z$ -direction, with the same order in each layer (according to the layer shape which may differ).

If one processes the tetrahedra sequentially, the data of the corresponding  $k$ -points (including the matrix elements) are not needed only for a short time. Conversely, even if one does not want to calculate the matrix elements multiple times, you need to store only  $n_{sim}$  matrix elements at the same time, where  $n_{sim}$  can be considerably smaller than  $n_k$ .

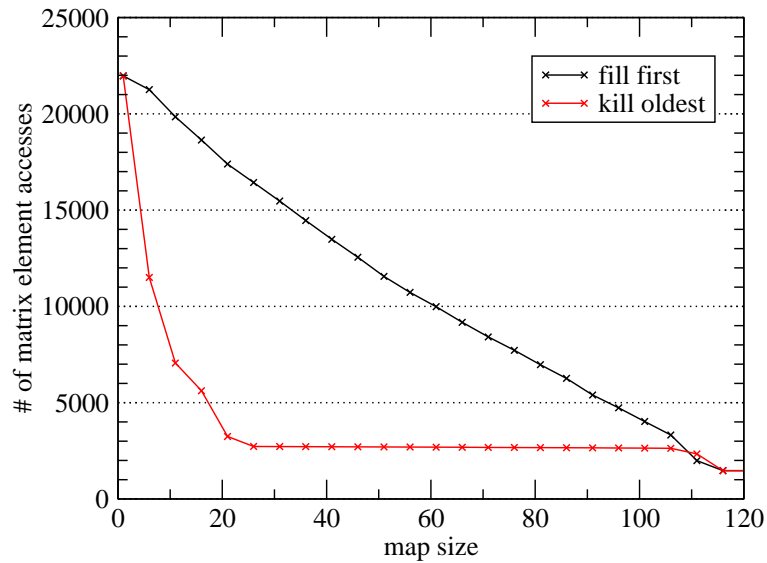


Figure 5.17: Computational amount depending on cache size (1470  $k$ -points, 6591 tetrahedra).

If you take a cache smaller than these  $n_{sim}$  entries, you will have to calculate matrix elements partly again since you have to skip some which you need later. But you can still take good advantage of that method, depending on which matrix elements you skip. In Fig. 5.17 this is illustrated for a  $k$ -point of 1470 points (it is a prism-shaped box with 14 equidistant points per edge), giving 6591 tetrahedra. Only matrix elements for  $n_{sim} = 116$   $k$ -points are needed simultaneously not to calculate them repeatedly.

If you lower the size of your cache below this value, your number of calculations increase, depending on your strategy. The point (116, 1470) at the lower right is the starting point of a complete caching. If the cache is full when a matrix element

should be stored, the first strategy writes the new element in the beginning of the cache, while the second one looks for the oldest element in cache. Though the number of computations quickly nearly doubles for a small decrease of cache size ( $\sim (106, 2650)$ ), it stays below 3000 – roughly double the computational amount – for even a fifth of the starting size.

As already mentioned, the calculation of the momentum matrix elements consumes most of the CPU time. In the current implementation the contribution of the interstitial according to (5.9) is costly. Investigations gave a ration between 75% and more than 95%, depending on the system size. In future we plan to replace this routine (including a double summation over  $\mathbf{G}$ -vectors) by an FFT technique.

## 5.7 Test calculation

The parameters used for these systems as well as for the systems calculated in Chapter six are listed in appendix D.

### 5.7.1 Aluminum

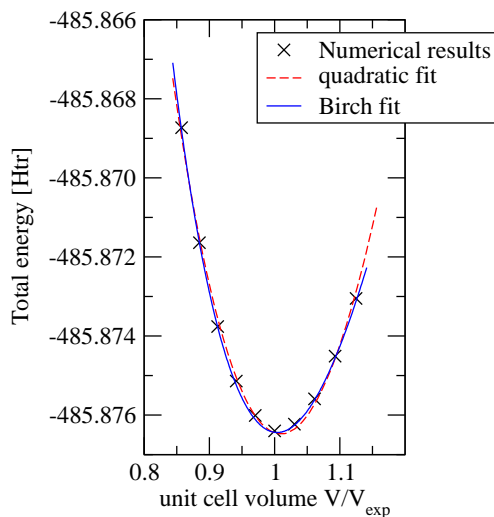


Figure 5.18: Total energy against the volume of the unit cell relative to the experimental value, i.e.  $\frac{V}{V_{exp}} = \left(\frac{L}{L_{exp}}\right)^3$ .

In nature, Aluminum exists in the face-centered cubic configuration. This can

be modeled in the basis

$$\mathcal{A}_1 = L \begin{pmatrix} \frac{1}{2} & \frac{1}{2} & 0 \\ \frac{1}{2} & 0 & \frac{1}{2} \\ 0 & \frac{1}{2} & \frac{1}{2} \end{pmatrix}, \quad \mathcal{B}_1 = \frac{2\pi}{L} \begin{pmatrix} 1 & 1 & -1 \\ 1 & -1 & 1 \\ -1 & 1 & 1 \end{pmatrix} \quad (5.74)$$

of real and reciprocal space. In the current calculation it is modeled in the real-space and reciprocal-space basis

$$\mathcal{A}_2 = L \begin{pmatrix} \frac{1}{2} & \frac{1}{2} & 0 \\ \frac{1}{2} & -\frac{1}{2} & 0 \\ 0 & 0 & 1 \end{pmatrix}, \quad \mathcal{B}_2 = \frac{2\pi}{L} \begin{pmatrix} 1 & 1 & 0 \\ 1 & -1 & 0 \\ 0 & 0 & 1 \end{pmatrix}, \quad (5.75)$$

with two atoms per unit cell on internal coordinates  $(0, 0, 0)$  and  $\frac{1}{2}(1, 1, 1)$ . The lattice parameter was varied and is plotted against the total energy in Fig. 5.18. Birch [Bir78] gives a relation for the total energy of a crystal against the volume  $V$ . For hydrostatic compression of cubic crystals, the strain tensor  $e_{\alpha\beta}$  reduces to a scalar  $e$ . For the limit  $e \rightarrow 0$  the energy reads

$$E(V) = E_0 + \frac{9}{8}K_0V_0 \left[ \left( \frac{V_0}{V} \right)^{\frac{2}{3}} - 1 \right]^2, \quad (5.76)$$

with  $E_0$  the energy of the equilibrium state,  $V_0$  it's volume, and  $K_0 = -V \left( \frac{\partial P}{\partial V} \right) \Big|_{V=V_0}$  is the modulus of compression (or bulk compression) in equilibrium. In this case, the calculation reproduces the experimental lattice constant nearly exactly, with a deviation of 0.3 percent,  $L_{num} = 1.003L_{exp}$ . Though the curve of a quadratic fit does not differ significantly, the location of the minimum is different.

A band structure (along the same path as those in Section 5.4) is shown in Fig. 5.19, together with the density of states. The  $3s$  electrons of this system show a behavior similar to free electrons, as can be seen in the parabola-like bands in the band structure, and in the square-root-like DOS. One can compare these results to those of the simple-cubic systems in Section 5.4.

The (imaginary) dielectric function has already been shown in Fig. 5.15 for a small number of  $k$ -points to demonstrate the influence of the sorting of eigenvalues. In Fig. 5.20 it is shown for different larger number of  $k$ -points. It shows the slow convergence known from literature. Furthermore, two characteristic peaks are located at 0.5eV and 1.6eV.

**Literature:** Experimental data have been obtained by Ehrenreich and Phillips [EPS63]. A first computational approach has been made by Brust [Bru70]. An analysis combining data from reflectance, ellipsometry and other measurements is presented in [SSIS80]. An analysis of aluminum within the APW method has been done by Szmulowicz and Segall [SS81]. One plot from this article is shown in Fig. 5.20.

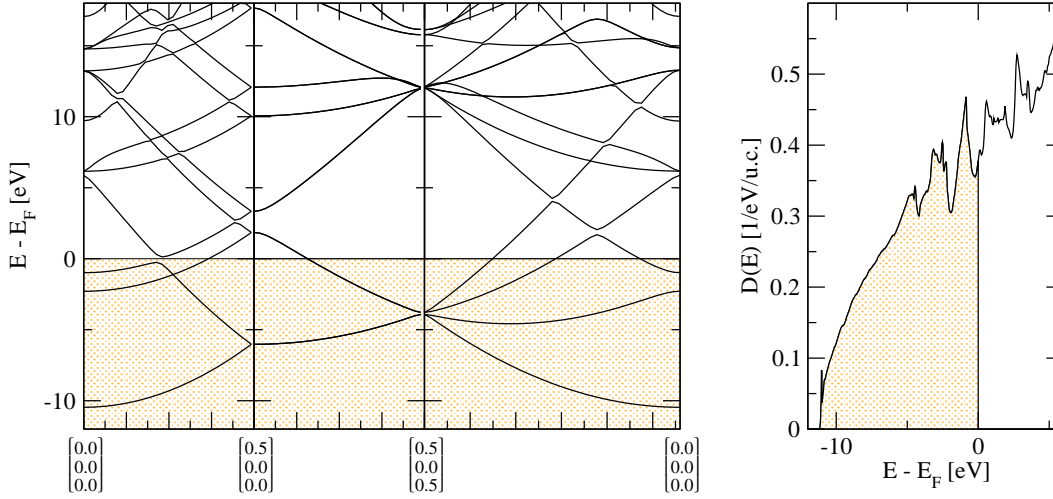


Figure 5.19: The band structure  $(0, 0, 0) \rightarrow (\frac{1}{2}, 0, 0) \rightarrow (\frac{1}{2}, \frac{1}{2}, 0) \rightarrow (\frac{1}{2}, \frac{1}{2}, \frac{1}{2}) \rightarrow (0, 0, 0)$  of Aluminum in fcc coordination is shown on the left. The right plot contains the according Density of states.

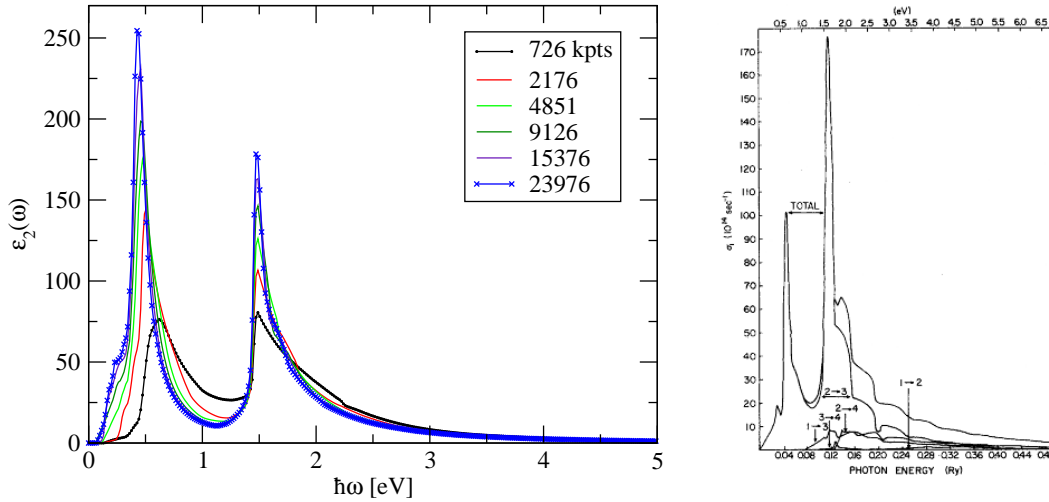


Figure 5.20: The imaginary part of the dielectric function for fcc Aluminum is shown on the left for different number of  $k$ -points, each in the IBZ. On the right, the real part of the conductivity  $\sigma_1(\omega)$  is plotted, taken from [SS81].

It shows the not the imaginary dielectric function but the related real conductivity  $\sigma_1(\omega) = \frac{\omega}{4\pi} \epsilon_2(\omega)$ . It shows the same characteristic peaks. Position of the peaks and the rough shape of the curve show good agreement. But due to the slow convergence, a quantitative comparison is not possible (therefore a change of the plot from

dielectric function to optical conductivity has not been made).

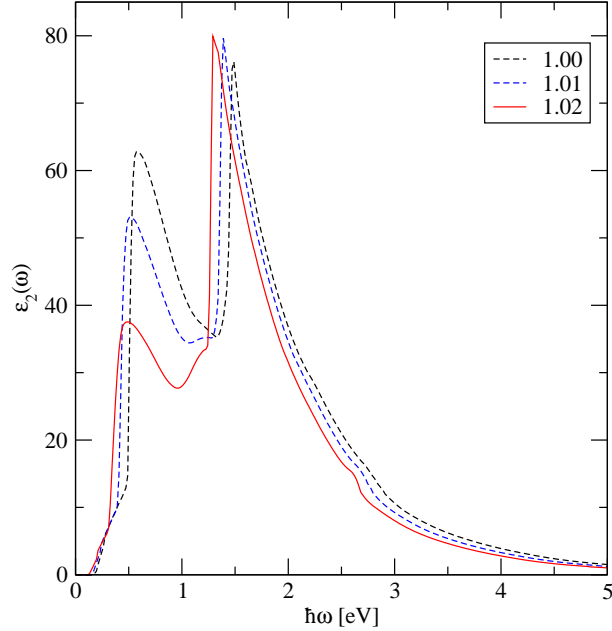


Figure 5.21: The imaginary part of the dielectric function of Aluminum for a mesh of 288  $k$ -points and three different lattice constants.

**Numerical considerations:** The self-consistency has been done for 6  $k$ -points and alternatively for 100  $k$ -points. The dielectric function does not show a visible difference. The dependence on the  $G_{max}$  cut-off value has been checked for the values  $G_{max} = 3.5, 4.8$ . No difference is visible. (Both is not shown explicitly in graphs.)

Further, the dielectric function was calculated for three slightly different lattice constants, shown in Fig. 5.21. Obviously the dielectric function is very sensitive to the shape of the Fermi surface, which (among other things) depends on the lattice constant and the Fermi energy. Thus a careful determination of the optimal lattice constant is recommended.

The accuracy and correctness were tested with respect to hermiticity and independence to the coordinate frame of reference and to the symmetry requirements. In both cases the deviations were within the overall accuracy. The choice of the muffin-tin radii (within a reasonable range) did cause no impact on the dielectric function.

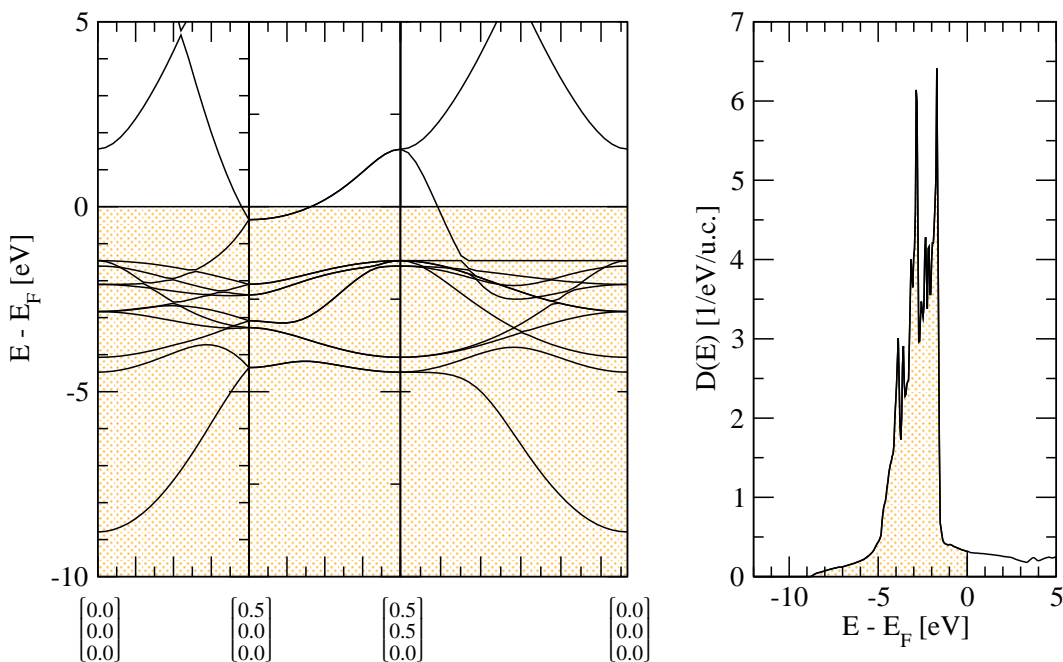


Figure 5.22: Band structure and Density of states of Copper.

## 5.7.2 Copper

The second test system is copper, which condensates in the face-centered cubic structure as well, therefore the same unit cell is used. This system was already referred to in Fig. 5.16 where the overlap for two bands is shown.

Band structure and DOS are shown in Fig. 5.22. The valence band is formed out of ten  $3d$  electrons and one  $4s$  electron per atom. The bands in the range  $-5eV \dots -1eV$  are mostly  $d$ -like, while the lowest is mostly  $s$ -like. The dielectric function is shown in 5.23. Due to the lonely band crossing the Fermi surface

**Literature:** Experimental results have been reported by Ehrenreich and Phillip [EP62]. Calculations have been done by Mueller and Phillip [MP66]. The calculated curve show meets many characteristics of the latter literature reference. There is a gap up to  $2eV$ , a peak at  $4.5eV$  and a decay towards higher energies that is a bit slower than towards lower energies. Beyond this qualitatively agreement, the numbers do not exactly fit, due to the different calculation methods as well as due to the different number of  $k$ -points.

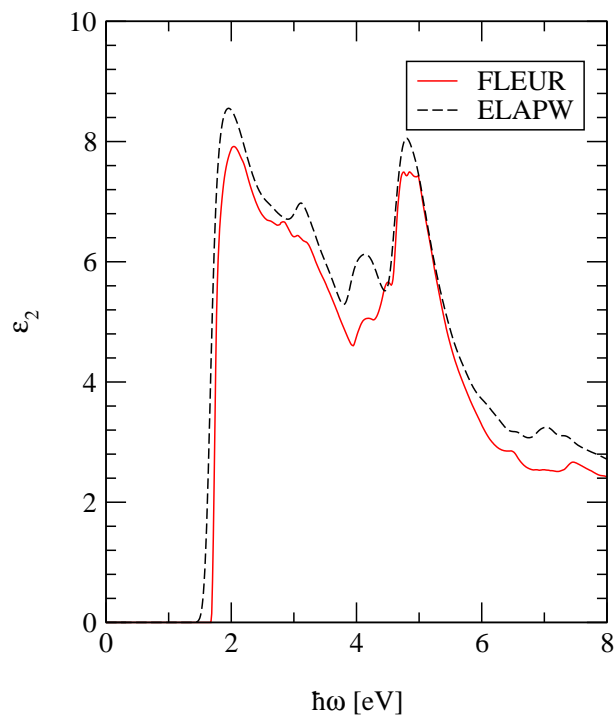


Figure 5.23: Imaginary part of the dielectric function of Copper. The solid red line is the calculated result (288 irreducible  $k$ -points), while the dashed black line is a result of an ELAPW calculation (897 irreducible  $k$ -points = 32768  $k$ -point in whole BZ; by courtesy of E. Krasovskii [Kraa]).



# Chapter 6

## Application to Phase-Change Materials

In this chapter, the method previously presented is applied. After a brief introduction of the idea of *phase-change materials* two classes of compounds (namely GeTe and AgTe compounds) are introduced. Band structure calculations are performed, and the dielectric function is determined for the GeTe system.

### 6.1 Phase-Change Materials

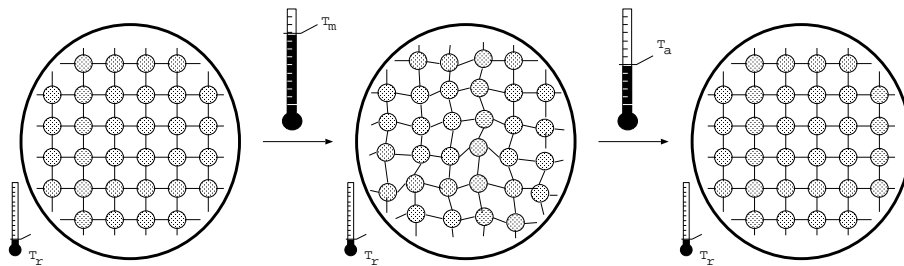


Figure 6.1: The principle of an information bit recorded by phase change. The circles illustrate a small region in the medium at room temperature  $T_r$ , indicated by the small thermometers. The changes in structure are induced by focused laser beams symbolized by the large thermometers, heating up the spot above the melting temperature  $T_m$ , or above the activation temperature  $T_a$ , respectively.

The concept of phase change recording is based on thin layers which change its structure reversibly against temperature. Being a crystal structure at room temperature, the film locally melts when shortly heated above a specific temperature  $T_m$  by a focused laser beam of high intensity. After switching off, the film rapidly

cools down with a cooling rate  $> 10^9 \frac{K}{s}$ . The rapid reduction of atomic mobility to negligible amplitudes keeps the material in this amorphous state.

When heated up again briefly above a certain *activation energy*  $T_a$  that is smaller than the melting temperature, the material recrystallizes into the previous crystal structure and keeps this structure during cooling down. Due to their different structure these two phases show different response to light. This way a bit of information can be stored. It is read out by a laser beam of low intensity, which is reflected differently depending on the structure of the spot of information.

In actual implementations, the phase change layer is sandwiched within a multilayer system of several dielectrics. This system is fixed onto a substrate.

**Motivation:** In production of information storage devices different demands compete with each other, like access time and price per capacity. This has led to a hierarchy of storage devices, primary memory (including *random access memory* (RAM) technologies), secondary memory (mass media like hard discs, read-only compact-discs (CD-ROMs), *Digital Versatile Discs* (DVDs)), and tertiary memory (tapes). In the category of rewritable mass media (second level of the hierarchy) apart from the well-known magnetic devices two technologies in particular developed into actual products, magneto-optical (MO) and phase change (PC) based devices. The rewritable DVD is already based on a phase-change effect. New materials are the subject of continuous development to improve the quality of devices and to develop new ones.

**Demands:** To be of practical use, a potential material must fulfill several criteria [Wut01]. In order to form a glass easily, the melting point should be reasonably low, around  $500^\circ C$ . The biggest part of the absorbed energy should be converted *locally* into heat to induce the phase change, resulting in a low power demand for the transformation. On the other hand the activation energy  $T_a$  to restore the crystal structure should be sufficiently high that the amorphous phase and therewith the stored data are persistent for a long period of time. A high optical contrast is important to distinguish a signal from noise, ensuring a reliable readability. A central problem in building stable layers is the mechanical stress linked with the phase transformation and the related volume change. For applicability a fast recrystallization is crucial, since this is the most time-consuming process, and an understanding of the underlying physics is needed. Investigations of potential phase-change materials include measurements of resistance, of structure, of mechanical stress, spectroscopic and ellipsometry measurements.

At present, the discovery and development of phase-change materials is mainly based upon empirical strategies. Detemple et al. [DWWB03] lately presented a structural criterion that needs to be met to enable the mandatory fast recrystallization with sufficient optical contrast that characterizes suitable phase-change materials. Only a certain subset of Te alloys showed a sufficient density change in

crystallization which is requisite for a sufficient optical contrast between crystal and amorphous phase. The alloys of this subset show a cubic or near-cubic coordination.

Using this improved knowledge of which systems to study computational methods form a useful tool to support investigations. Two classes are covered in the following sections with focus on the optical properties.

## 6.2 GeTe compounds

The majority of atoms that build the phase-change materials in investigation are from the groups 13 to 16 (formerly *IIIB* to *VIB*) of the periodic table, that is having one to four electrons in the outer  $p$ -shell, most of them from the periods four and five (Ga, Ge, As, Se, In, Sn, Sb, Te). Together with Germanium, Tellurium is the element chosen most frequently.

Composites of these elements like GeTe,  $\text{Ge}_1\text{Sb}_2\text{Te}_4$ ,  $\text{Ge}_4\text{Sb}_1\text{Te}_5$ ,  $\text{Ge}_2\text{Sb}_2\text{Te}_5$  have been investigated [Wel02, Fri00, YOMU98]. The first of these compounds, GeTe, is not only the easiest of these systems, but shows characteristics also found in other compounds.

**Structure:** The structure and binding of GeTe has been presented in [Wel02] and [Sin01] (and references therein). GeTe appears in a high-temperature and a low-temperature structure, called  $\beta$ - and  $\alpha$ -structure. While being in trigonal structure at room temperature, it merges into the rocksalt structure when crossing the transition temperature  $T_{tr}$ . A value of  $T_{tr} = 700\text{K}$  is reported for this temperature, showing a strong dependence on the stoichiometry of the sample.

These properties of bulk differ for thin films. After being created by thermal evaporation or sputtering on glass or silicon, respectively, the film transforms from the amorphous to the high-temperature rocksalt structure during tempering at  $480\text{K}$ . This coordination is conserved when being cooled down. This is not the high-temperature phase but a meta stable phase. Investigations show that the lattice parameters are comparable to that of the high-temperature phase.

The rocksalt structure is sketched in Fig. 6.2. It can be seen as two combined fcc lattices shifted by  $\frac{1}{2}(1, 1, 1)$ , i.e. half of the diagonal of the cube. The basis cell can be chosen as

$$\mathcal{A}_{fcc} = \frac{b_{cub}}{2} \begin{pmatrix} 1 & 1 & 0 \\ 1 & 0 & 1 \\ 0 & 1 & 1 \end{pmatrix}, \quad (6.1)$$

forming a trigonal unit cell with angles  $\alpha = 60^\circ$  between the unit vectors and atom

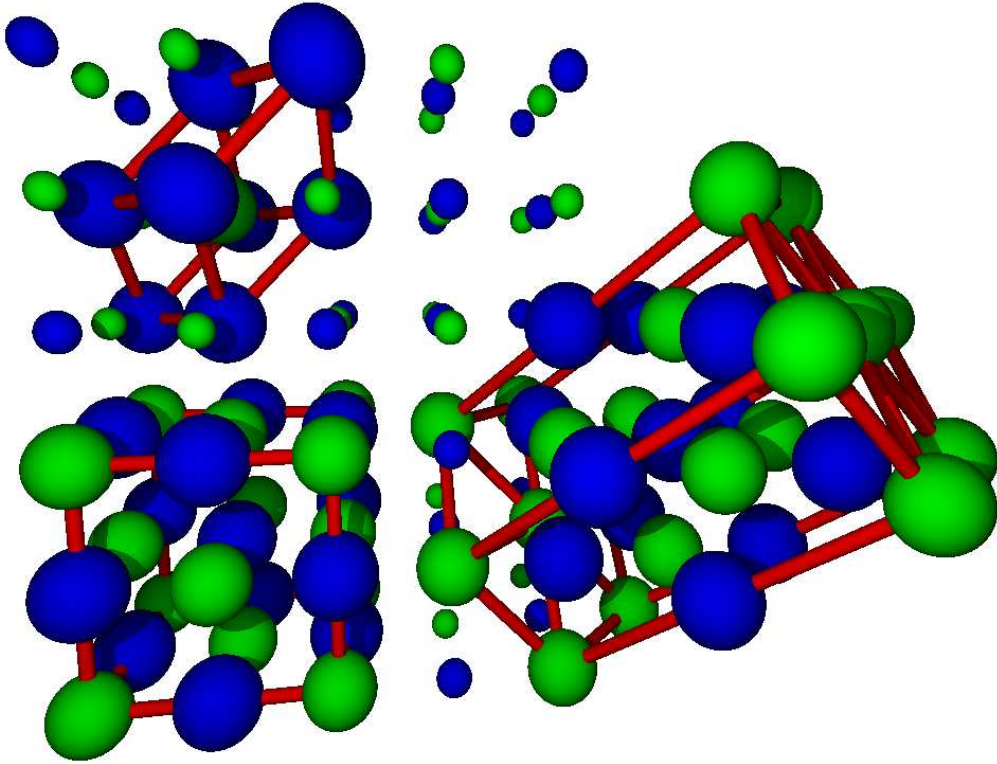


Figure 6.2: A sketch of the rocksalt structure. It consists of two fcc lattices placed into each others vacant positions. The two kinds of atoms are symbolized by the blue and green balls, respectively. Three different unit cells are marked with red sticks, a cubic one on the bottom left, a trigonal one on the top left, and a hexagonal one on the right. All atoms in the picture belong to *one* crystal. Only for reasons of survey, atoms not part of these three unit cells are painted smaller.

positions in this basis

$$\mathbf{r}_{cub}^{Ge} = \begin{pmatrix} 0 \\ 0 \\ 0 \end{pmatrix}, \quad \mathbf{r}_{cub}^{Te} = \delta \begin{pmatrix} 1 \\ 1 \\ 1 \end{pmatrix}, \quad \delta = \frac{1}{2}, \quad (6.2)$$

or vice versa. When referring to a cubic unit cell

$$\mathcal{A}_{cub} = a_{cub} \begin{pmatrix} 1 & 0 & 0 \\ 0 & 1 & 0 \\ 0 & 0 & 1 \end{pmatrix}, \quad (6.3)$$

the structure is settled by the length of the cube  $a_{cub} = b_{cub}\sqrt{2}$ . The experimental

lattice constants is reported to be  $a_{cub}^{exp} = 6.012\text{\AA}$  [ZZ]. The numerical lattice constant  $a_{cub}^{num} = 6.083\text{\AA}$  is taken from [Wel02] (see also appendix D). This structure possesses the usual cubic symmetries, that are three four-fold rotation axes along (100)-like axes, six two-fold axes along (110) and four three-fold rotation axes along (111) and that like. It possesses inversion symmetry as well.

The low temperature trigonal phase (also called *A7* phase) differs from the cubic phase expressed in a trigonal cell (6.1) by a change of the edge length  $b_{trig} = 4.293\text{\AA}$ , and the three angles still being equal among each other, but taking the value  $\alpha^{exp} = 58.128^\circ$ . Furthermore the parameter  $\delta$  now deviates from  $\delta = 0.5$  giving the configuration with the farrest distance to neighbors, but takes the value  $\delta^{exp} = 0.4746$ . The reason must therefore lie in the electronic structure. This system does not possess inversion symmetry anymore. One can imagine this as a rocksalt structure stretched in (111)-direction and compressed in the perpendicular directions.

In the present calculation this phase is modeled in hexagonal coordination described by two lattice parameters ( $a, c$ ). To transform coordinates, the trigonal cell is written as

$$\mathbf{A}_{trig} = b_{trig} \begin{pmatrix} 0 & X & -X \\ 2Y & -Y & -Y \\ Z & Z & Z \end{pmatrix} \quad (6.4)$$

with the naming  $X = \sqrt{\frac{1}{2}(1 - \cos \alpha)}$ ,  $Y = \sqrt{\frac{1}{6}(1 - \cos \alpha)}$ ,  $Z = \sqrt{\frac{1}{3}(1 + 2 \cos \alpha)}$ . The atoms are placed at

$$\mathbf{r}_{trig}^{Ge} = \begin{pmatrix} 0 \\ 0 \\ 0 \end{pmatrix}, \quad \mathbf{r}_{trig}^{Te} = \delta \begin{pmatrix} 1 \\ 1 \\ 1 \end{pmatrix}. \quad (6.5)$$

The resulting hexagonal parameters derive to

$$a_{hex} = b_{trig} \sqrt{2(1 - \cos \alpha)}, \quad c_{hex} = \sqrt{3(1 + 2 \cos \alpha)} \quad (6.6)$$

and the atom positions to

$$\mathbf{r}_{hex}^{Ge} = \left\{ \begin{pmatrix} 0 \\ 0 \\ 0 \end{pmatrix}, \begin{pmatrix} \frac{1}{3} \\ \frac{2}{3} \\ \frac{1}{3} \end{pmatrix}, \begin{pmatrix} \frac{2}{3} \\ \frac{1}{3} \\ \frac{2}{3} \end{pmatrix} \right\},$$

$$\mathbf{r}_{hex}^{Te} = \left\{ \begin{pmatrix} 0 \\ 0 \\ \delta \end{pmatrix}, \begin{pmatrix} \frac{1}{3} \\ \frac{2}{3} \\ \frac{1}{3} + \delta \end{pmatrix}, \begin{pmatrix} \frac{2}{3} \\ \frac{1}{3} \\ \frac{2}{3} + \delta \end{pmatrix} \right\}, \quad (6.7)$$

referring to the hexagonal basis

$$\mathcal{A}_{hex} = \begin{pmatrix} a_{hex} & -\frac{1}{2}a_{hex} & 0 \\ 0 & a_{hex} \cos \frac{\pi}{6} & 0 \\ 0 & 0 & c_{hex} \end{pmatrix}. \quad (6.8)$$

Thus the resulting hexagonal unit cell is three times as large as the trigonal one.

**Electronic structure:** The rocksalt structure was calculated in a basis set with shape like those used for the calculation of the fcc structures Al and Cu in Chapter five, thus containing four atoms per unit cell. The hexagonal unit cell that was used to model the  $A7$  structure contains six atoms.

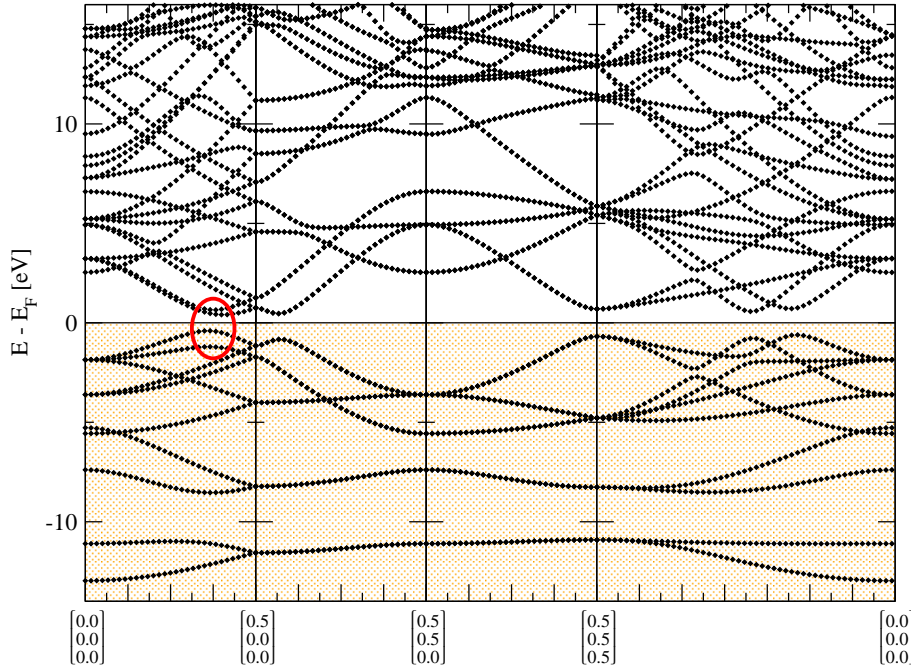


Figure 6.3: The band structure of GeTe (rocksalt) with 4 atoms/u.c. Here as well as in the following band structures and density-of-states plots, the occupied part below Fermi energy is marked with an orange fill. For semi-conductors, the Fermi energy is placed in the middle of the gap. The red ellipse marks the location close to which large contributions to the dielectric function arise.

The band structure for these two setups are shown in Figs. 6.3 and 6.4. The compound is a semi-conductor in both configurations. The bandgaps take values of  $0.51eV$  for the cubic structure and  $0.65eV$  for the  $A7$  structure. One should note that these values are sensitive to a sufficient  $G_{max}$  cut-off.

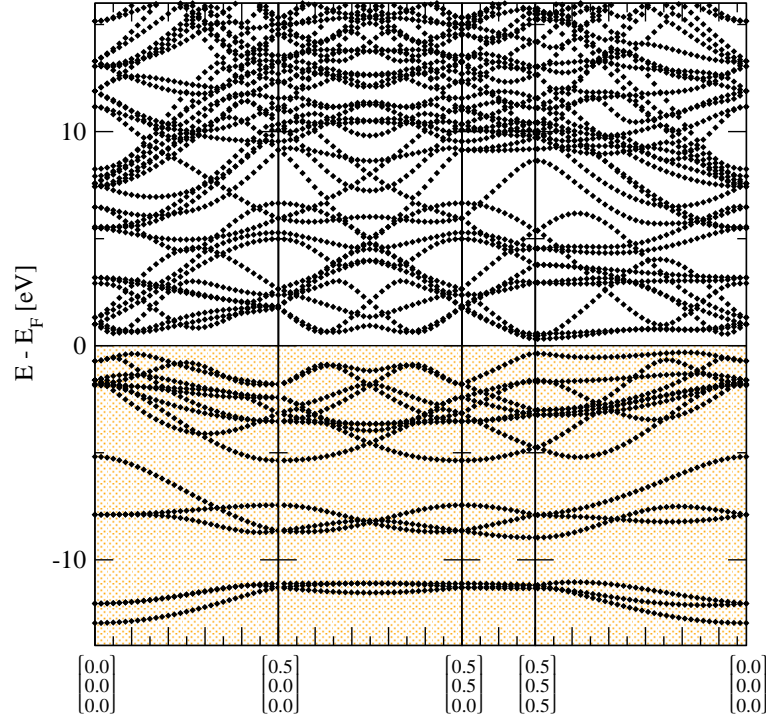


Figure 6.4: The band structure of GeTe (A7) with 6 atoms/u.c.

The according density-of-states are given in Fig. 6.5. Though not obvious from the band structures due to the different basis sets, one sees that there is only a small difference between the cubic and trigonal phase. According to [Wel02], the buckle at  $-11eV$  is formed mainly by Te  $s$ -electrons, the buckle one around  $-8eV$  by the Ge  $s$ -electrons. The contribution  $-5eV..0eV$  is made by the Ge  $p$ - and Te  $p$ -electrons. The  $d$ -electrons form lower lying states.

To investigate the possible influence of these  $d$ -states, the calculations have been performed with  $d$ -electrons included in the valence band, c.f. the dashed line in Fig. 6.5. Both curves show good agreement in the occupied part. Therefore it seems reasonable to treat these electrons as core states.

**Dielectric properties:** The dielectric function for the GeTe system in the two structures are shown in Fig. 6.6. The energy range  $0eV..19eV$  has been calculated. For both systems the dielectric function was calculated cubic-like. The peak is very large for both systems. Its main contribution could be located close to the region marked with a red circle in Fig. 6.3. Further analysis has to be made, especially to correlation to the number of  $k$ -points used.

The imaginary part of both curves are quite similar, as expected. The gaps last until  $E_g \approx 0.75eV$  and  $E_g \approx 1.0eV$ , respectively (cubic/trigonal). The broad-

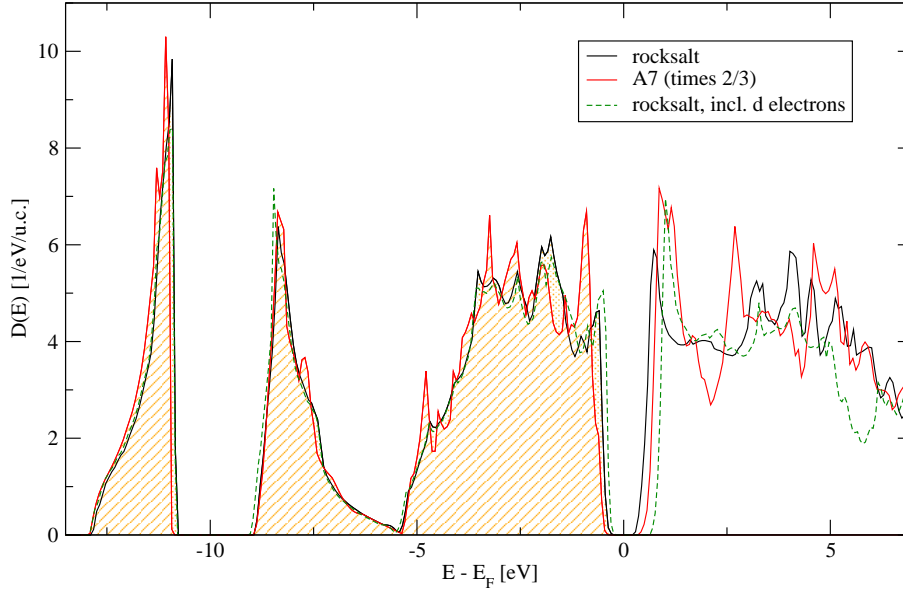


Figure 6.5: The density of states for the two GeTe structures (cubic: 75  $k$ -points, trigonal: 50  $k$ -points).

ening at  $0.5eV..0.75eV$  (cubic) might be due to backfolding effects. The large peaks are located at  $E_p = 1.50eV/E_p = 1.59eV$  and are of similar amplitude  $\varepsilon_{2,max} = 577/\varepsilon_{2,max} = 559$ . Both curves take a local minimum around  $\hbar\omega \approx 5eV$  and rise again towards a local maximum at  $\hbar\omega = 6.2eV/\hbar\omega = 7.0eV$ . The difference in the resulting real parts of the dielectric function are more visible to the naked eye. The positions of the peaks of the curve for cubic structure are slightly shifted towards lower energies. The curve in total is lower compared to the curve of the trigonal structure, giving a lower first positive peak and a second negative peak of higher amplitude.

To give a connection to the optical application the reflectivity of a bulk surface of this material (according to Eq. (3.30)) is shown in Fig. 6.7. However, in order to compare to reflectivity measurements of thin films, a different description for the reflectivity has to be used. At low frequencies including the optical range the difference between the two systems is marginal. Between  $5.0eV$  and  $6.5eV$ , however, the cubic structure shows a significant lower reflection, investigating the difference in energies of excited states as well as in the matrix elements.

At this point the comparison to calculations of amorphous structures would be interesting. From a numerical point of view, the influence of the inclusion of the  $d$ -electrons into the valence band on the dielectric function should be checked.

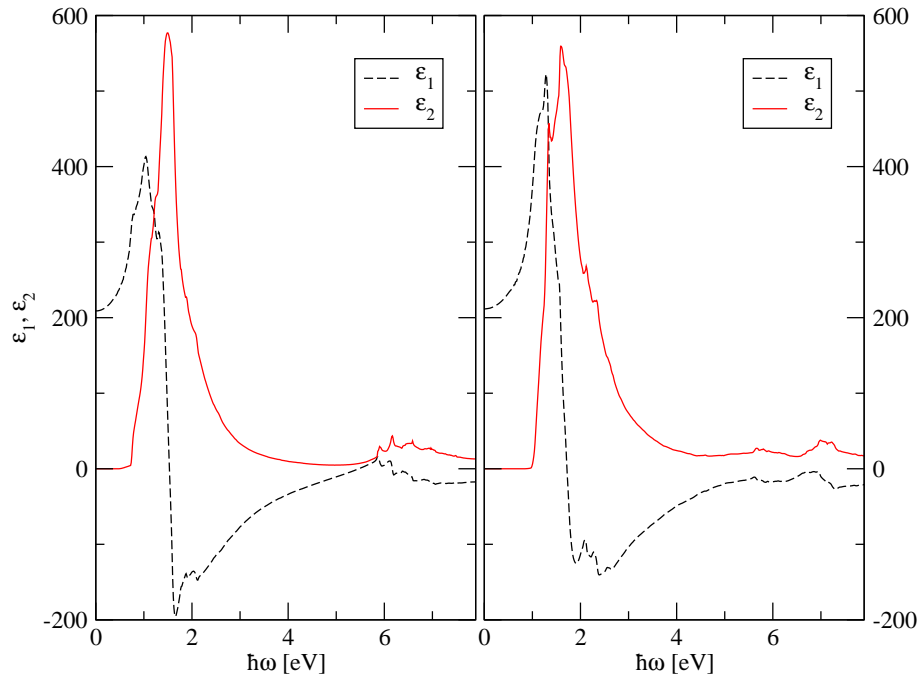


Figure 6.6: The real and imaginary part of the dielectric function of the GeTe system. The rocksalt structure is shown on the left, the trigonal A7 structure on the right.

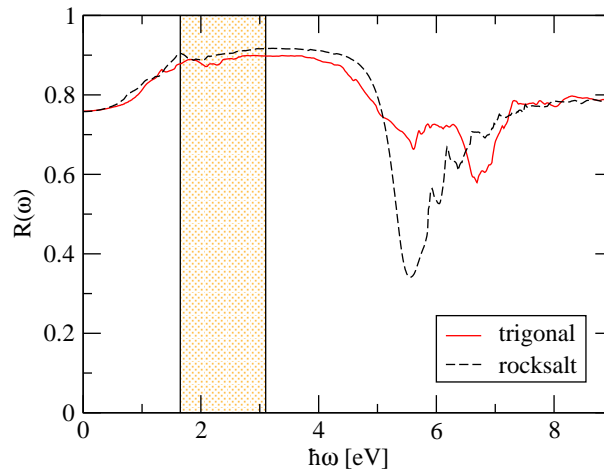


Figure 6.7: The bulk reflectivity of the two GeTe systems. To give a relation to the energy scale, the optical range (i.e. the energy range of light from  $400\text{nm}$  to  $750\text{nm}$ ) is marked with an orange fill. Solid state lasers presently used in optical data storage have a wavelength of  $780\text{nm}$ .

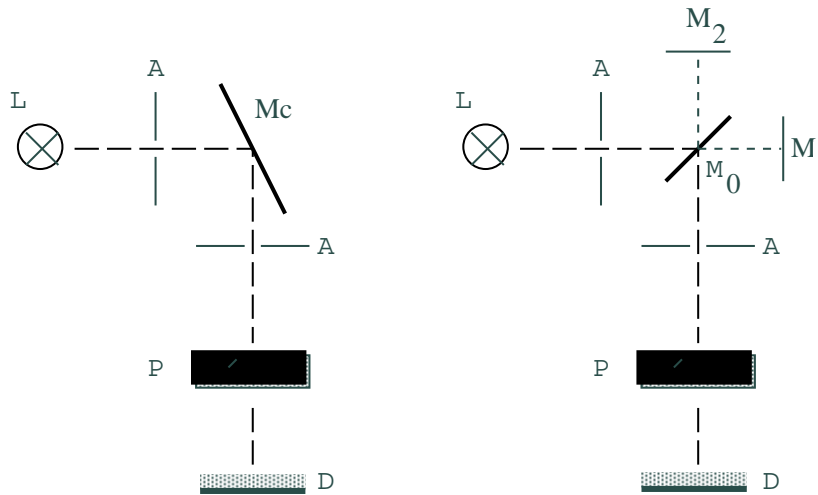


Figure 6.8: Sketch of spectrometric devices (in transmission mode). The left one bases on lattice spectroscopy. A beam from a light source  $L$  (dashed line) is reduced to a certain wavelength by the monochromator  $Mc$ , and hits (after passing the apertures  $A$ ) a probe  $P$ . The detector's signal depends on the setting of the monochromator. On the right a draft of a Fourier Analyzer is given. The light beam hits a semi-permeable mirror  $M_0$  that splits it into two beams (dotted lines) that are reflected at the mirrors  $M_1$  and  $M_2$  and reunite again at  $M_0$  to continue the path to the probe  $P$ . While one of the mirrors  $M_1, M_2$  is fixed, the other is movable to introduce a slight difference in the length of the optical path. The detector's signal depends on this difference  $\Delta x$ .

**Comparison to Measurements:** In order to determine optical properties experimentally, a major group of investigations are formed by spectroscopic methods, that are measurements to obtain a frequency dependent spectrum [Sch00]. It's principle is shown in Fig. 6.8. In direct spectroscopy, the wavelength of observation is selected with the monochromator. This gives the spectrum  $P(\omega)$  of the signal  $P$  at the detector. In Fourier Spectroscopy, the light beam interferes with itself after being split and introducing a difference in optical path  $\Delta x$ . One measures an interference spectrum  $P(\Delta x)$  which is the Fourier transform of the desired spectrum  $P(\omega)$ . With these spectroscopic methods one can obtain for instance spectra of the transmission  $T(\omega)$  or reflection  $R(\omega)$ . Another method of observation is ellipsometry, which can be used to determine the complex dielectric function [Bas95].

In Fig. 6.9 the dielectric function for the two GeTe structures obtained by ellipsometry measurements are shown. The divergence in the imaginary parts for small frequencies is expected to be due to impurities within the samples. The amplitude of the curves differs by one order of magnitude compared to the calculated curves in Fig. 6.6. This can not be explained at the moment. The peak positions of  $E_p = 1.62eV/E_p = 1.65eV$  correspond to the computed values given above, con-

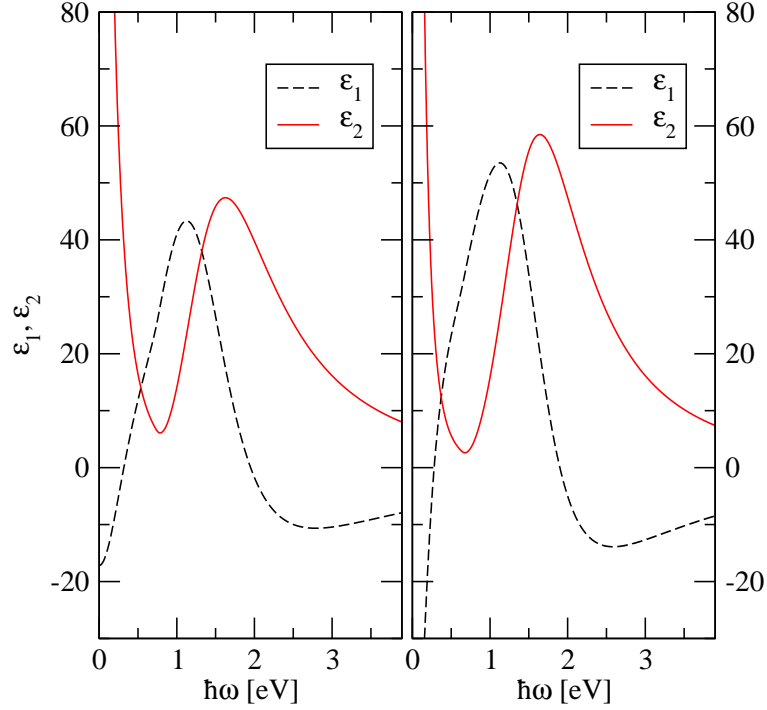


Figure 6.9: Ellipsometry measurements of GeTe (by courtesy of W. Welnic, [Wel02]). Real and imaginary part of the dielectric function are plotted for the cubic structure on the left, and for the trigonal structure on the right.

sidering the fact that a correction of the bandgap (a systematically underestimated quantity within LDA and GGA calculations) shifts the complete dielectric function with respect to energy. However, the shift of the peak (comparing cubic to trigonal setup) is larger in computation ( $0.09\text{eV}$ ) than in measurement ( $0.03\text{eV}$ ). While the amplitude lowers in computation with the change from cubic to trigonal setup, it rises in measurement. The decay in the computed curve is more rapid than in measurement. In the measured curves the local minima around  $5\text{eV}$  and the proximate local maxima seen in calculation can not be found. Due to these difference, the real parts of computation and measurement share significant characteristics, but do not agree quantitatively.

Out of these data the bulk reflection has been calculated (see Fig. 6.10)<sup>1</sup>. The general shape does qualitatively agree with Fig. 6.7 in some points. For energies  $1.0\text{eV}..1.6\text{eV}$  in the infrared range the experimental curves show the same amplitude as the theoretical ones. For lower energies the impurities in the measured sample turn the reflectivity to one. In the optical range both structures show prac-

<sup>1</sup>Since the dielectric function is determined by an explicit surface measurement, the calculation of the reflectivity in this context is of more academical nature to determine the influence of differences in the dielectric function on the reflectivity.

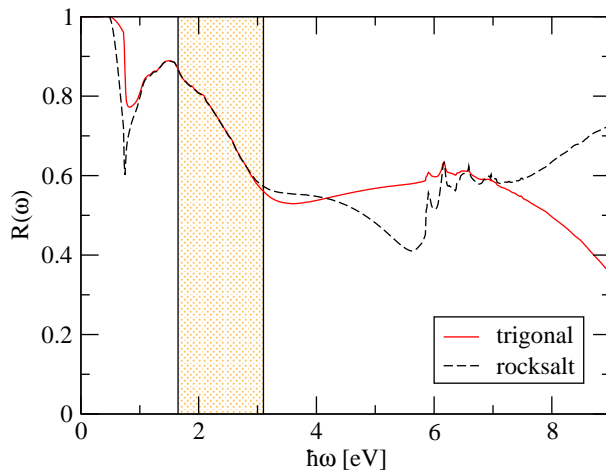


Figure 6.10: The bulk reflectivity of the two GeTe systems determined out of the experimental ellipsometry data.

tically identical but decreasing reflectivity (with respect to the energy). Results from computation also showed nearly equal but constant values in this range. Also for the experimental data the cubic structure takes a significant lower reflectivity of 0.4 around the energy of  $5.6\text{eV}$ .

### 6.3 AgTe compounds

Compounds made of the elements Ag, In, Sb and Te have been shown to be suitable for the realization of fast optical data storage devices [BvR<sup>+</sup>01]. Such compounds frequently decompose into  $\text{AgInTe}_2$  and  $\text{AgSbTe}_2$  when persistently heated [IHN<sup>+</sup>01]. These two compounds have been investigated by Detemple et al. [DWWB03].

**Structure:**  $\text{AgInTe}_2$  appears in chalcopyrite structure, while  $\text{AgSbTe}_2$  takes rocksalt structure. In the latter one, one fcc sublattice is occupied by Tellurium, the other sublattice is occupied alternately by Silver and Antimony. These chalcopyrite structure is sketched in Fig. 6.11. The chalcopyrite structure resembles the zincblende structure. It also consists of two fcc lattices shifted against each other by one fourth of the cubes diagonal. But since one sublattice is occupied alternately by Ag and In, the unit cell is double the size compared to zincblende. The appearance of this structures fits to the trend of a less cubic coordination of AgTe alloys the closer the third component (In and Sb in this case) comes to the transition metals (from the point of view of the periodic table).

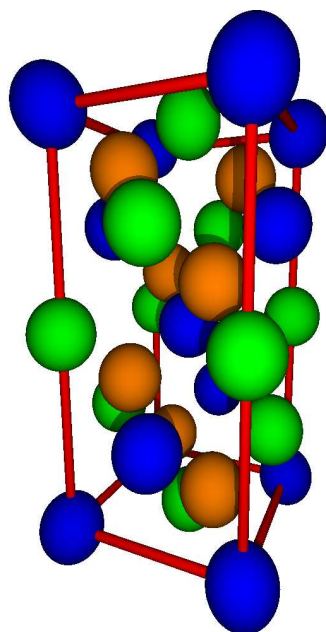


Figure 6.11: Sketch of a unit cell of the chalcopyrite structure. It is formed by two fcc sublattices occupied by three constituents in the ratio 1 : 1 : 2. For  $\text{AgInTe}_2$  for instance, the orange balls symbolize the Tellurium atoms while the green and blue balls symbolize the Silver and Indium atoms.

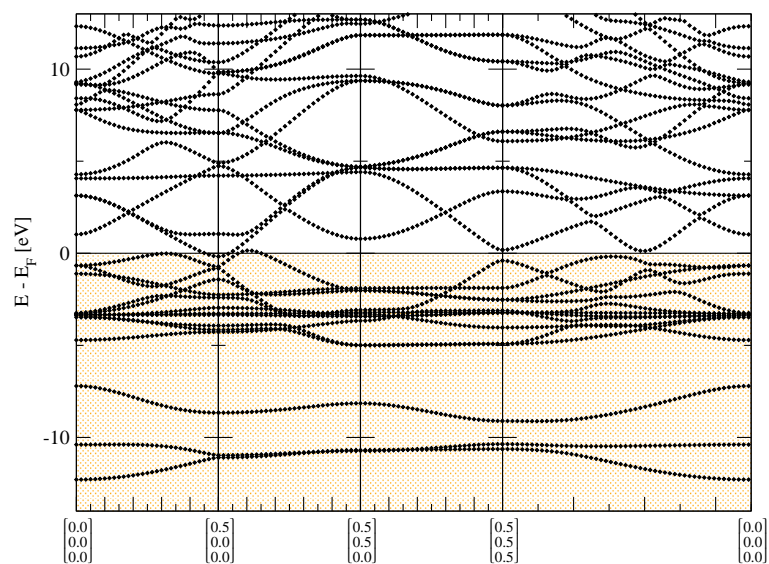


Figure 6.12: The band structure of  $\text{AgSbTe}_2$  in rocksalt structure.

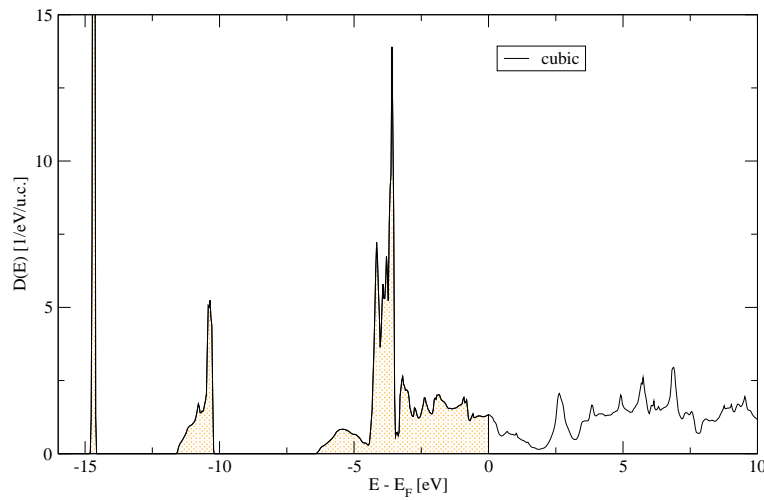


Figure 6.13: The density-of-states of  $\text{AgSbTe}_2$  in rocksalt structure.

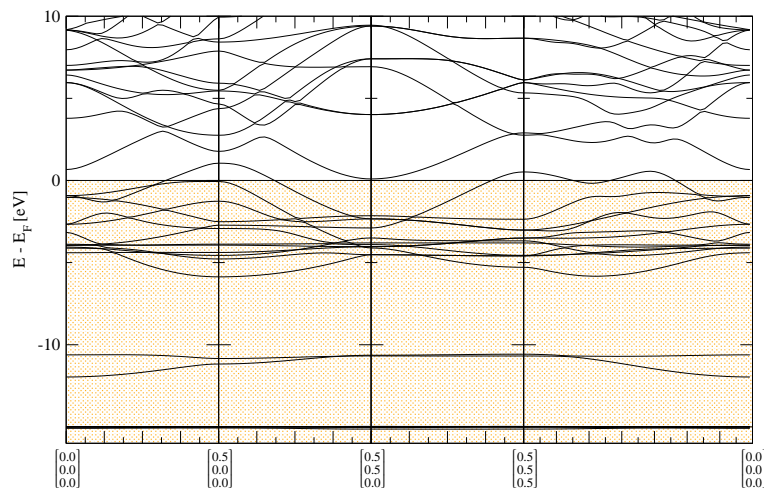


Figure 6.14: The band structure of  $\text{AgInTe}_2$  in rocksalt structure.

**Electronic properties:** To investigate the impact of the different structures, the two compounds have been calculated each in rocksalt and in chalcopyrite structure. The rocksalt structure was modeled with four atoms per unit cell, while the unit cell of the chalcopyrite structure takes sixteen atoms.

Following [DWWB03], the two compounds have been calculated in each rocksalt and chalcopyrite structure. The band structure and density-of-states of  $\text{AgSbTe}_2$  in rocksalt structure are shown for in Figs. 6.12 and 6.13. The band structure and DOS of  $\text{AgInTe}_2$  in rocksalt and chalcopyrite structure are shown in Figs. 6.14, 6.15 and

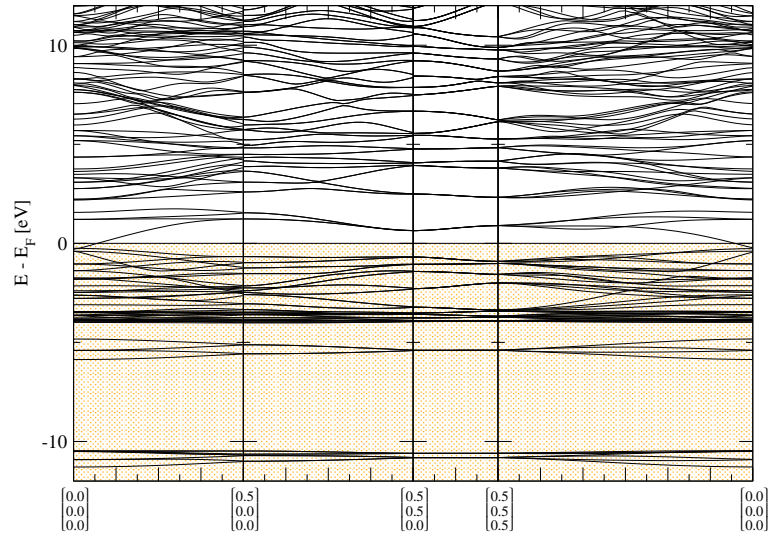


Figure 6.15: The band structure of  $\text{AgInTe}_2$  in chalcopyrite structure.

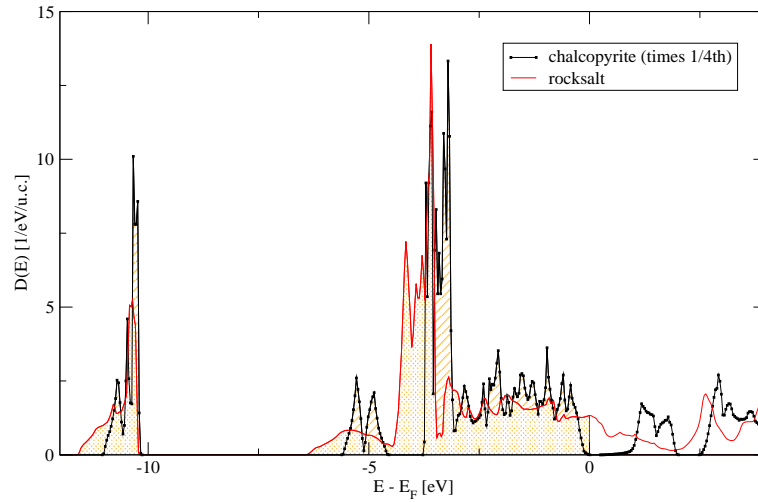


Figure 6.16: The density-of-states of both  $\text{AgInTe}_2$  compounds.

6.16. All of these systems are metals. (The gap in the plot of the DOS of  $\text{AgInTe}_2$  in chalcopyrite structure results from an inadequately chosen  $k$ -point set omitting the vicinity of the  $\Gamma$ -point.)

**Dielectric properties:** Due to the considerable computational expense of the chalcopyrite structures, caused by the number of atoms in the unit cell and the low symmetry, studies of the dielectricity could not be made. Further investigations are

planned subsequent to this diploma thesis.

# Chapter 7

## Conclusion

In this thesis we presented an implementation of the dielectric response function in linear response theory for optical excitations neglecting the local field effects and intraband transitions. The dielectric function is calculated within the density functional theory in the local density approximation and the generalized gradient approximation. The dielectric function has been realized within the context of the FLAPW method FLEUR and thus allows the treatment of materials containing transition metals in complex compounds with open structures and low symmetry. The momentum-matrix elements, the tetrahedron method and the Kramers-Kronig integration are described in detail as implemented to obtain the response function. Considerable problems occurred due to the spurious transitions of backfolded states due to calculations carried out in non-minimal unit-cells, i.e. unit cells which contain more than one chemical unit of a compound. We carefully examined these transitions and developed a procedure to minimize their contribution.

We give a detailed account on the extensive tests carried out for Al and Cu which included the dependence on the number of k-points, the number of basis functions, the dependence on the symmetry and the check of the hermiticity of the matrix elements. For Cu the results agree nicely with those of Krasovskii [Kraa] and the results for Al agree with results from literature [SS81].

We calculated the electronic properties in terms of the band structure and density of states for GeTe in rocksalt and trigonal A7 structure and for AgSbTe<sub>2</sub> and AgInTe<sub>2</sub> each in rocksalt and chalcopyrite structure for the theoretical lattice constants. Both are phase-change materials under current experimental investigations. For GeTe in both structures the bandstructure and DOS agree to large extent. The two AgInTe<sub>2</sub> structures reveal substantial differences in electronic structure close to Fermi energy. For GeTe we calculated also the dielectric function and compared with ellipsometry measurements. Although the agreement of the reflectivity is very nice, the peaks in the dielectric functions from which the reflectivity is calculated differ by a factor 10 with the experimental data. The origin of this difference is not clear yet.

The method developed opens the possibility for the application on a large variety of systems which include different phase-change materials. The amorphous state may be treated approximately using larger supercells. Technical improvements may include the local orbitals to treat semi-core states and to extend the basis set to higher unoccupied states. The method may be parallelized over the tetrahedra to run on multiprocessor computer architectures. The work done in this thesis provides a basis from which on a development in various directions becomes possible. One option is to extend this method to deal with questions in the area of magneto-optics. The other option is to extend the treatment of the density functional theory to the GW method to describe the excitation within the framework of the many body perturbation theory or the time-dependent DFT.

Though theoretically well understood, the opportunities of computation make optics more lively than ever!

# Appendix A

## Momentum matrix elements

The matrix elements of the momentum operator should be expressed in terms of the LAPW basis set in summed form (4.28), i.e.

$$\psi_i(\mathbf{k}, \mathbf{r}) = \begin{cases} \frac{1}{\sqrt{\Omega}} \sum_{\mathbf{G}} C_{\mathbf{k}+\mathbf{G}}^i e^{i(\mathbf{k}+\mathbf{G})\mathbf{r}} & \mathbf{r} \in \text{IS} \\ \sum_{l=0}^{l_{max}} \sum_{m=-l}^l [A_{lm}^{i,\alpha}(\mathbf{k}) u_l(r; E_l) + B_{lm}^{i,\alpha}(\mathbf{k}) \dot{u}_l(r; E_l)] Y_{lm}(\hat{\mathbf{r}}) & \mathbf{r} \in \text{MT}_\alpha \end{cases} \quad (\text{A.1})$$

The interstitial part of this matrix element is derived in section 5.1.1. The part inside the muffin-tins is more lengthy to derive and therefore done here. The matrix element is not calculated in the cartesian basis but in the natural basis ( $\partial_x + i\partial_y, \partial_x - i\partial_y, \partial_z$ ). In spherical coordinates these partial derivatives read

$$\begin{aligned} \partial_x \pm i\partial_y &= \sin \theta e^{\pm i\varphi} \frac{\partial}{\partial r} + \frac{1}{r} e^{\pm i\varphi} \left( \cos \theta \frac{\partial}{\partial \theta} \pm \frac{i}{\sin \theta} \frac{\partial}{\partial \varphi} \right) \\ \partial_z &= \cos \theta \frac{\partial}{\partial r} - \frac{1}{r \sin \theta} \frac{\partial}{\partial \theta}. \end{aligned} \quad (\text{A.2})$$

The radial and spherical derivatives separate. Introducing the abbreviations

$$\begin{aligned} F_{lm}^{(1)} &= - \sqrt{\frac{(l+m+1)(l+m+2)}{(2l+1)(2l+3)}} \\ F_{lm}^{(2)} &= \sqrt{\frac{(l-m)(l-m-1)}{(2l-1)(2l+1)}} \\ F_{lm}^{(3)} &= \sqrt{\frac{(l-m+1)(l-m+2)}{(2l+1)(2l+3)}} \\ F_{lm}^{(4)} &= - \sqrt{\frac{(l+m)(l+m-1)}{(2l-1)(2l+1)}} \\ F_{lm}^{(5)} &= \sqrt{\frac{(l-m+1)(l+m+1)}{(2l+1)(2l+3)}} \\ F_{lm}^{(6)} &= \sqrt{\frac{(l-m)(l+m)}{(2l-1)(2l+1)}}, \end{aligned} \quad (\text{A.3})$$

the recurrence relations of the Legendre polynomials yield the equations

$$\begin{aligned}
e^{+i\varphi} \sin \theta Y_{l,m} &= F_{lm}^{(1)} Y_{l+1,m+1} + F_{l,m}^{(2)} Y_{l-1,m+1} \\
e^{+i\varphi} \sin \theta Y_{l,m} &= F_{lm}^{(3)} Y_{l+1,m-1} + F_{l,m}^{(4)} Y_{l-1,m-1} \cdot \\
\cos \theta Y_{l,m} &= F_{lm}^{(5)} Y_{l+1,m} + F_{lm}^{(6)} Y_{l-1,m}
\end{aligned} \tag{A.4}$$

Furthermore the relations

$$\begin{aligned}
e^{+i\varphi} \left( \cos \theta \frac{\partial}{\partial \theta} + \frac{i}{\sin \theta} \frac{\partial}{\partial \varphi} \right) Y_{lm} &= -l F_{lm}^{(1)} Y_{l+1,m+1} + (l+1) F_{lm}^{(2)} Y_{l-1,m+1} \\
e^{-i\varphi} \left( \cos \theta \frac{\partial}{\partial \theta} - \frac{i}{\sin \theta} \frac{\partial}{\partial \varphi} \right) Y_{lm} &= -l F_{lm}^{(3)} Y_{l+1,m-1} + (l+1) F_{lm}^{(4)} Y_{l-1,m-1} \\
-\sin \theta \frac{\partial}{\partial \theta} Y_{lm} &= -l F_{lm}^{(5)} Y_{l+1,m} + (l+1) F_{lm}^{(6)} Y_{l-1,m}
\end{aligned} \tag{A.5}$$

In order to apply the derivatives on the LAPW functions, we define the functions (omitting the muffin-tin index  $\alpha$  for convenience)

$$\begin{aligned}
U_{lm}^i &= A_{lm}^{i,\alpha}(\mathbf{k}) u_l(r; E_l) + B_{lm}^{i,\alpha}(\mathbf{k}) \dot{u}_l(r; E_l) \\
V_{lm}^i &= \frac{\partial}{\partial r} U_{lm}^i \\
&= A_{lm}^{i,\alpha}(\mathbf{k}) u_l'(r; E_l) + B_{lm}^{i,\alpha}(\mathbf{k}) \dot{u}_l'(r; E_l) \\
W_{lm}^i &= \frac{1}{r} \cdot U_{lm}^i \\
&= \frac{1}{r} \cdot (A_{lm}^{i,\alpha}(\mathbf{k}) u_l(r; E_l) + B_{lm}^{i,\alpha}(\mathbf{k}) \dot{u}_l(r; E_l))
\end{aligned} \tag{A.6}$$

**First component  $\partial_x + i\partial_y$ :** If one expresses the LAPWs with these functions (A.6) utilizing the relations (A.2) and (A.5), one yields for the operation of the operator

$$(\partial_x + i\partial_y) \psi_i(\mathbf{k}, \mathbf{r}) = \sum_{lm} \left[ (V_{lm}^i - l W_{lm}^i) F_{lm}^{(1)} Y_{l+1,m+1} + (V_{lm}^i - (l+1) W_{lm}^i) F_{lm}^{(2)} Y_{l-1,m+1} \right], \tag{A.7}$$

omitting spatial coordinates, and the summation indices running through  $l = 0, \dots, l_{max}$ ,  $m = -l \dots l$ . Multiplying the corresponding bra gives

$$\begin{aligned}
&\int_{MT_\alpha} d^3r \psi_f^*(\mathbf{k}, \mathbf{r}) (\partial_x + i\partial_y) \psi_i(\mathbf{k}, \mathbf{r}) \\
&= \sum_{lm, l'm'} \int_0^{R_\alpha} r^2 dr \oint d\Omega U_{l'm'}^{f*} Y_{l'm'}^* \left[ (V_{lm}^i - l W_{lm}^i) F_{lm}^{(1)} Y_{l+1,m+1} + (V_{lm}^i - (l+1) W_{lm}^i) F_{lm}^{(2)} Y_{l-1,m+1} \right] \\
&= \sum_{lm, l'm'} \int_0^{R_\alpha} r^2 dr \overset{(1)}{D} 1_{lm}^{l'm'} \oint d\Omega Y_{l'm'}^* Y_{l+1,m+1} + \\
&\quad \sum_{lm, l'm'} \int_0^{R_\alpha} r^2 dr \overset{(2)}{D} 2_{lm}^{l'm'} \oint d\Omega Y_{l'm'}^* Y_{l-1,m+1}
\end{aligned} \tag{A.8}$$

with the abbreviations for  $D1, D2$  equal to

$$\begin{aligned}
(j) D1_{lm}^{l'm'} &= F_{lm}^{(2j-1)} U_{l'm'}^{f*} (V_{lm}^i - l W_{lm}^i) \\
(j) D2_{lm}^{l'm'} &= F_{lm}^{(2j)} U_{l'm'}^{f*} (V_{lm}^i - (l+1) W_{lm}^i).
\end{aligned} \tag{A.9}$$

With the spherical harmonics being orthogonal,

$$\begin{aligned}\oint d\Omega Y_{l'm'}^* Y_{l+1,m+1} &= \delta_{l',l+1} \delta_{m',m+1}, \\ \oint d\Omega Y_{l'm'}^* Y_{l-1,m+1} &= \delta_{l',l-1} \delta_{m',m+1},\end{aligned}\tag{A.10}$$

the quadruple summation in the two terms reduces to each a double one:

$$\begin{aligned}\sum_{lm,l'm'} \cdot^{(j)} D1_{lm}^{l'm'} \delta_{l',l+1} \delta_{m',m+1} &= \sum_{l=0}^{l_{max}-1} \sum_{m=-l}^{+l} \cdot^{(j)} D1_{lm}^{l+1,m+1} \\ \sum_{lm,l'm'} \cdot^{(j)} D2_{lm}^{l'm'} \delta_{l',l-1} \delta_{m',m+1} &= \sum_{l=0}^{l_{max}-1} \sum_{m=-l}^{+l} \cdot^{(j)} D2_{l+1,m-1}^{lm}.\end{aligned}\tag{A.11}$$

Please note the maximum  $l$  decreased by one. Now applying the remaining radial integration, and expanding the symbols  $D1$  and  $D2$  finally gives:

$$\begin{aligned}\langle f\mathbf{k} | \partial_x + i\partial_y | i\mathbf{k} \rangle &= \sum_{l=0}^{l_{max}-1} \sum_{m=-l}^l \\ & \left[ \left( \int u_{l+1} u'_l r^2 dr - \int u_{l+1} u_l r dr \right) A_{l+1,m+1}^{*f} A_{l,m}^i \right. \\ & + \left( \int u_{l+1} \dot{u}'_l r^2 dr - \int u_{l+1} \dot{u}_l r dr \right) A_{l+1,m+1}^{*f} B_{l,m}^i \\ & + \left( \int \dot{u}_{l+1} u'_l r^2 dr - \int \dot{u}_{l+1} u_l r dr \right) B_{l+1,m+1}^{*f} A_{l,m}^i \\ & + \left. \left( \int \dot{u}_{l+1} \dot{u}'_l r^2 dr - \int \dot{u}_{l+1} \dot{u}_l r dr \right) B_{l+1,m+1}^{*f} B_{l,m}^i \right] F_{l,m}^{(1)} \\ & + \left[ \left( \int u_l u'_{l+1} r^2 dr + (l+2) \int u_{l+1} u_l r dr \right) A_{l,m}^{*f} A_{l+1,m-1}^i \right. \\ & + \left( \int u_l \dot{u}'_{l+1} r^2 dr + (l+2) \int u_{l+1} \dot{u}_l r dr \right) A_{l,m}^{*f} B_{l+1,m-1}^i \\ & + \left( \int \dot{u}_l u'_{l+1} r^2 dr + (l+2) \int \dot{u}_{l+1} u_l r dr \right) B_{l,m}^{*f} A_{l+1,m-1}^i \\ & + \left. \left( \int \dot{u}_l \dot{u}'_{l+1} r^2 dr + (l+2) \int \dot{u}_{l+1} \dot{u}_l r dr \right) B_{l,m}^{*f} B_{l+1,m-1}^i \right] F_{l+1,m-1}^{(2)}\end{aligned}$$

**Second component  $\partial_x - i\partial_y$ :** The procedure is analogous for the next component. Again (A.2) and (A.5) help to express it as

$$\begin{aligned}(\partial_x - i\partial_y)\psi_i(\mathbf{k}, \mathbf{r}) &= \sum_{lm} \left[ (V_{lm}^i - l W_{lm}^i) F_{lm}^{(3)} Y_{l+1,m-1} \right. \\ & \left. (V_{lm}^i - (l+1) W_{lm}^i) F_{lm}^{(4)} Y_{l-1,m-1} \right].\end{aligned}\tag{A.12}$$

Multiplying the bra,

$$\begin{aligned}& \int_{MT_\alpha} d^3r \psi_f^*(\mathbf{k}, \mathbf{r}) (\partial_x - i\partial_y) \psi_i(\mathbf{k}, \mathbf{r}) \\ &= \sum_{lm,l'm'} \int_0^{R_\alpha} r^2 dr \cdot^{(3)} D1_{lm}^{l'm'} \oint d\Omega Y_{l'm'}^* Y_{l+1,m-1} + \\ & \sum_{lm,l'm'} \int_0^{R_\alpha} r^2 dr \cdot^{(4)} D2_{lm}^{l'm'} \oint d\Omega Y_{l'm'}^* Y_{l-1,m-1},\end{aligned}\tag{A.13}$$

calculating the integral over the spherical harmonics and reducing the resulting fourfold summation analogous to the first component,

$$\begin{aligned} \sum_{lm,l'm'} .^{(j)}D1_{lm}^{l'm'} \delta_{l',l+1} \delta_{m',m-1} &= \sum_{l=0}^{l_{max}-1} \sum_{m=-l}^{+l} .^{(j)}D1_{lm}^{l+1,m-1} \\ &= \sum_{lm,l'm'} .^{(j)}D2_{lm}^{l'm'} \delta_{l',l-1} \delta_{m',m-1} = \sum_{l=0}^{l_{max}-1} \sum_{m=-l}^{+l} .^{(j)}D2_{l+1,m+1}^{lm}, \end{aligned} \quad (\text{A.14})$$

yields

$$\begin{aligned} \langle f\mathbf{k} | \partial_x - i\partial_y | i\mathbf{k} \rangle &= \sum_{l=0}^{l_{max}-1} \sum_{m=-l}^l \\ &+ \left[ \left( \int u_{l+1} u'_l r^2 dr - l \int u_{l+1} u_l r dr \right) A_{l+1,m-1}^{*f} A_{l,m}^i \right. \\ &+ \left( \int u_{l+1} \dot{u}'_l r^2 dr - l \int u_{l+1} \dot{u}_l r dr \right) A_{l+1,m-1}^{*f} B_{l,m}^i \\ &+ \left( \int \dot{u}_{l+1} u'_l r^2 dr - l \int \dot{u}_{l+1} u_l r dr \right) B_{l+1,m-1}^{*f} A_{l,m}^i \\ &+ \left. \left( \int \dot{u}_{l+1} \dot{u}'_l r^2 dr - l \int \dot{u}_{l+1} \dot{u}_l r dr \right) B_{l+1,m-1}^{*f} B_{l,m}^i \right] F_{l,m}^{(3)} \\ &+ \left[ \left( \int u_l u'_{l+1} r^2 dr + (l+2) \int u_{l+1} u_l r dr \right) A_{l,m}^{*f} A_{l+1,m+1}^i \right. \\ &+ \left( \int u_l \dot{u}'_{l+1} r^2 dr + (l+2) \int u_{l+1} \dot{u}_l r dr \right) A_{l,m}^{*f} B_{l+1,m+1}^i \\ &+ \left( \int \dot{u}_l u'_{l+1} r^2 dr + (l+2) \int \dot{u}_{l+1} u_l r dr \right) B_{l,m}^{*f} A_{l+1,m+1}^i \\ &+ \left. \left( \int \dot{u}_l \dot{u}'_{l+1} r^2 dr + (l+2) \int \dot{u}_{l+1} \dot{u}_l r dr \right) B_{l,m}^{*f} B_{l+1,m+1}^i \right] F_{l+1,m-1}^{(4)}. \end{aligned}$$

**Third component  $\partial_z$ :** The same goes for the third component:

$$\begin{aligned} \partial_z \psi_i(\mathbf{k}, \mathbf{r}) &= \sum_{lm} \left[ (V_{lm}^i - l W_{lm}^i) F_{lm}^{(5)} Y_{l+1,m} \right. \\ &\quad \left. (V_{lm}^i - (l+1) W_{lm}^i) F_{lm}^{(6)} Y_{l-1,m} \right]. \end{aligned} \quad (\text{A.15})$$

Multiplication of the corresponding bra from the left:

$$\begin{aligned} &\int_{MT_\alpha} d^3r \psi_f^*(\mathbf{k}, \mathbf{r}) \partial_z \psi_i(\mathbf{k}, \mathbf{r}) \\ &= \sum_{lm,l'm'} \int_0^{R_\alpha} r^2 dr .^{(5)}D1_{lm}^{l'm'} \oint d\Omega Y_{l'm'}^* Y_{l+1,m} + \\ &\quad \sum_{lm,l'm'} \int_0^{R_\alpha} r^2 dr .^{(6)}D2_{lm}^{l'm'} \oint d\Omega Y_{l'm'}^* Y_{l-1,m} \end{aligned} \quad (\text{A.16})$$

Reduction of fourfold summation:

$$\begin{aligned} \sum_{lm,l'm'} .^{(j)}D1_{lm}^{l'm'} \delta_{l',l+1} \delta_{m',m} &= \sum_{l=0}^{l_{max}-1} \sum_{m=-l}^{+l} .^{(j)}D1_{lm}^{l+1,m} \\ &= \sum_{lm,l'm'} .^{(j)}D2_{lm}^{l'm'} \delta_{l',l-1} \delta_{m',m} = \sum_{l=0}^{l_{max}-1} \sum_{m=-l}^{+l} .^{(j)}D2_{l+1,m}^{lm} \end{aligned} \quad (\text{A.17})$$

Result:

$$\begin{aligned}
\langle f\mathbf{k}|\partial_z|i\mathbf{k}\rangle &= \sum_{l=0}^{l_{max}-1} \sum_{m=-l}^l \\
&+ \left[ \left( \int u_{l+1}u'_l r^2 dr - l \int u_{l+1}u_l r dr \right) A_{l+1,m}^{*f} A_{l,m}^i \right. \\
&+ \left( \int u_{l+1}\dot{u}'_l r^2 dr - l \int u_{l+1}\dot{u}_l r dr \right) A_{l+1,m}^{*f} B_{l,m}^i \\
&+ \left( \int \dot{u}_{l+1}u'_l r^2 dr - l \int \dot{u}_{l+1}u_l r dr \right) B_{l+1,m}^{*f} A_{l,m}^i \\
&+ \left. \left( \int \dot{u}_{l+1}\dot{u}'_l r^2 dr - l \int \dot{u}_{l+1}\dot{u}_l r dr \right) B_{l+1,m}^{*f} B_{l,m}^i \right] F_{l,m}^{(5)} \\
&+ \left[ \left( \int u_l u'_{l+1} r^2 dr + (l+2) \int u_{l+1}u_l r dr \right) A_{l,m}^{*f} A_{l+1,m}^i \right. \\
&+ \left( \int u_l \dot{u}'_{l+1} r^2 dr + (l+2) \int u_{l+1}\dot{u}_l r dr \right) A_{l,m}^{*f} B_{l+1,m}^i \\
&+ \left( \int \dot{u}_l u'_{l+1} r^2 dr + (l+2) \int \dot{u}_{l+1}u_l r dr \right) B_{l,m}^{*f} A_{l+1,m}^i \\
&+ \left. \left( \int \dot{u}_l \dot{u}'_{l+1} r^2 dr + (l+2) \int \dot{u}_{l+1}\dot{u}_l r dr \right) B_{l,m}^{*f} B_{l+1,m}^i \right] F_{l+1,m-1}^{(6)}.
\end{aligned}$$

**More general notation:** The results for the three components can be written in the form

$$\begin{aligned}
\langle f\mathbf{k}|\partial_n|i\mathbf{k}\rangle &= \sum_{l=0}^{l_{max}-1} \sum_{m=-l}^l \\
&+ \left[ \left( \int u_{l+1}u'_l r^2 dr - l \int u_{l+1}u_l r dr \right) A_{l+1,m'}^{*f} A_{l,m}^i \right. \\
&+ \left( \int u_{l+1}\dot{u}'_l r^2 dr - l \int u_{l+1}\dot{u}_l r dr \right) A_{l+1,m'}^{*f} B_{l,m}^i \\
&+ \left( \int \dot{u}_{l+1}u'_l r^2 dr - l \int \dot{u}_{l+1}u_l r dr \right) B_{l+1,m'}^{*f} A_{l,m}^i \\
&+ \left. \left( \int \dot{u}_{l+1}\dot{u}'_l r^2 dr - l \int \dot{u}_{l+1}\dot{u}_l r dr \right) B_{l+1,m'}^{*f} B_{l,m}^i \right] F_{l,m}^{(2n-1)} \\
&+ \left[ \left( \int u_l u'_{l+1} r^2 dr + (l+2) \int u_{l+1}u_l r dr \right) A_{l,m}^{*f} A_{l+1,m''}^i \right. \\
&+ \left( \int u_l \dot{u}'_{l+1} r^2 dr + (l+2) \int u_{l+1}\dot{u}_l r dr \right) A_{l,m}^{*f} B_{l+1,m''}^i \\
&+ \left( \int \dot{u}_l u'_{l+1} r^2 dr + (l+2) \int \dot{u}_{l+1}u_l r dr \right) B_{l,m}^{*f} A_{l+1,m''}^i \\
&+ \left. \left( \int \dot{u}_l \dot{u}'_{l+1} r^2 dr + (l+2) \int \dot{u}_{l+1}\dot{u}_l r dr \right) B_{l,m}^{*f} B_{l+1,m''}^i \right] F_{l+1,m''}^{(2n)}
\end{aligned}$$

for  $n = 1, 2, 3$ , and  $\partial$ ,  $m', m''$  given by

$$\partial = \begin{pmatrix} \partial_x + i\partial_y \\ \partial_x - i\partial_y \\ \partial_z \end{pmatrix}, \quad m' = \begin{pmatrix} m+1 \\ m-1 \\ m \end{pmatrix}, \quad m'' = \begin{pmatrix} m-1 \\ m+1 \\ m \end{pmatrix} \quad \text{for } n = \begin{pmatrix} 1 \\ 2 \\ 3 \end{pmatrix}.$$

**Local orbital contribution:** The contributions of the basis functions additional in the local orbital extension can be calculated analogically, resulting in extra terms of the same shape. The derivation can be found in [Abt97].



# Appendix B

## Tetrahedron method

As already mentioned in section 5.2, Blöchl, Jepsen and Andersen [BJA94] gave a convenient general notation for the tetrahedron method. They consider integrals over the Brillouin zone (BZ) in  $k$ -space like those of the expectation value of an operator  $X$ ,

$$\langle X \rangle = \frac{1}{V_G} \sum_n \int_{BZ} d^3k X_n(\mathbf{k}) f(\epsilon_n(\mathbf{k})), \quad (\text{B.1})$$

where  $f$  is the Fermi factor to an energy  $\epsilon_n$ .  $V_G$  is the volume of the Brillouin zone, and the used  $k$ -dependent expectation value reads

$$X_n(\mathbf{k}) = \langle n\mathbf{k} | X | n\mathbf{k} \rangle. \quad (\text{B.2})$$

They show that in tetrahedron method this integral can be written as

$$\langle X \rangle = \sum_{j,n} X_n(\mathbf{k}_j) w_{nj}. \quad (\text{B.3})$$

This sum runs over all bands  $n$  and  $k$ -points  $j$ .

### B.1 Integration weights

The weight of one  $k$ -point  $w_{nj}$  is the sum of weights it gets in each tetrahedron it belongs to. In each tetrahedra, the indices are assigned so that the energies are ordered,  $\epsilon_1 < \epsilon_2 < \epsilon_3 < \epsilon_4$ .

1.  $\epsilon_F < \epsilon_1$

$$w_1 = w_2 = w_3 = w_4 = 0. \quad (\text{B.4})$$

2.  $\epsilon_1 < \epsilon_F < \epsilon_2$

$$\begin{aligned}
w_1 &= C \left[ 4 - (\epsilon_F - \epsilon_1) \left( \frac{1}{\epsilon_{21}} + \frac{1}{\epsilon_{31}} + \frac{1}{\epsilon_{41}} \right) \right] \\
w_2 &= C \frac{\epsilon_F - \epsilon_1}{\epsilon_{21}} \\
w_3 &= C \frac{\epsilon_F - \epsilon_1}{\epsilon_{31}} \\
w_4 &= C \frac{\epsilon_F - \epsilon_1}{\epsilon_{41}}
\end{aligned} \tag{B.5}$$

with

$$C = \frac{V_T (\epsilon_F - \epsilon_1)^3}{4V_G \epsilon_{21} \epsilon_{31} \epsilon_{41}}. \tag{B.6}$$

3.  $\epsilon_2 < \epsilon_F < \epsilon_3$

$$\begin{aligned}
w_1 &= C_1 + (C_1 + C_2) \frac{\epsilon_3 - \epsilon_F}{\epsilon_{31}} + (C_1 + C_2 + C_3) \frac{\epsilon_4 - \epsilon_F}{\epsilon_{41}} \\
w_2 &= C_1 + C_2 + C_3 + (C_2 + C_3) \frac{\epsilon_3 - \epsilon_F}{\epsilon_{32}} + C_3 \frac{\epsilon_4 - \epsilon_F}{\epsilon_{42}} \\
w_3 &= (C_1 + C_2) \frac{\epsilon_F - \epsilon_1}{\epsilon_{31}} + (C_2 + C_3) \frac{\epsilon_F - \epsilon_2}{\epsilon_{32}} \\
w_4 &= (C_1 + C_2 + C_3) \frac{\epsilon_F - \epsilon_1}{\epsilon_{41}} + C_3 \frac{\epsilon_F - \epsilon_2}{\epsilon_{42}}
\end{aligned} \tag{B.7}$$

with

$$\begin{aligned}
C_1 &= \frac{V_T (\epsilon_F - \epsilon_1)^2}{4V_G \epsilon_{41} \epsilon_{31}} \\
C_2 &= \frac{V_T (\epsilon_F - \epsilon_1)(\epsilon_F - \epsilon_2)(\epsilon_3 - \epsilon_F)}{4V_G \epsilon_{41} \epsilon_{32} \epsilon_{31}} \\
C_3 &= \frac{V_T (\epsilon_F - \epsilon_2)^2 (\epsilon_4 - \epsilon_F)}{4V_G \epsilon_{42} \epsilon_{32} \epsilon_{41}}.
\end{aligned} \tag{B.8}$$

4.  $\epsilon_3 < \epsilon_F < \epsilon_4$

$$\begin{aligned}
w_1 &= C \frac{\epsilon_4 - \epsilon_F}{\epsilon_{41}} \\
w_2 &= C \frac{\epsilon_4 - \epsilon_F}{\epsilon_{42}} \\
w_3 &= C \frac{\epsilon_4 - \epsilon_F}{\epsilon_{43}} \\
w_4 &= \frac{V_T}{4V_G} - C \left[ 4 - (\epsilon_F - \epsilon_1) \left( \frac{1}{\epsilon_{21}} + \frac{1}{\epsilon_{31}} + \frac{1}{\epsilon_{41}} \right) \right]
\end{aligned} \tag{B.9}$$

with

$$C = \frac{V_T (\epsilon_4 - \epsilon_F)^3}{4V_G \epsilon_{41} \epsilon_{42} \epsilon_{43}}. \quad (\text{B.10})$$

5.  $\epsilon_4 < \epsilon_F$

$$w_1 = w_2 = w_3 = w_4 = \frac{V_T}{4V_G}. \quad (\text{B.11})$$

## B.2 Number and density of states

When neglecting the matrix elements, one yields the well-known terms for the number of states  $n_T(E)$  and the density of states  $D_T(E)$  of one tetrahedron, which are equivalent to the formulae given for instance by Lehmann and Taut [LT72].

Neglecting the matrix elements means setting them to one, i.e.  $X_n(\mathbf{k}_j) = 1$  in (B.3). With this the number of states and density of states take the form

$$n_T(\epsilon) = \sum_{i=1}^4 w_i, \quad D_T(\epsilon) = \frac{\partial}{\partial \epsilon} n_T(\epsilon), \quad (\text{B.12})$$

and take the following values in the five regions:

1.  $\epsilon_F < \epsilon_1$

$$\begin{aligned} n_T(\epsilon) &= 0 \\ D_T(\epsilon) &= 0 \end{aligned} \quad (\text{B.13})$$

2.  $\epsilon_1 < \epsilon_F < \epsilon_2$

$$\begin{aligned} n_T(\epsilon) &= \frac{V_T (\epsilon - \epsilon_1)^3}{V_G \epsilon_{21} \epsilon_{31} \epsilon_{41}} \\ D_T(\epsilon) &= \frac{V_T 3(\epsilon - \epsilon_1)^2}{V_G \epsilon_{21} \epsilon_{31} \epsilon_{41}} \end{aligned} \quad (\text{B.14})$$

3.  $\epsilon_2 < \epsilon_F < \epsilon_3$

$$\begin{aligned} n_T(\epsilon) &= \frac{V_T}{V_G \epsilon_{31} \epsilon_{41}} \left[ \epsilon_{21}^2 + 3\epsilon_{21}(\epsilon - \epsilon_2) + 3(\epsilon - \epsilon_2)^2 - \frac{\epsilon_{31} + \epsilon_{42}}{\epsilon_{32} \epsilon_{42}} (\epsilon - \epsilon_2)^3 \right] \\ D_T(\epsilon) &= \frac{V_T}{V_G \epsilon_{31} \epsilon_{41}} \left[ 3\epsilon_{21} + 6(\epsilon - \epsilon_2) - 3 \frac{\epsilon_{31} + \epsilon_{42}}{\epsilon_{32} \epsilon_{42}} (\epsilon - \epsilon_2)^2 \right] \end{aligned} \quad (\text{B.15})$$

4.  $\epsilon_3 < \epsilon_F < \epsilon_4$

$$\begin{aligned} n_T(\epsilon) &= \frac{V_T}{V_G} \left( 1 - \frac{(\epsilon_4 - \epsilon)^3}{\epsilon_{41}\epsilon_{42}\epsilon_{43}} \right) \\ D_T(\epsilon) &= \frac{V_T}{V_G} \frac{3(\epsilon_4 - \epsilon)^2}{\epsilon_{41}\epsilon_{42}\epsilon_{43}} \end{aligned} \tag{B.16}$$

5.  $\epsilon_4 < \epsilon_F$

$$\begin{aligned} n_T(\epsilon) &= \frac{V_T}{V_G} \\ D_T(\epsilon) &= 0 \end{aligned} \tag{B.17}$$

# Appendix C

## Units

Among gaussian and SI and other unit systems, there are the so called *atomic units* (see also appendix 6 in [ZL83]), which are favored in atomic calculations. This term actually refers to two slightly different scalings. As in all unit systems, the fine-structure constant

$$\alpha = \frac{e^2}{4\pi\epsilon_0\hbar c}$$

(here given in SI units) has to be conserved. For calculations on the atomic scale, the characteristic length is the Bohr radius

$$a_0 = \frac{4\pi\epsilon_0\hbar^2}{me^2} = 5.29 \cdot 10^{-11}m,$$

while the Rydberg energy

$$Ry = \frac{\hbar^2}{2ma_0^2} = 13.61eV$$

is the typical energy dimension.

- For *Hartree units* you set

$$\hbar = 1, m = 1, e = 1, \epsilon_0 = \frac{1}{4\pi}, c = \frac{1}{\alpha} \approx 137,$$

with the result that lengths are given in Bohr radii, and energies are multiples of  $2Ry$ , which is called one *Hartree*. The kinetic operator takes the usual form

$$\frac{\mathbf{p}^2}{2} \quad \text{or} \quad \frac{\mathbf{k}^2}{2}.$$

- In the *Rydberg* set you place

$$\hbar = 1, m = \frac{1}{2}, e^2 = 2, \epsilon_0 = \frac{1}{4\pi}, c = \frac{2}{\alpha} \approx 2 \cdot 137,$$

resulting in lengths expressed in Bohr radii, and energies in multiples of one Rydberg. But the kinetic operator takes the unnormal form

$$\mathbf{p}^2 \quad \text{or} \quad \mathbf{k}^2.$$

Whichever of the two scalings you choose, you can take a formula in gaussian or SI system and replace the quantities as mentioned above. The junction to the SI quantities energy, frequency and temperature is given by

$$1\text{eV} = 1.602 \cdot 10^{-19} \text{Ws} \quad (\text{C.1})$$

$$\frac{1\text{meV}}{\hbar} = 1.519 \text{THz} \quad (\text{C.2})$$

$$\frac{1\text{meV}}{k_B} = 11.604 \text{K}. \quad (\text{C.3})$$

# Appendix D

## Parameters of calculations

**Electronic shells:** In the following table the atomic configurations for the elements calculated with in this thesis are listed.

Element	number	atomic levels
Al	13	[Ne]. $3s^2.3p^1$
Ge	32	[Ar]. $3d^{10}.4s^2.4p^2$
Ag	47	[Kr]. $4d^{10}.5s^1$
In	49	[Kr]. $4d^{10}.5s^2.5p^1$
Sn	50	[Kr]. $4d^{10}.5s^2.5p^2$
Sb	51	[Kr]. $4d^{10}.5s^2.5p^3$
Te	52	[Kr]. $4d^{10}.5s^2.5p^4$
Au	79	[Xe]. $4f^{14}.5d^{10}.6s^1$

The notation of the atomic levels refers the the next smaller noble element, which are:

Element	number	atomic levels
He	2	$1s^2$
Ne	10	[He]. $2s^2.2p^6$
Ar	18	[Ne]. $3s^2.3p^6$
Kr	36	[Ar]. $3d^{10}.4s^2.4p^6$
Xe	54	[Kr]. $4d^{10}.5s^2.5p^6$

This sections lists the most important parameters for the self-consistent FLAPW bulk calculations, which have been performed with the FLEUR code [FLE]. The revised version (revPBE) [ZY98] of the GGA potential of Perdew, Burke and Ernzerhof (PBE) [PBE96] has been used. The number of basis functions is the maximum number of  $G$ -vectors used. The number of  $k$ -points refers to the self-consistent calculation, the DOS and the calculation of the dielectric function.

**Test systems:** These systems were calculated in chapter five for testing purposes. Aluminum was calculated in simple cubic configuration (sc) for two unit cells to illustrate backfolding.

Al (hypoth.)		
lattice structure	sc	
lattice parameter	$a_{num} = 2.729\text{\AA}$	
inversion symmetry	yes	
atoms per unit cell	1	2
$G_{max}[1/a_0]$	3.5	3.5
# of basis functions	110	206
# of electrons	3	6
# of k-points	6	6

It has been calculated in the actual face-centered cubic (fcc) configuration as well to compare to literature.

Al	
lattice structure	fcc
experimental parameters	$a_{exp} = 4.049\text{\AA}$
lattice parameters	$a_{num} = 4.049\text{\AA}$
difference ( $\frac{num}{exp} - 1$ )	0.1%
inversion symmetry	yes
atoms per unit cell	2
$G_{max}[1/a_0]$	3.5
# of basis functions	184
# of electrons	6
# of k-points	140, 300, various

The second test system was copper.

Cu	
lattice structure	fcc
lattice parameters	$a = 3.598\text{\AA}$
experimental	$a = 3.615\text{\AA}$
difference ( $\frac{num}{exp} - 1$ )	-0.4%
inversion symmetry	yes

atoms per unit cell	2
$G_{max}[1/a_0]$	3.5
# of basis functions	142
# of electrons	22
# of k-points	30, 300, 288

**GeTe compounds:** The cubic and trigonal phases were investigated. Lattice parameters are taken from [Wel02].

GeTe (high temp.)	
lattice structure	rocksalt
exp. lattice parameters	$a_{exp} = 6.012\text{\AA}$
num. lattice parameters	$a_{num} = 6.086\text{\AA}$
difference ( $\frac{num}{exp} - 1$ )	+1.23%
inversion symmetry	yes
atoms per unit cell	4
$G_{max}[1/a_0]$	3.5
# of basis functions	567
# of electrons	20, 60
# of k-points	84, 75, 288

GeTe (low temp.)	
lattice structure	trigonal (A7)
exp. lattice parameters	$a_{tr} = 4.293\text{\AA}$ $\alpha = 58.128^\circ$
exp., hexagonal	$a_{exp} = 4.171\text{\AA}$ $c_{exp} = 10.662\text{\AA}$
num., hexagonal	$a_{num} = 4.273\text{\AA}$ $c_{num} = 10.725\text{\AA}$
difference ( $\frac{num}{exp} - 1$ )	+2.45%, +0.59%
$\delta_{exp}$ <sup>1</sup>	0.4746

<sup>1</sup>Please see chapter 6 for the meaning of this parameter.

$\delta_{num}$	0.4747
inversion symmetry	no
atoms per unit cell	6
$G_{max}[1/a_0]$	3.2
# of basis functions	665
# of electrons	30
# of k-points	85, 50, 146

**AgTe compounds:** The second class of systems investigated were Silver-Tellurium compounds. The lattice numerical parameters are taken from Detemple et al. [DWWB03].

AgSbTe <sub>2</sub>	
lattice structure	rocksalt
lattice parameters	$a_{exp} = 6.08 \text{ \AA}$
lattice parameters	$a_{num} = 6.29 \text{ \AA}$
difference ( $\frac{num}{exp} - 1$ )	+3.5%
inversion symmetry	yes
atoms per unit cell	4
$G_{max}[1/a_0]$	3.4
# of basis functions	576
# of electrons	58
# of k-points	84,75

AgInTe <sub>2</sub>	
lattice structure	chalcopyrite
lattice parameters	$a_{exp} = 6.42 \text{ \AA}$
	$c_{exp} = 12.58 \text{ \AA}$
lattice parameters	$a_{num} = 6.84 \text{ \AA}$
	$c_{num} = 13.12 \text{ \AA}$
difference ( $\frac{num}{exp} - 1$ )	+6.5%, +4.3%
inversion symmetry	no
atoms per unit cell	16
$G_{max}[1/a_0]$	3.2

# of basis functions	1937
# of electrons	144
# of k-points	26,50

Detemple refers to [Hah53] for the experimental lattice constants of this system.

AgInTe <sub>2</sub>	
lattice structure	rocksalt
lattice parameters	$a_{exp} = 6.02\text{\AA}$
lattice parameters	$a_{num} = 6.22\text{\AA}$
difference ( $\frac{num}{exp} - 1$ )	+3.3%
inversion symmetry	yes
atoms per unit cell	4
$G_{max}[1/a_0]$	3.4
# of basis functions	554
# of electrons	36
# of k-points	84,75

No experimental data are available for this structure.

AgSbTe <sub>2</sub> (hypoth.)	
lattice structure	chalcopyrite
lattice parameters	$a_{num} = 7.14\text{\AA}$ $c_{num} = 13.49\text{\AA}$
inversion symmetry	no
atoms per unit cell	16
$G_{max}[1/a_0]$	3.2
# of basis functions	1937
# of electrons	144
# of k-points	26



# Bibliography

- [AAW<sup>+</sup>97] R. Ahuja, S. Auluck, J.M. Wills, M. Alouani, B. Johansson, and O. Eriksson. Optical properties of graphite from first-principles calculations. *Phys. Rev. B*, 55, 1997.
- [Abt97] R. Abt. *Berechnung optischer Eigenschaften von Hochtemperatursupraleitern in der LAPW-Methode*. PhD thesis, Universität Graz, 1997.
- [Adl62] S. Adler. Quantum Theory of the Dielectric Constant in Real Solids. *Phys. Rev.*, 126(2):413, 1962.
- [AK60] V. Ambegaokar and W. Kohn. Electromagnetic Properties of Insulators. I. *Phys. Rev.*, 117, 1960.
- [Bas95] M. Bass, editor. *Handbook of Optics*. McGraw Hill, 1995.
- [BBM<sup>+</sup>70] H. Bross, G. Bohn, G. Meister, W. Schubö, and H. Stöhr. New Version of the Modified Augmented-Plane-Wave Method. *Phys. Rev. B*, 2, 1970.
- [Bir78] F. Birch. Finite Strain Isotherm and Velocities for Single-Crystal and Polycrystalline NaCl at High Pressures and 300°K. *Journal of Geophysical Research*, 83 (B3), 1978.
- [BJA94] P. Blöchl, O. Jepsen, and O.K. Andersen. Improved tetrahedron method for Brillouin-zone integrations. *Phys. Rev. B*, 49(23), 1994.
- [Bro64] H. Bross. *Phys. Kond. Materie*, 3, 1964.
- [Bro68] H. Bross. *Helv. phys. Acta*, 41, 1968.
- [Bro93] H. Bross. On the Efficiency of Different Schemes for the Evaluation of the Density of States and Related Properties in Solids. *phys. stat. sol. B*, 179, 1993.
- [Bru70] D. Brust. Band structure and Optical Properties of Aluminum. *Solid State Communications*, 8, 1970.

- [BvR<sup>+</sup>01] H.J. Borg, M. v.Schijndel, J.C.N. Rijpers, M.H.R. Lankhorst, G. Zhou, M.H. Dekker, I.P.D. Ubbens, and M. Kuijper. Phase-Change Media for High-Numerical-Aperture and Blue-Wavelength Recording. *Jpn. J. Appl. Phys.*, 40, 2001.
- [CC73] D.J. Chadi and M.L. Cohen. Special points in the Brillouin zone. *Phys. Rev. B*, 8, 1973.
- [Cun74] S.L. Cunningham. Special k-points in 2 dimensions. *Phys. Rev. B*, 10, 1974.
- [Del98] A. Delin. *Density Functional Calculations of Optical Spectra and Narrow Band Systems*. PhD thesis, Uppsala University, 1998.
- [DWWB03] R. Detemple, D. Wamwangi, M. Wuttig, and G. Bihlmayer. Identification of Te alloys with suitable phase change characteristics. *Applied Physics Letters*, to be published, 2003.
- [EC59] H. Ehrenreich and M.H. Cohen. Self-Consistent Field Approach to the Many-Electron Problem. *Phys. Rev.*, 115, 1959.
- [EP62] H. Ehrenreich and H.R. Philipp. Optical Properties of Ag and Cu. *Phys. Rev.*, 128, 1962.
- [EPS63] H. Ehrenreich, H.R. Philipp, and B. Segall. Optical Properties of Aluminum. *Phys. Rev.*, 132, 1963.
- [Feh88] G.M. Fehrenbach. Lösung der Schrödingergleichung für Blochelektronen durch Spline-Interpolation. Master's thesis, LMU München, 1988.
- [Fer27] E. Fermi. *Atti Accad. Naz. Lincei, Cl. Sci. Fis. Mat. Nat. Rend*, 6, 1927.
- [FLE] FLEUR - Full-potential linearized augmented plane-wave code of Europe. <http://www.flapw.de>.
- [Fri00] I. Friedrich. *Optische Datenspeicherung mit Phasenwechselmedien-Präparation und Charakterisierung von GeSbTe-Schichten, Dissertation*. Forschungszentrum Juelich, Jül 3775, 2000.
- [GB75] G. Gilat and N.R. Bharatiya. Tetrahedron method of zone integration: Inclusion of matrix elements. *Phys. Rev. B*, 12, 1975.
- [GR66] G. Gilat and L.J. Raubenheimer. Accurate Numerical Method for Calculating Frequency-Distribution Functions in Solids. *Phys. Rev.*, 144, 1966.
- [Hah53] H. Hahn. *Z. Anorg. Allg. Chem.*, 271, 1953.

- [Ham79] D.R. Hamann. Semiconductor Charge Densities with Hard-Core and Soft-Core Pseudopotentials. *Phys. Rev.*, 42, 1979.
- [HK64] P. Hohenberg and W. Kohn. Inhomogeneous Electron Gas. *Phys. Rev.*, 136, 1964.
- [IHN<sup>+</sup>01] H. Iwasaki, M. Harigaya, O. Nonoyama, Y. Kageyama, M. Takahashi, K. Yamada, H. Deguchi, and Y. Ide. Completely Erasable Phase Change Optical Disc II: Application of Ag-In-Sb-Te Mixed-Phase System for Rewritable Compact Disc Compatible with CD-Velocity and Double CD-Velocity. *Jpn. J. Appl. Phys.*, 32, 2001.
- [JA71] O. Jepsen and O.K. Andersen. The electronic structure of h.c.p. Ytterbium. *Solid State Commun.*, 9, 1971.
- [KNA93] E.E. Krasovskii, V.V. Nemoshkalenko, and V.N. Antonov. On the accuracy of the wavefunctions calculated by LAPW method. *Zeitschrift für Physik B*, 91, 1993.
- [Kraa] E.E. Krasovskii. private communication.
- [Krab] E.E. Krasovskii. *The ISOLDA manual, appendix B*.
- [Kra97] E.E. Krasovskii. Accuracy and convergence properties of the extended linear APW method. *Phys. Rev. B*, 56, 1997.
- [KS65] W. Kohn and L.J. Sham. Self-Consistent Equations Including Exchange and Correlation Effects. *Phys. Rev.*, 140, 1965.
- [KS99] E.E. Krasovskii and W. Schattke. Local field effects in optical excitations of semicore electrons. *Phys. Rev. B*, 60, 1999.
- [KS01] E.E. Krasovskii and W. Schattke. Semirelativistic technique for  $\vec{k} \cdot \vec{p}$  calculations: Optical properties of Pd and Pt. *Phys. Rev. B*, 63, 2001.
- [KSS99] E.E. Krasovskii, F. Starrost, and W. Schattke. Augmented Fourier components method for constructing the crystal potential in self-consistent band-structure calculations. *Phys. Rev. B*, 59, 1999.
- [Kur00] Ph. Kurz. *Non-Collinear Magnetism at Surfaces and in Ultrathin Films, PhD thesis*. Forschungszentrum Juelich, Jül 3832, 2000.
- [Lin54] J. Lindhard. *Kgl. Danske Videnskab. Selskab, Mat.-fys. Medd.*, 28, 1954.
- [Lov89] D.R. Lovett. *Tensor properties of Crystals*. Adam Hilger, Bristol and New York, 1989.

- [LT72] G. Lehmann and M. Taut. On the Numerical Calculation of the Density of States and Related Properties. *Phys. Status Solidi B*, 54, 1972.
- [Mad78] O. Madelung. *Introduction to Solid-State Theory*. Springer Series in Solid-State Sciences. Springer-Verlag, 1978.
- [Mah80] G.D. Mahan. Modified Sternheimer equation for polarizability. *Phys. Rev. A*, 22, 1980.
- [MP66] F.M. Mueller and J.C. Phillip. Electronic Spectrum of Crystalline Copper. *Phys. Rev.*, 157, 1966.
- [MPD03] Ph. Mavropoulos, N. Papanikolaou, and P. H. Dederichs. A KKR Green function formalism for ballistic transport. *Phys. Rev. B*, to be published, arXiv:cond-mat/0306604, 2003.
- [NP58a] P. Nozières and D. Pines. Electron Interaction in Solids. Collective Approach to the Dielectric Constant. *Phys. Rev.*, 109, 1958.
- [NP58b] P. Nozières and D. Pines. Electron Interaction in Solids. General Formulation. *Phys. Rev.*, 109, 1958.
- [Nye57] J.F. Nye. *Physical Properties of Crystals*. Oxford, 1957.
- [PBE96] J.P. Perdew, K. Burke, and M. Ernzerhof. Generalized Gradient Approximation Made Simple. *PRL*, 77, 1996.
- [RF75] J. Rath and A.J. Freeman. Generalized magnetic susceptibilities in metals: Application of the analytic tetrahedron linear energy method to Sc. *Phys. Rev. B*, 11(6), 1975.
- [SBB<sup>+</sup>00] J. Schoenes, U. Barkow, M. Broschwitz, P.M. Oppeneer, D. Kaczorowski, and A. Czopnik. Optical properties of itinerant UGa<sub>3</sub>: Ellipsometric measurements and first-principles theory. *Phys. Rev. B*, 61, 2000.
- [Sch00] W. Schmidt. *Optische Spektroskopie*. Wiley VCH, 2000.
- [SF84] R. Del Sole and E. Fiorino. Macroscopic dielectric tensor at crystal surfaces. *Phys. Rev. B*, 29, 1984.
- [Sin91] D.J. Singh. Ground-state properties of lanthanum: Treatment of extended-core states. *Phys. Rev. B*, 43, 1991.
- [Sin94] D.J. Singh. *Planewaves, Pseudopotentials and the LAPW Method*. Kluwer Academic Publishers, 1994.

- [Sin01] M. Sinzinger. *Ab-initio-Untersuchungen zu den statischen und dynamischen Eigenschaften der IV-VI-Ferroelektrika GeTe und SnTe*. PhD thesis, Universität Regensburg, 2001.
- [Sla37] J.C. Slater. Wave Functions in a Periodic Potential. *Phys. Rev.*, 51, 1937.
- [SS81] F. Szmulowicz and B. Segall. Calculation of optical spectra of aluminum. *Phys. Rev. B*, 24, 1981.
- [SSIS80] E. Shiles, T. Sasaki, M. Inokuti, and D.Y. Smith. Self-consistency and sum-rule tests in the Kramers-Kronig analysis of optical data: Applications to aluminum. *Phys. Rev. B*, 22, 1980.
- [SZ80] M.J. Stott and E. Zaremba. Linear-response theory within the density-functional formalism: Application to atomic polarizabilities. *Phys. Rev. A*, 21, 1980.
- [Tho27] L.H. Thomas. *Proc. Cambridge Philos. Soc.*, 23, 1927.
- [Wel02] W. Welnic. Ab initio Untersuchungen der Struktur und Bindung von Phasenwechselmaterialien. Master's thesis, RWTH Aachen, 2002.
- [Wis63] N. Wiser. Dielectric Constant with Local Field Effects Included. *Phys. Rev.*, 129, 1963.
- [WKWF81] E. Wimmer, H. Krakauer, M. Weinert, and A.J. Freeman. Full-potential self-consistent linearized-augmented-plane-wave method for calculating the electronic structure of molecules and surfaces: O<sub>2</sub> molecule. *Phys. Rev. B*, 24, 1981.
- [Wut01] M. Wuttig. *Rewritable DVDs based on Phase Change Materials*, 31. *Ferienschule Jülich*. 2001.
- [YKS] O.V. Yazyev, K.N. Kudin, and G.E. Scuseria. Efficient algorithm for band connectivity resolution. *Phys. Rev. B*, 65.
- [YOMU98] S. Yamanaka, S. Ogawa, I. Morimoto, and Y. Ueshima. Electronic Structures and Optical Properties of GeTe and Ge<sub>2</sub>Sb<sub>2</sub>Te<sub>5</sub>. *Jpn. J. Appl. Phys.*, 37, 1998.
- [ZL83] P. Ziesche and G. Lehmann, editors. *Ergebnisse in der Elektronentheorie der Metalle*. Springer-Verlag, 1983.
- [ZS80] A. Zangwill and P. Soven. Density-functional approach to local-field effects in finite systems: Photoabsorption in the rare gases. *Phys. Rev. A*, 21, 1980.

- [ZY98] Y. Zhang and W. Yang. Comment on *Generalized Gradient Approximation Made Simple*. *PRL*, 80, 1998.
- [ZZ] T.B. Zhukova and A. Zaslavskii. *Sov. Phys. Crystallogr.*

# Danksagung

An dieser Stelle möchte ich mich bei all den freundlichen Helfern bedanken, die mich bei meiner Arbeit unterstützt haben und ohne die diese Diplomarbeit nicht möglich gewesen wäre.

Als erstes möchte ich Herrn Prof. Dr. P.H. Dederichs danken für die Übernahme der Betreuung meiner Diplomarbeit.

Herrn Prof. Dr. M. Wuttig danke ich für die Übernahme des Korreferats.

Mein besonderer Dank gilt Herrn Prof. Dr. Stefan Blügel für die freundliche Aufnahme in seiner Gruppe und die interessante Problemstellung dieser Arbeit, die mich der Faszination dieses Wissenschaftsgebietes nahe gebracht hat.

Durch seine lebendige Art hat Herr Dr. Daniel Wortmann mir stets Antrieb gegeben und ist häufig mit mir zusammen meinen Problemen auf den Leib gerückt. Ohne seine ausdauernden Korrekturlesungen und wertvollen Anmerkungen wäre diese Arbeit sicherlich nicht so leserlich.

Trotz großer Bemühungen konnte keines meiner Probleme Herrn Dr. Gustav Bihlmayer aus der Ruhe bringen. Geduldig wurde ich immer zur Einsicht und auf einen Lösungsweg gebracht und mit dem Computer versöhnt.

Besonders intensiv hat Herr Dr. habil. Eugene Krasovskii an meinen Irrungen und Wirrungen bei der Implementation Anteil genommen. Ohne die Ergebnisse der Vergleichsrechnungen, die er für mich angefertigt hat, und ohne die konkrete Hilfestellung in vielen Detailfragen hätte ich diese Arbeit nicht beenden können. Auch die Kramers-Kronig Routine, die ich nutzen durfte, hat sich als enorme Hilfe erwiesen.

Die Zeit meiner Diplomarbeit im IFF würde mir nicht so positiv in Erinnerung bleiben ohne meine Büro-Kollegen Frau Marjana Lezaic und Herrn Yuriy Mokrousov, mit denen ich nicht nur kryptische Fehlermeldung und mangelnde Konvergenzen, sondern auch diverse andere Probleme geteilt habe.

Herr Wojciech Welnic und Herr Dr. Ralf Detemple haben mir nicht nur ihre Daten für die Berechnung der Phasen-Wechselmedien zur Verfügung gestellt, sondern mir in Gesprächen diese Materialien nahe gebracht. Mancher Ungenauigkeit bei den Ausführungen zu den Phasenwechselmedien ist dank Herrn Welnic der Garaus ge-

macht worden.

Mithilfe von Herrn Dr. Phivos Mavropoulos konnte ich die Entartung in meinem Kopf aufheben und kreuzende und verknottete Energiebänder ordnen.

Ein Dank an alle nicht namentlich erwähnten Mitarbeiter der Theorie-Institute des IFF für die freundliche beziehungsweise freundschaftliche und angenehme Atmosphäre.

Mein nachhaltigster Dank gilt meinen Eltern, die mir durch immerwährenden Zuspruch und Unterstützung alle Türen geöffnet haben. Udenkbar, daß ich ohne sie diesen Weg hätte gehen können!

Hiermit versichere ich, daß ich diese Arbeit eigenhändig angefertigt habe.